Design and Optimization of Fast Switching Valves for Large Scale Digital Hydraulic Motors

Roemer, Daniel Beck

Publication date:
2014

Document Version
Publisher's PDF, also known as Version of record

DEPARTMENT OF ENERGY TECHNOLOGY
AALBORG UNIVERSITY

Design and Optimization of Fast Switching Valves for Large Scale Digital Hydraulic Motors

Daniel Beck Roemer

August, 2014

A Dissertation Submitted to the Faculty of Engineering and Science at Aalborg University in Partial Fulfilment for the degree of Doctor of Phiosophy

Design and Optimization of Fast Switching Valves
for Large Scale Digital Hydraulic Motors

Department of Energy Technology
Aalborg University
Ponstoppidanstraede 101
DK-9220 Aalborg East
Denmark

Printed in Denmark by Uniprint, Aalborg 2015

ISBN 978-87-92846-58-7

PUBLIC DEFENSE OF PHD DISSERTATION

Thesis Title:
Design and Optimization of Fast Switching Valves
for Large Scale Digital Hydraulic Motors

PhD Defendant:
Daniel B. Roemer

Supervisor:
Associate Professor Henrik C. Pedersen

Moderator:
Associate Professor Michael M. Bech

Assessment Committee:
Associate Professor Soeren Juhl Andreasen (chairman)
Department of Energy Technology
Aalborg University

Professor Rudold Scheidl
Institute of Machine Design and Hydraulic Drives
Johannes Kepler University Linz

Professor Elena Lomonova
Department of Electrical Engineering
Technische Universiteit Eindhoven

Defense Date and Place:
Friday 14th November, 2014
Pontoppidanstraede 101, Room 23
Aalborg University

Design and Optimization of Fast Switching Valves for Large Scale Digital Hydraulic Motors

by Daniel Beck Roemer

Supervisor: Henrik C. Pedersen, Ph.D., Associate Professor

List of published and submitted papers:

A **Analysis of Dynamic Properties of a Fast Switching On-Off Valve for Digital Displacement Pumps**, Daniel B. Roemer, Per Johansen, Henrik C. Pedersen and Torben O. Andersen, *in Proceedings of the Bath/ASME Symposium on Fluid Power and Motion Control, FPMC2012.*

B **Design and Modelling of Fast Switching Efficient Seat Valves for Digital Displacement Pumps**, Daniel B. Roemer, Per Johansen, Henrik C. Pedersen and Torben O. Andersen, *Transactions of the Canadian Society for Mechanical Engineering, 2013 Vol. 37, pp. 71-81.*

C **Topology Selection and Analysis of Actuator for Seat Valves suitable for use in Digital Displacement Pumps/Motors**, Daniel B. Roemer, Per Johansen, Henrik C. Pedersen and Torben O. Andersen, *in Proceedings of the 2013 IEEE International Conference on Mechatronics and Automation, ICMA2013.*

D **Analysis of Valve Requirements for High-Efficiency Digital Displacement Fluid Power Motors**, Daniel B. Roemer, Per Johansen, Henrik C. Pedersen and Torben O. Andersen, *in Proceedings of the 8^{th} International Conference on Fluid Power Transmission and Control, ICFP2013.*

E **Simulation of Dynamic Behaviour of a Digital Displacement Motor using transient 3D Computational Fluid Dynamics analysis**, Daniel B. Roemer, Per Johansen, Henrik C. Pedersen and Torben O. Andersen, *in Proceedings of the Bath/ASME Symposium on Fluid Power and Motion Control, FPMC2013.*

F **Method for Lumped Parameter simulation of Digital Displacement pumps/motors based on CFD**, Daniel B. Roemer, Per Johansen, Henrik C. Pedersen and Torben O. Andersen, *Applied Mechanics and Materials, 2013 Vols. 397-400, pp. 615-620.*

G **Design Method for Fast Switching Seat Valves for Digital Displacement Machines**, Daniel B. Roemer, Per Johansen, Henrik C. Pedersen and Torben O. Andersen, *in Proceedings of the 8^{th} FPNI Ph.D Symposium on Fluid Power, FPNI2014.*

H **Optimization of geometry of annular seat valves suitable for Digital Displacement Fluid Power Pumps/Motors**, Daniel B. Roemer, Per Johansen, Henrik C. Pedersen and Torben O. Andersen, *in Proceedings of the 2013 IEEE International Conference on Mechatronics and Automation, ICMA2013.*

I **Optimum design of seat region in valves suitable for Digital Displacement Machines**, Daniel B. Roemer, Per Johansen, Henrik C. Pedersen and Torben O. Andersen, *International Journal of Mechatronics and Automation, 2014 Vol. 4, No. 2, pp. 116-126.*

J **Oil Stiction in Fast Switching Annular Seat Valves for Digital Displacement Fluid Power Machines**, Daniel B. Roemer, Per Johansen, Henrik C. Pedersen and Torben O. Andersen, *in Proceedings of the 12th Biennial Conference on Engineering Systems Design and Analysis, ESDA2014, ASME 2014.*

K **Optimum design of a Moving Coil Actuator for Fast Switching Valves in Digital Hydraulic Pumps and Motors**, Daniel B. Roemer, Per Johansen, Michael M. Bech and Henrik C. Pedersen, *IEEE/ASME Transactions on Mechatronics, 2015, Preprint Access, DOI 10.1109/TMESH.2015.2410994.*

L **Simulation and experimental testing of actuator for a fast switching on-off valve suitable to efficient Digital Displacement Machines**, Daniel B. Roemer, Per Johansen, Michael M. Bech and Henrik C. Pedersen, *in Proceedings of the 9th JFPS International Symposium on Fluid Power, 2014.*

Other papers:

Asymptotic Approximation of Laminar Lubrication Thermal Field at Low Reduced Peclet and Brinkman Number, Per Johansen, Daniel B. Roemer, Torben O. Andersen and Henrik C. Pedersen, *Journal of Tribology, Vol. 4, No. 136.*

Multibody Dynamics of a Fluid Power Radial Piston Motor Including Transient Hydrodynamic Pressure Models of Lubricating Gaps, Per Johansen, Daniel B. Roemer, Henrik C. Pedersen and Torben O. Andersen, *in Proceedings of the ASME/BATH Symposium on Fluid Power & Motion Control, FPMC2013.*

A Modelling Approach to Multibody Dynamics of Fluid Power Machinery with Hydrodynamic Lubrication, Per Johansen, Daniel B. Roemer, Henrik C. Pedersen and Torben O. Andersen, *in Proceedings of the 8th International Conference on Fluid Power Transmission and Control, ICFP2013.*

Analytical Thermal Field Theory applicable to Oil Hydraulic Fluid Film Lubrication, Per Johansen, Daniel B. Roemer, Henrik C. Pedersen and Torben O. Andersen, *in Proceedings of ASME/BATH Symposium on Fluid Power & Motion Control, FPMC2014.*

Modelling of Spatial Conformal Lubricated Joints in Fluid Power Multibody Systems, Per Johansen, Daniel B. Roemer, Henrik C. Pedersen and Torben O. Andersen, *in Proceedings of the 9th JFPS International Symposium on Fluid Power, 2014.*

This present report combined with the above listed scientific papers has been submitted for assessment in partial fulfilment of the PhD degree. The scientific papers are not included in this version due to copyright issues. Detailed publication information is provided above and the interested reader is referred to the original published papers. As part of the assessment, co-author statements have been made available to the assessment committee and are also available at the Faculty of Engineering and Science, Aalborg University.

Preface

The work for this thesis has been carried out at the Department of Energy Technology at Aalborg University in the period Sep. 2011 - Sep. 2014. The work has been internally founded by the department at the initiative of Prof. Torben O. Andersen and Asc. Prof. Henrik C. Pedersen - thank you for making my research into this interesting field possible during this period and beyond.

I would like to thank fellow PhD-student Per Johansen for countless hours of inspiring discussions within all aspects of my work, and Asc. Prof. Michael M. Bech for numerous enthusiastic discussions and great help in developing electronic circuits for laboratory measurements. In addition, a special thanks goes to Peter Valler, Sintex A/S for his help during ordering and specification of permanent magnets, and Sintex A/S for sponsoring the permanent magnets needed for the valve prototype.

My thanks also goes to my supervisor Asc. Prof. Henrik C. Pedersen for his great support and guidance throughout the project, and my office mates Per, Lasse, Anders and Rico for many enjoying hours on and off work. Thanks also go to the staff at the workshop for their inputs and help during prototype manufacturing. Finally, a special gratitude goes to my family for their patience and support.

Aalborg, August 2014
Daniel Beck Roemer

Abstract

The present thesis is on the design, analysis and optimization of fast switching valves for digital hydraulic motors with high power ratings. The need for such high power motors origins in the potential use of hydrostatic transmissions in wind turbine drive trains, as digital hydraulic machines have been shown to improve the overall efficiency and efficient operation range compared to traditional hydraulic machines.

Digital hydraulic motors uses electronically controlled independent seat valves connected to the pressure chambers, which must be fast acting and exhibit low pressure losses to enable efficient operation. These valves are complex components to design, as multiple design aspects are present in these integrated valve units, with conflicting objectives and interdependencies.

A preliminary study on a small scale single-cylinder digital hydraulic pump has initially been conducted. Here, experimental measurements were compared to a corresponding pump model, which included a number of dynamic effects concerning the low pressure seat valve movement and its electro-magnetic actuator. The pump model was found to predict the digital pump response with reasonable accuracy, but this preliminary model included some soft parameters that were not based on known physical quantities.

Having experimental confidence in a small scale unit, attention has been turned towards the design of seat valves for large scale motors. A method for generally setting the valve requirements to obtain high efficiency was developed, where the efficiency was characterized in terms of valve switching time and flow coefficient. A suitable valve topology for large power motors was determined, resulting in annular valve geometry with a moving coil linear actuator. Transient electro-magnetic Finite Element Analysis (FEA) predicted the moving coil actuator to have superior performance compared to state of the art actuator solutions in the field.

Detailed analysis on a pressure chamber in a motor was conducted using transient 3D Computational Fluid Dynamics (CFD) simulation, including dynamic fluid domain boundaries to account for piston and valve movements. This CFD model was found to be able to simulate the chamber response, but suffers from being computationally expensive to run. A simplified lumped parameter model, based on steady CFD results, was developed and shown to compare reasonably well with the more detailed results from the transient CFD model.

An optimization method for seat valves suitable for digital hydraulic motors is presented, based on subsequent optimization and analysis of subdomains of the valve. This method includes; an optimization of the plunger and seat geometry based on a structural FEA with contact elements, a flow geometry optimization utilizing steady CFD analysis, valve stiction effects analysis, virtual mass and damping effects modeling based on transient CFD, heat dissipation analysis and an optimization of the actuator based on transient electro-magnetic FEA. The optimization method is shown applied to the selected valve topology, resulting in a well performing seat valve suitable for large scale hydraulic motors based on model predictions.

The valve designed using the above method was manufactured in order to validate the model predictions experimentally, and the transient actuator force response was found experimentally to correspond well with the model predictions. Further experiments are needed, however, to validate all aspects of the valve design.

The research documented in this dissertation has contributed with dimensioning guidelines and topology analysis of seat valves suitable for large scale digital hydraulic motors and detailed analysis methods for the pressure chambers of such machines. In addition, modeling methods of seat valves within this field have been developed, and a design method utilizing these models including optimization of subdomains has been developed and applied.

Resumé

Denne afhandling omhandler design, analyse og optimering af hurtige ventiler til digitale hydrauliske motorer i store effektklasser. Behovet for disse ventiler er opstået på baggrund af en potentiel udnyttelse af hydrauliske transmissioner i vindturbiner, idet disse digitale hydrauliske motorer har vist sig at forbedre virkningsgraden, og det effektive arbejdsområde, når de sammenlignes med konventionelle hydrauliske motorer. Digitale hydrauliske motorer benytter uafhængige elektroniske sædeventiler i forbindelse med hvert trykkammer, der skal være hurtigtskiftende og udvise et lavt tryktab for at sikre effektiv drift. Sådanne ventiler er komplicerede at designe, da de er integrerede enheder og rummer mange designområder med konfliktende objektiver og afhængigheder.

Et forstudie på en én-cylindret digital hydraulisk pumpe i lille effektklasse er blevet gennemgået som opstart på projektet. I dette forstudie blev eksperimentelle målinger sammenlignet med en udviklet pumpemodel, der inkluderede en række dynamiske effekter på lavtrykssædeventilen og dennes elektromagnetiske aktuator. Modellen viste fornuftig præcision, men inkluderede en række parametre, der ikke var baseret på kendte fysiske størrelser. Med baggrund i de eksperimentelle resultater i lille effektklasse blev fokus rettet mod designet af sædeventiler til motorer i stor effektklasse. En metode blev udviklet, med hvilken det er muligt generelt at fastsætte krav til sædeventilerne med henblik på at opnå en høj effektivitet. Denne metode karakteriserer motoreffektiviteten ud fra ventilernes skiftetid og strømningskoefficienten. En egnet ventiltopologi er blevet udvalgt, hvilket resulterede i en ringformet sædeudformning og en lineær aktuator baseret på en bevægelig spole. Transient elektro-magnetisk elementmetode har vist, at aktuatoren baseret på en bevægelig spole har bedre ydelse sammenlignet med andre kendte løsninger inden for feltet.

Detaljeret analyse af et motortrykkammer er blevet udført ved brug af en transient 3D fluid dynamisk beregning, der inkluderede dynamiske fluidgrænser for at tage højde for stempel og ventilbevægelserne. Denne beregning blev fundet brugbar til at simulere trykkammerdynamikken, men har den ulempe at være beregningsmæssigt tung at udføre. En simplificeret analysemodel, der er langt mindre beregningsmæssigt tung, blev ydermere udviklet og fundet at stemme tilfredsstillende overens med ovennævnte tungere beregningsmodel.

En optimeringsmetode for sædeventiler til brug i digitale hydrauliske motorer er blevet udviklet. Metoden baserer sig på optimering og analyse af delelementer i ventilen og indeholder; en optimering af sædegeometrien med brug af elementmetode beregninger, optimering af strømningsgeometrien ud fra fluiddynamiske beregninger, en analyse af statiske friktionsfænomener, virtuel masse og dæmpningseffekter ved flytning gennem olie, varmestrømningsanalyse samt en optimeringsalgoritme af aktuatoren baseret på elektromagnetisk elementmetode. Optimeringsmetoden er vist anvendt på den valgte ventiltopologi, hvilket resulterer i et samlet ventildesign med god ydeevne i forhold til at opnå en høj effektivitet af motoren.

Det ovennævnte ventildesign er blevet fremstillet for at validere beregningsmetoderne eksperimentelt, og den transiente ydeevne af den lineære aktuator er fundet til at stemme

godt overens med det forventede fra beregningerne. Yderligere eksperimenter er dog nødvendige for at validere alle aspekter af ventildesignet.

Forskningen gengivet i nærværende afhandling har bidraget med retningslinjer for dimensionering og en topologianalyse af sædeventiler til digitale hydrauliske motorer og detaljerede beregningsmetoder for trykkamrene i disse motorer. Analysemetoder til sædeventilerne inden for dette felt er blevet udviklet, og en samlet designmetode, der sammensætter disse metoder i en optimeringsrutine, er blevet præsenteret og vist anvendt.

Contents

Abbreviations

MW	Mega Watt
DD	Digital Displacement®
AIP	Artemis Intelligent Power
MHI	Mitsubishi Heavy Industries
HPV	High Pressure Valve
LPV	Low Pressure Valve
LP	Low Pressure
HP	High Pressure
TDC	Top Dead Center (piston)
BDC	Bottom Dead Center (piston)
CFD	Computational Fluid Dynamics
FEA	Finite Element Analysis
LPM	Lumped Parameter Model
PWM	Pulse Width Modulation
CFRP	Carbon Fiber Reinforced Polymer
PEEK	Poly-Ether-Ether-Ketone
2D,3D	Two dimensional, Three dimensional
MOSFET	Metal-Oxide-Semiconductor-Field-Effect Transistor
CAD	Computer Aided Design
FPGA	Field-Programmable Gate Array

Nomenclature

All units in the nomenclature are given in accordance with the SI-system to indicate the parameter type, even though other units and scalings may be used in the thesis. Separate nomenclatures are given for each chapter and some symbols are used differently between the chapters. In chapter 4 a small number of symbols have more than one meaning, and these symbols have been given more than one description in the below nomenclature. The correct meaning should be clear from the surrounding contents, which is hopefully the case.

Chapter 1: Introduction

η	Efficiency (-)
Q_{out}	Machine output flow (m^3/s)
Δp	Pressure difference (Pa)
τ	Shaft torque (Nm)
ω	Rotation speed (rad/s)
E_{comp}	Compression energy (J)
β	Oil stiffness (Pa)
Q	Flow rate (m^3/s)
k_f	Flow coefficient ($\sqrt{Pa}/(m^3/s)$)

Chapter 2: Preliminary Valve Studies

m	Moving mass (kg)
x, $\dot{x}$, $\ddot{x}$	Position, velocity, acceleration (m,m/s,m/s^2)
F_{act}	Actuator force (N)
i	Coil current (A)
F_{damp}	Damping force (N)
F_{stic}	Stiction force (N)
A_s	Shadow area (m^2)
F_{flow}	Flow force (N)
C_d	Discharge coefficient (-)
Re	Reynolds number (-)
A	Orifice area (m^2)
ρ	Oil density (kg/m^3)
L	Coil self-inductance (H)
N	Number of turns (-)
$\mathcal{R}_{eq}$	Equivalent magnetic reluctance (A/Wb)
F	Actuator force (N)
B_v	Viscous damping coefficient (Ns/m)
B_D	Drag coefficient (Ns^2/m^2)
B_0	Constant damping term (Ns/m)
$B_{near,op}$	Viscous friction coefficient, opening (Ns/m)
$B_{near,cl}$	Viscous friction coefficients, closing (Ns/m)
l_{sl}	Valve stroke length (m)
$x_{0,op}$, $x_{0,cl}$	Exponential coefficients, viscous friction (m)
k	Tuning parameter in stiction model (1/s)
h_i	Initial height in stiction model (m)
C_{turb}	Constant discharge coefficient in turbulent regime (-)
Re_t	Transition Reynolds number (-)
d_h	Hydraulic diameter (m)
ν	Kinematic oil viscosity (m^2/s)
O	Wetted perimeter (m)

Chapter 3: Supporting Studies for Large Scale Valves

θ, $\dot{\theta}$	Crankshaft angle and angular velocity (rad,rad/s)
p_H, p_L	Manifold high and low pressure (Pa)
p_c	Chamber pressure (Pa)
β	Oil stiffness (Pa)
V, $\dot{V}$	Chamber volume and volume rate of change (m^3,m^3/s)
Q_H, Q_L	Flow rate through high and low pressure valves (m^3/s)
V_{dead}	Dead chamber volume (m^3)
r	Crankshaft eccentricity (m)
A_p	Piston area (m^2)
V_d	Displacement volume (m^3)

$\overline{x}_L$, $\overline{x}_H$	Normalized plunger positions, range 0-1 (-)
k_f	Valve flow coefficient ($\sqrt{\text{Pa}}/(\text{m}^3/\text{s})$)
t_s	Valve switching time (s)
$\ddot{\overline{x}}$	Constant valve acceleration (m/s^2)
$\overline{x}_i$	Initial valve position (m)
θ_{LPV}, θ_{HPV}	Valve closing angles (rad)
E_{out}, E_{in}	Cycle energy output and input (J)
E_{loss}	Cycle energy loss (J)
η_α	Machine efficiency at part load (-)
α	Displacement ratio or
-	air ratio at atmospheric pressure (-)
$E_{loss,motoring}$	Energy loss for a motoring cycle (J)
$E_{loss,idling}$	Energy loss for an idling cycle (J)
$E_{in,motoring}$	Energy input for motoring cycle (J)
$E_{in,idling}$	Energy input for idling cycle (J)
$\overline{t}_s$	Normalized switching time (-)
$\overline{k}_f$	Normalized flow coefficient (-)
T_{rev}	Revolution time (s)
ρ	Fluid density (kg/m^3)
ρ_{F0}, ρ_{A0}	Density of pure oil and air respectively, atmospheric pressure (kg/m^3)
p, p_0	Oil pressure, reference oil pressure (Pa)
m	Stiffness pressure gradient (-)
κ	Adiabatic constant of air (-)
μ	Dynamic oil viscosity (-)
λ	Operation temperature ($^\circ$C)
F_{res}	Resulting fluid and actuator force (N)
Δt	Solver time step (s)
l_{stroke}	Piston stroke length (m)
x_p, x_h, x_l	Piston and valve positions (m)
A_h, A_l	Orifice areas of high and low pressure valve respectively (m^2)
m_h, m_l	As above for the moving mass (kg)
$F_{fluid,h}$	Fluid forces acting on the high pressure valve (N)
$F_{fluid,l}$	Fluid forces acting on the low pressure valve (N)
$F_{act,h}$, $F_{act,l}$	As above for the actuator forces (N)
$F_{fric,h}$	Friction forces acting on the high pressure valve (N)
$F_{fric,l}$	Friction forces acting on the low pressure valve (N)
A_{ph}, A_{pl}	Shadow areas for the high and low pressure valve (m^2)
k_1, k_2	Flow coefficients used in the LPM ($\text{Pa}/(\text{m}^3/\text{s})^2$),$\text{Pa}/(\text{m}^3/\text{s})$)
A'_h, A'_l	Normalized valve areas, high and low pressure valve (-)
γ	Force-pressure correction function (-)
f	Function used when calculating γ (-)
B_h, B_l	Drag coefficients for the high and the low pressure valve (Ns^2/m^2)
x'_h, x'_l	Normalized valve positions, high and low pressure valve (-)
K	Drag constant (-)
A_{fronth}	Frontal area of the high pressure valve plunger (m^2)
A_{frontl}	Frontal area of the low pressure valve plunger (m^2)

Chapter 4: Optimization Method for Digital Motor Valves

b	Width of flow passage (m) or
-	width of coil (m)
η	Machine efficiency (-) or
-	dynamic fluid viscosity ($\mathrm{Ns/m^2}$)
h	Plunger height parameter (m) or
-	height of coil (m) or
-	squeeze film height (m), $h = h(x)$
$\dot{h}$	Film height velocity (m/s)
h_i	Initial height (at x=0) for the stiction model (m)
α	Valve seat angle (rad)
R_{seat}	Radius defining curvature of valve seat (m)
l_{seat}	length of seat faces, cross sectional (m)
R	Main radius of valve (m)
$\underline{K}$	Stiffness matrix (N/m)
$\mathbf{u}$	Displacement vector (m)
$\mathbf{F^a}$	Applied load vector (N)
$\widetilde{\sigma}$	Modified-Mohr effective stress (Pa)
S_{ut}, S_{uc}	Ultimate tensile strength, ultimate compressive strength (Pa)
σ_1, σ_2, σ_3	Principal material stresses (Pa)
$\mathbf{x}$	Design point vector
$\mathbf{f}$	Design objective vector
f_1, f_2, f_3, f_4	Individual design objectives
$\mathbf{x}_{min}$	Minimum (optimum) design point
M_α	Set of feasible designs for a given α
S_{allow}	Maximum allowable effective material stress (Pa)
U_{ref}	Reference overhead seat length (-)
$U_{L,mean}$	Mean overhead seat length, lower part (-)
$U_{U,mean}$	Mean overhead seat length, upper part (-)
$\widehat{l}_{\mathrm{seat}}$	Estimated seat length (m)
p_{load}	Pressure chamber load pressure (Pa)
p_{cont}	Seat contact pressure (Pa)
$\widehat{R}_{\mathrm{seat}}$	Estimated seat curvature radius (m)
L_{seat}	Total circumferential seat length (m)
ν_{steel}, ν_{PEEK}	Poisson's ratio for steel and PEEK material (-)
E_{steel}, E_{PEEK}	As above with Young's modulus (Pa)
l_s	Valve stroke length (m)
Q	Valve flow rate ($\mathrm{m^3/s}$)
k_f	Valve flow coefficient ($\sqrt{\mathrm{Pa}}/(\mathrm{m^3/s})$)
Δp	Valve pressure difference (Pa)
$k_{f,eq}$	Equivalent flow coefficient ($\sqrt{\mathrm{Pa}}/(\mathrm{m^3/s})$)
$E_{loss,sym}$	Energy loss of symmetric valve (J)
$E_{loss,asym}$	Energy loss of asymmetric valve (J)

$k_{f,in}$, $k_{f,out}$	Flow coefficients for inflow and outflow ($\sqrt{\text{Pa}}/(\text{m}^3/\text{s})$)
$\overline{k}_f$	Normalized flow coefficient (-)
p_H, p_L	High and low manifold pressure (Pa)
Q_{mean}	Mean displacement flow rate ($\text{m}^3/2$)
p_c	Chamber pressure (Pa)
y_p, $\ddot{y}_p$	Valve plunger position and acceleration (m,m/s^2)
m	Plunger moving mass (kg)
A_{ps}	Pressure shadow area (m^2)
p_0	Manifold pressure level (Pa)
F_{spr}	Opening spring force (N)
F_s	Stiction force (N)
T_{stic}	Additional opening time due to stiction effects (s)
x	Squeeze film coordinate, zero at center (m)
$p = p(x)$	Squeeze film pressure distribution (Pa)
U	Relative velocity between seat surfaces in x-direction (m/s)
C_1,C_2	Integration constants
k	Geometry constant (1/m)
y	Projected plunger position (m)
γ	Seat angle used for projection (rad)
$\overline{u}$	Mean fluid velocity in squeeze film (m/s)
L	Distance from squeeze film center to the boundary (m)
p_0	Boundary pressure (Pa)
p_{min}	Minimum pressure, negative pressures denotes tension (Pa)
x_{min}	Location of minimum pressure (m)
x_{cav}	Location of cavitation boundary (m)
$\overline{p}$	Mean film pressure (Pa)
A_s	Total stiction effect area (m^2)
$\dot{x}_{cav}$	Cavitation zone velocity (m/s)
Q_{cav}	Cavitation boundary flow rate (m^3/s)
A_{cav}	Cavitation boundary flow area (m^2)
τ	Cavitation zone refilling coefficient (-)
$V_{cav,c3}$	Total volume of cavitation zone when entering case 3 (m^3)
$V_{\text{outflow,c2}}$	Outflow volume during case 2, when entering case 3 (m^3)
T_{c2}, T_{c3}, T_{c1}	Time of entering case 2, case 3 and reentering case 1 respectively (s)
$x_{cav,c3}$	Position of cavitation boundary when entering case 3 (m)
P	Surrounding pressure (Pa)
λ	loss coefficient (-)
ρ	Fluid density (kg/m^3)
F_{br}	Maximum braking force (N)
k_i	Stiffness of the mechanical interface (N/m)
Δl	Elongation of interface at maximum force (m)
E_{pot}, E_{kin}	Potential and kinetic energy (J)
m_{br}	Mass to be braked (kg)
v_{imp}	Impact velocity (m/s)
F_f	Fluid opposing force (N)
m_v	Virtual mass from surrounding fluid (kg)
B	Viscous friction coefficient (Ns/m)

D	Drag coefficient (Ns^2/m^2)
$k_1 \cdots k_5$	Additional friction coefficients
F_{em}	Electro-magnetic actuator force (N)
k_s	Spring constant (N/m)
y_i	Spring preload (m)
ν	Kinematic oil viscosity (m^2/s)
A_{act}	Shearing area of bobbin (m^2)
w	Shearing layer thickness (m)
d	Coil wire diameter (m)
n	Number of coil turns (-)
R_{coil}	Mean coil radius (m)
m_0	Moving mass excluding coil (kg)
ρ_c	Density of copper (kg/m^3)
N	Number of wire layers in coil (-)
ξ	Coil fill factor (-)
T_s	Valve switching time (s)

Chapter 5: Experimental Results on Prototype Valve

B	Magnetic flux density (T)
H	Magnetic field strength (A/m)
μ, μ_r	Permeability of free space, relative permeability (H/m,-)
M	Strength of permanent magnets (A/m)
Φ	Magnetic flux (Wb)
N_p, N_s	Number of turns in primary and secondary windings (-)
v_s	Induced voltage in secondary winding (V)
i_p	Primary winding current (A)
R_o, R_i	Outer and inner toroid radius (m)

Chapter 1

Introduction

The thesis' main objective is design and optimization of fast switching valves for digital hydraulic motors with high power ratings. The need for such machines origins in the potential use of hydrostatic transmissions in wind turbine drive trains. This chapter gives a short introduction to current large scale wind turbine drive trains, followed by a description of the hydrostatic transmission alternative. This leads to a presentation of the so-called digital hydraulic machines and the valves used in such machines, including a survey of existing technology in this field.

1.1 Wind turbines and their drive-train systems

Since the first electricity-generating horizontal axis wind turbines emerged in the mid-1900s, their power ratings have heavily increased. The state of the art trend is towards multi-megawatt turbines located offshore in wind parks having total power ratings of hundreds of megawatts. The largest current wind turbine has an impressive power rating of 7.5 MW with a rotor diameter above 125 m [1] - even larger turbines are close to market.

A key part of wind turbines is the drive train system embedded in the nacelle on top of the turbine tower. The drive train converts energy captured from the wind into power suitable for the electrical grid. Having an overall purpose of the wind turbine to generate cost-effective electricity, the drive train should have characteristics that minimize the cost of producing energy. Multiple aspects including efficiency, controllability, weight, mechanical loading, complexity, durability and maintenance must be taking into account when designing the drive train.

Three drive train types dominate within the field of commercial large scale wind turbines, which is here taken to be turbines of 5 MW and above. An overview of current (some

not commissioned yet) large scale wind turbines and some of their specifications are given in table 1.1. All of the drive trains utilized for these large scale wind turbines are variable speed, able to convert energy with rotor speeds typically in the range 5-12 RPM, in order to facilitate optimum wind energy extraction in both high and moderate wind conditions [2]. These drive trains, as shown in table 1.1, are introduced briefly in the following sections.

Table 1.1: *Specifications of current large scale wind turbines (5 MW and above). Drive train types refer to sections below.*

Manufacturer	Turbine Name	Diameter (m)	Power (MW)	Drive train
Vestas	V164	164	8.0	B
Enercon	E-126	127	7.6	A
Mitsubishi	SeaAngel	167	7.0	Hydrostatic Trans.
REpower	6M	126	6.1	C
Alstom	Haliade 150	150	6.0	A
Siemens	SWT-6.0-154	154	6.0	A
Sinovel	SL6000	128	6.0	C
Dongfang/AMSC	DEC DF140	140	5.5	C
Gamesa	G128	130	5.0	B

A: Directly driven generator with full power converter

This drive train topology reduces the number of moving parts to a minimum by avoiding a mechanical gearing. The slow rotating generator supplies electrical power with varying frequency depending on the rotation speed of the turbine, and a full power back-to-back converter facilitates supply of energy to the grid at a suitable constant frequency, cf. figure 1.1.

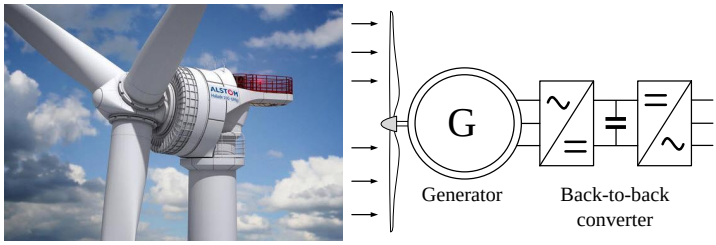

Figure 1.1: *Drive train type A. Slow rotating generator directly driven from the rotor, and a full power back-to-back converter is connected to the grid. Alstom Haliade 150 pictured left, where the large diameter generator dominates the nacelle shape [3].*

The generator used for this type of drive train is realized having a relatively large number of poles, with a large diameter generator (12 m for the Enercon E-126, 8 m for the Alstom Haliade 150, and 6.5 m for the Siemens SWT-6.0-154). A trend towards minimizing the generator diameter seems to be ongoing, as the E-126 is the oldest turbine and the SWT-

6.0-154 is the newest. This diameter reduction reduces the nacelle size of the newest large scale turbines using this drive train topology.

B: Medium ratio gearbox and full power converter

Similar to drive train A, the drive train type B also uses a full power converter. However, a medium ratio mechanical gearbox is used to increase the rotation speed of the generator shaft, as shown in figure 1.2. This decreases the generator size significantly while avoiding the high speed gears of a full ratio mechanical gearbox. Typically a gearing ratio of 15-25 is utilized [2].

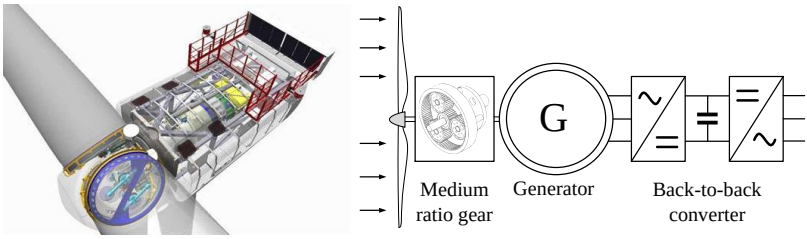

Figure 1.2: *Drive train type B. Turbine rotor connected to a medium ratio planetary gearbox, which in turn is connected to a generator and a full power converter is then connected to the grid. The Vestas V164 nacelle is shown left indicating a slimmer nacelle compared to drive train type A [4].*

Topology B has been chosen by Vestas for the V164 turbine, the highest power rating turbine currently announced.

C: High ratio gearbox and doubly-fed induction generator

The third drive train type (so-called DFIG - Doubly Fed Induction Generator) is the most common drive train used for wind turbines in general [5], and this drive train type is also well represented in the above 5 MW category. A full speed mechanical gearbox increases the shaft rotation speed to a level suitable for a generator connected directly to the grid. A back-to-back converter is connected to the generator rotor, and suitable methods are applied to allow for variable rotor speeds while connected to the grid, cf. figure 1.3. The converter needed for this drive train is typically about 25 % of the power rating and this drive train type thereby avoid the need for a full power converter [6].

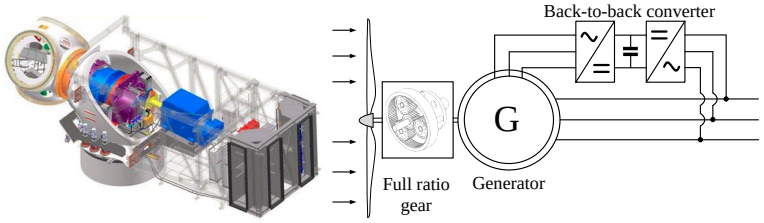

Figure 1.3: *Drive train topology C. Turbine rotor connected to a full speed gearbox which is connected to a generator directly connected to the grid. The generator rotor is supplied by a converter connected to the common grid [7].*

Efficiency and availability

The above drive trains all have their strengths and weaknesses, with no drive train being the clear optimum selection for large scale wind turbines, as evident from the variety of drive trains existing in current solutions. Ultimately, the total cost of energy (including commissioning, service, maintenance) of the complete turbine is what matters when selecting the most suitable drive train. Such cost analysis is not easily conducted and a number of uncertain factors inherently exist. One well defined parameter of the drive train, however, is the power efficiency.

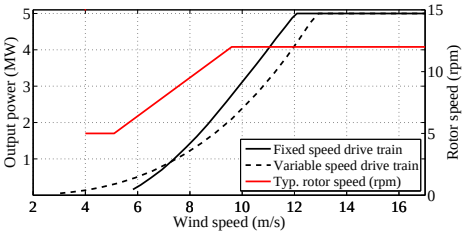

Figure 1.4: *Output power as function of wind speed for fixed and variable speed drive trains [8].*

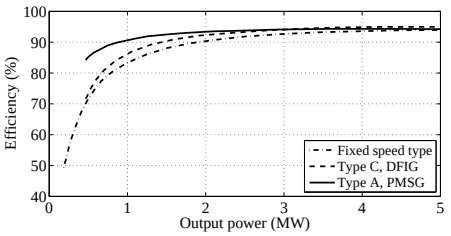

Figure 1.5: *Simulated total drive train efficiency for different drive train topologies, constructed from data in [8].*

In [8], a comparison of the total efficiency of large scale wind turbine transmissions (5 MW) is given (from rotor to grid). The efficiencies are based on simulations, and both a fixed speed drive train and two variable speed drive trains are compared. Figure 1.4 shows the output power as function of the wind speed for the efficiency analysis in [8], and figure 1.5 show the corresponding total efficiency as function of the output power. All drive trains are seen to exhibit total efficiencies above 90 % for output powers above 40 % of the rated power, and the type A drive train has an efficiency just above 90 % at 20 % load for the given simulation.

Besides having high efficiency, wind turbine drive trains should also exhibit high overall availability (effective operation time compared to potential operation time). The ReliaWind project has published the mean overall availability of wind turbines, and the distribution of downtime contributions due to different parts of the turbine [9]. The data corresponds to more than a combined 35 years of wind-farm operation. The total availability is 97 %, and the downtime distribution is shown in figure 1.6.

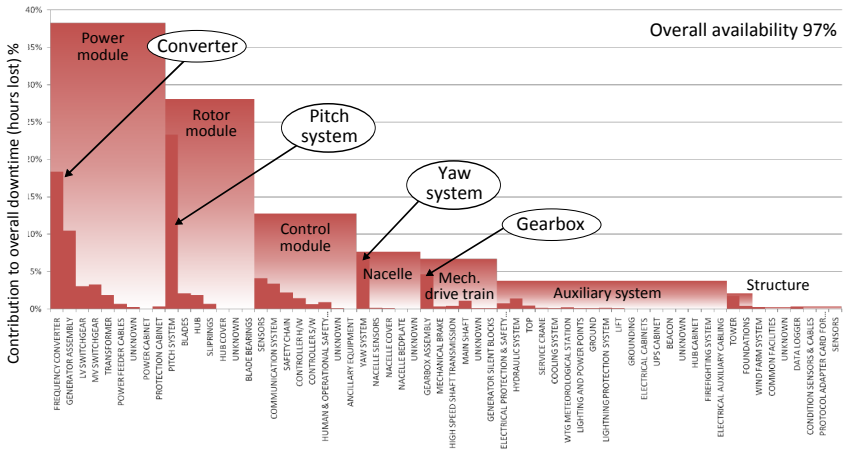

Figure 1.6: *Contribution to the overall downtime of the individual parts of the wind turbine system [9].*

As seen from figure 1.6, contributions to turbine downtime are caused by different parts of the system. The converter, generator assembly, pitch system, yaw system and gearbox contribute most to the overall downtime. Generally the drive trains currently available offers relatively high overall availability. The results from the ReliaWind project are based on existing turbines, and the requirements for availability is expected to increase for offshore large scale wind turbines.

Further details on these existing drive train solutions are beyond the scope of the present thesis, but the above introduction serve as basis for evaluating an alternative drive train utilizing a hydrostatic transmission, which is the subject of the following sections.

1.2 Alternative: Wind turbine drive train using hydrostatic transmission

Referring to table 1.1, an alternative drive train using a hydrostatic transmission is present among the commercial large scale wind turbines (currently at prototype stage, though). This drive train differs significantly from all other topologies currently used, as illustrated in figure 1.7. The wind rotor is connected to a displacement pump which,

in the general case, is a variable displacement unit. Generated fluid flow and pressure is then used to drive a variable displacement motor directly connected to a synchronous generator. No mechanical gearbox or frequency inverter is needed.

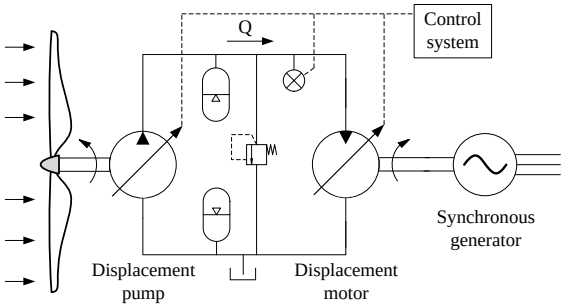

Figure 1.7: *Hydrostatic drive train for wind turbines. The wind rotor drives a slowly rotating displacement (variable or fixed) pump connected to a fast rotating variable displacement motor, in turn driving a synchronous generator directly connected to the grid.*

A number of advantages for a hydrostatic transmission based drive train are:

- The rotor is mechanically decoupled from the load, as the power is transferred through fluid flow. This decreases loading of the nacelle structure in the presence of wind gusts, as excessive power may be stored in the accumulators or be dumped through the pressure relief valve.
- By using a variable displacement motor, the hydrostatic transmission is capable of driving a generator at constant speed while allowing a variable rotor speed - without the need for a frequency inverter.
- High quality electrical output using a synchronous generator directly connected to the grid. Low-voltage ride-through is obtainable using motor displacement control in combination with accumulators and/or pressure relief valves.
- The generator may be operated at grid voltage (typically 10-33 kV) avoiding a transformer to boost the voltage as typically needed in current drive train solutions.
- Energy storage using hydraulic accumulators is easily implemented, which has superior power and energy density compared to capacitor based energy storage [10].
- Fluid power machines exhibit high power to weight ratios, suggesting a possible reduction in weight for the speed gearing compared to a mechanical gearbox[1].

[1] As example: A 5 MW full speed mechanical transmission made by Wikov weighs 57t or 11t/MW whereas a 2 MW slow rotating hydraulic pump made by Hagglunds weighs 5t/MW and a 0.85 MW fast rotating hydraulic motor made by Danfoss weighs 0.1t/MW - giving roughly half the transmission weight of the hydrostatic transmission compared to the mechanical.

The concept of using a hydrostatic transmission in wind turbines is not new, and the large power density of fluid power machinery is an intriguing property for wind turbine transmissions. In 1976, a 3 MW wind turbine with hydrostatic transmission was installed and tested, but the turbine proved to be inefficient and unreliable, and the turbine was disassembled after only a few hours of operation [11].

One recent attempt on developing an efficient 1 MW hydrostatic transmission drive train is presented in [12]. Here two parallel fixed displacement pumps are used for generating flow (with an option of short circuiting one of the pumps during partial load), which in turn is connected two four displacement motors (three of them variable) driving two synchronous generators, cf. left part of figure 1.8. The resulting total drive train efficiency is shown to the right in figure 1.8. A maximum efficiency of approximately 85 % is found experimentally, and an efficiency in the range of 70-80 % is found for lower rotation speeds, corresponding to the partial loading regime.

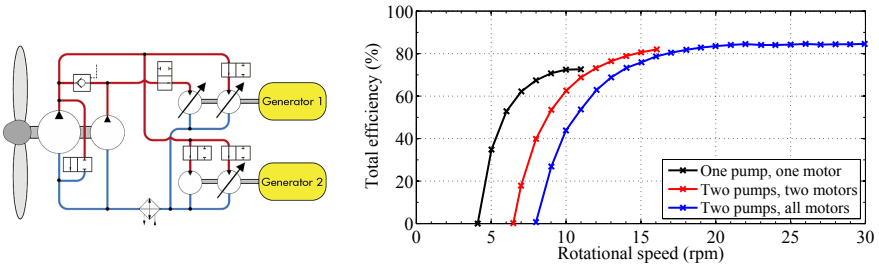

Figure 1.8: *Hydrostatic transmission drive train presented in [12] with corresponding total efficiency.*

Another contribution within hydrostatic transmissions for wind turbines has been made by the company ChapDrive AS. Their largest transmission was installed in a 900 kW wind turbine. This transmission utilized a Hägglunds low speed fixed displacement pump unit in the nacelle and two Bosch Rexroth (A4 type) variable displacement motors located at the tower base together with the synchronous generator. Successful operation during a period of three years is reported using this 900 kW transmission and a smaller 225 kW similar transmission [13]. However, no data on the drive train efficiency is available. The company was closed down in 2013, and no further development on their drive train is being conducted.

Commercial fluid power units suitable for realizing a wind turbine transmission in the MW range exist. Taking state of the art commercial components as an example, a 2 MW drive train solution could be comprised of a 2 MW slow rotating fixed displacement hydraulic pump, two or three fast rotating variable displacement motors and a corresponding number of synchronous generators.

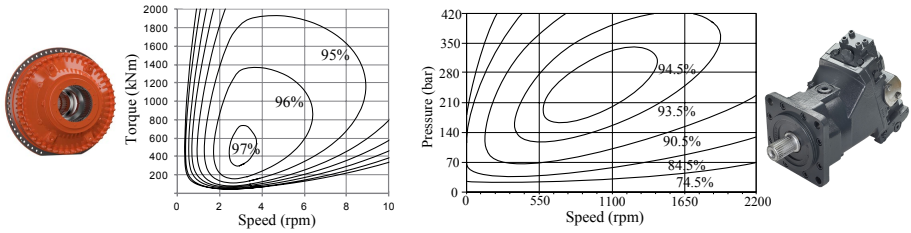

Figure 1.9: *Efficiency contours for the Hägglunds CBM6000 low-speed high-torque displacement pump (left) and full displacement efficiency contours of the Danfoss S51-250 bent-axis displacement motor (right) [14, 15].*

Figure 1.9 show efficiency contours of such a 2 MW slow rotating fixed displacement pump (left), with a maximum operation pressure of 350 bar, and a 0.85 MW fast rotating variable displacement motor (right). Assuming maximum power throughput, the pump is operating at 10 rpm and 2 MNm (corresponding to 350 bar) at 94-95% efficiency. Operating the motor at 1500 rpm to drive a generator gives an efficiency about 94 %. Typically the generator is able to maintain an efficiency of 98 %. Neglecting all other losses besides those in these components gives a maximum drive train efficiency of 87 %. Flow losses, cooling and control electronics will further limit the maximum efficiency, which correspond well with the measured maximum efficiency in figure 1.8. With a solution where multiple pumps/motors are utilized, the part load efficiency is lower, depending on the number of units and how declutching and/or short circuiting is implemented for partial displacement operation.

In total, a hydrostatic transmission based drive train for wind turbines realized using commercially available components has an energy efficiency significantly below existing wind turbine drive train solutions, cf. figure 1.5. This is one of the reasons for the lack of any commercial wind turbine with a hydrostatic transmission, despite the advantages outlined above.

Technology utilizing the so-called digital hydraulic machines, also termed Digital Displacement® (DD) machines by the original inventors, is promising to improve the efficiency of fluid power machines, leading the way for hydrostatic transmissions in wind turbines, as also shown previously in table 1.1. This technology, and illustrations of a large scale prototype drive train utilizing this technology, is the topic of the following sections. The term DD is used interchangeably to replace the term 'digital hydraulic' throughout the thesis, and DD machines are also referred to simply as 'digital' machines for convenience.

Drive train based on digital hydraulic machines

The difference between traditional variable displacement machines (typically axial piston type machines) and digital hydraulic machines lies in the way that oil displacement is controlled. In DD pumps/motors, each pressure chamber is fitted with two valves, which are individually manipulated by use of electronically controlled actuators, as illus-

trated in figure 1.10. A DD pump or motor has multiple pressure chambers individually controlled. By changing the state of the valves for a given pressure chamber, it is possible to select either pumping, motoring or idling action of the chambers, giving the possibility of selecting the displacement in discrete steps. A chamber may, for instance, be set in idling operation by keeping the LPV open during a complete cycle. Pumping or motoring operation of a chamber may be obtained by controlling the LPV and the HPV to appropriate states according to the piston movement. Idling chambers (not contributing to the machine displacement) are not pressurized, leading to improved part load efficiency compared to traditional displacement machines. A number of features in DD machines gives high efficiency - more details on this and the valve control later. Firstly, state of the art within large scale DD machines and hydrostatic transmission based drive trains are presented.

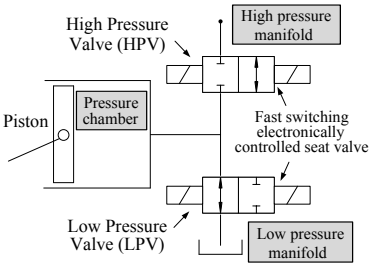

Figure 1.10: *DD pressure chamber configuration. Two valves connects the pressure chamber to the high/low pressure manifold, here shown connected to the low pressure manifold.*

The concept of DD machines were originally developed in the 1980s by a team at Edinburgh University [16], leading to the establishment of the company Artemis Intelligent Power (AIP) in 1994. AIP is forerunner in developing the DD technology, and hold a number of patents within different aspect of the technology. The first and most general patents were filled in 1989 and 1990 and are now expired. In 2010, AIP was acquired by Mitsubishi Heavy Industries (MHI) and progressive work is now being conducted aiming at developing a commercial large scale wind turbine drive train based on the DD technology.

Figure 1.11 shows pictures of the prototype 7 MW drive train with hydrostatic transmission developed by AIP and MHI. The turbine rotor shaft is connected to a ring cam based variable displacement pump, with the low pressure manifold tubing clearly visible in the picture. Two 3.5 MW variable displacement motors (one on each side of the nacelle) drives two synchronous generators each with a rated output of 4.2 MW. Commissioning of a 7 MW prototype wind turbine (SeaAngel) utilizing this prototype drive train is expected to be completed summer 2014 at the SSE Hunterston test facility in Scotland [17].

Detailed information of the DD pump and DD motor used in the above transmission, and in particular the valves used, has not been published. However, some general specifications have been disclosed in [17] and some parameters of this state of the art transmission

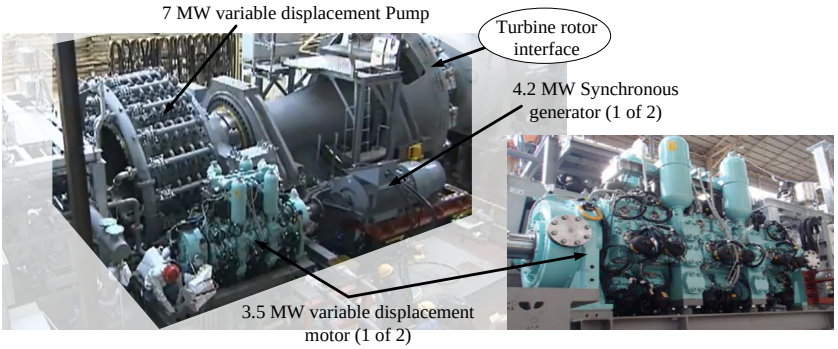

Figure 1.11: *7 MW wind turbine drive train based on a hydrostatic transmission, developed by AIP and MHI [17][18].*

may be estimated from the pictures, patent descriptions [19, 20, 21] and rough calculations. A sum-up of these specifications is given in table 1.2. The synchronous generator connected to each motor has a rated power of 4.2 MW and is directly driven by the DD motor running at 1000 rpm.

Regarding efficiency of the hydrostatic transmission, the general manager of engineering in Mitsubishi Power Systems Europe (part of MHI), Masahide Umaya, is quoted for mentioning that the total efficiency of the transmission is 94 % (98 % for the pump and 96 % for the motors) [22].

Table 1.2: *DD transmission specifications, *estimate, **rough estimate*

	Pump	**Motor**
Rated power	7 (7.4* max) MW	3.5 (3.7* max) MW
Speed	max 10.5 rpm	1000 rpm
Torque	max 7.0 MNm	35.2 kNm
Low operation pressure	<7 bar	<7 bar
High operation pressure	360 bar	360 bar
Size**	⌀4.5 m x 1.5 m	⌀0.8 m x 2 m
Piston displacement* (ideal)	7800 cc/rev	190 cc/rev
Number of pistons	168 (42 x 4)	36 (6 x 6)
Piston bore/stroke**	⌀270 mm x 135 mm	⌀80 mm x 38 mm
Valve config.	Passive + active	Double active
Machine type	Ring cam, radial piston	Radial piston
Piston cycle frequency	max 400** rpm	1000 rpm

Many of the specifications given in table 1.2 are calculated based on [17], wherein details of the rotor speed, transmission pressure, generated power and fraction of active cylinders for the pump and motors during full drive train operation are presented. The sizes of the pump and motor are estimated from the pictures of the drive train, and the piston sizes are estimated from illustrations in patents [20, 19].

The DD pump used in the transmission shown in figure 1.11 is made up of a large number of pistons oriented radially at the circumference with a large hollow rotor shaft at the center, cf. figure 1.12. The pistons are moved by rollers and a ring cam, and each pressure chamber is fitted with an active LPV and a passive HPV. External piping is used to create the low pressure manifold, with individual pipes going to each cylinder. Axial bores and external piping is used for creating the high pressure manifold, as indicated in figure 1.12. The pump is made up of modules, and easy replacement of any part of the pump should be possible according to information in [17].

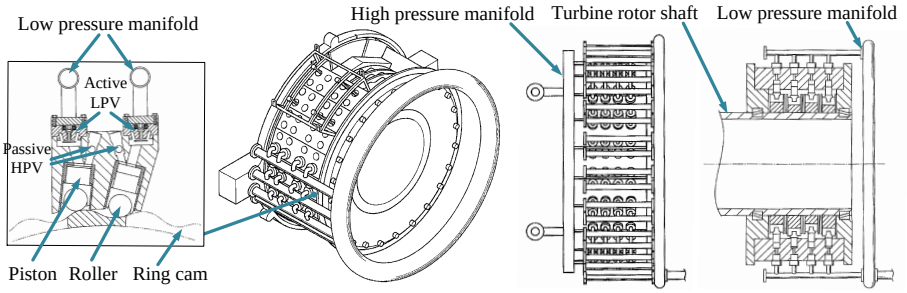

Figure 1.12: *Illustrations of the DD pump unit used in a DD transmission prototype by MHI [20].*

The flow generated by the DD pump drives the two DD motors in the DD transmission. These motors are also fitted with radially oriented pistons, with a number of pistons acting on a common shaft. Figure 1.13 illustrates such a motor construction. Six pistons are arranged on the shaft eccentricity, and six of these slices are acting on the common shaft, driving the generator directly. Active LP valves and HP valves are connected to each pressure chamber, which is controlled according to the needed motor displacement. The motor seen in figure 1.13 is not equal to the one pictured in figure 1.11, but is similar in principle. One main difference, however, is the low pressure manifold. In figure 1.13, the low pressure manifold surrounds the motor itself, whereas the LP manifold in figure 1.11 is realized by other means internally. One obvious benefit of this internal manifold solution is easy access to the valve modules.

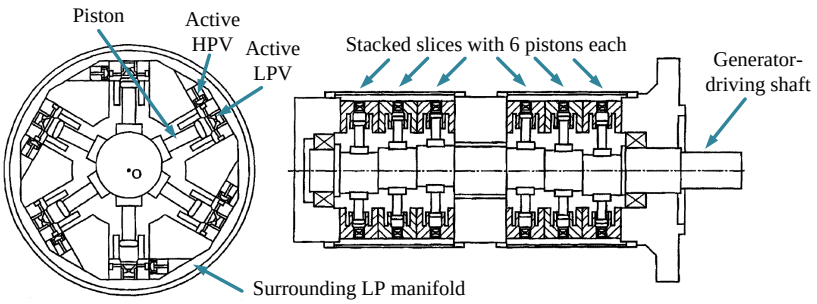

Figure 1.13: *Illustration of DD motor with radially oriented pistons from [23]*

Having some idea of the current state of the art of large power DD units used in wind turbine transmissions, a more general introduction to DD machines and their valves are given.

1.3 Digital hydraulic machines

As previously mentioned, DD machines utilize independent valves connected to each pressure chamber. This concept may generally be illustrated as previously shown in figure 1.10. The core element of the DD technology is the use of leakage free seat valves and relatively weak actuators using only a little power. Such concept is illustrated in figure 1.14. The valves are manipulated directly by electro-magnetic actuators, which are generally much weaker than the pressure forces acting to close the valves against their seats. However, by manipulating the valves at appropriate times according to the piston movement, different modes of operation (pumping/motoring/idling) may be obtained without needing to open the valves against high pressure forces [24].

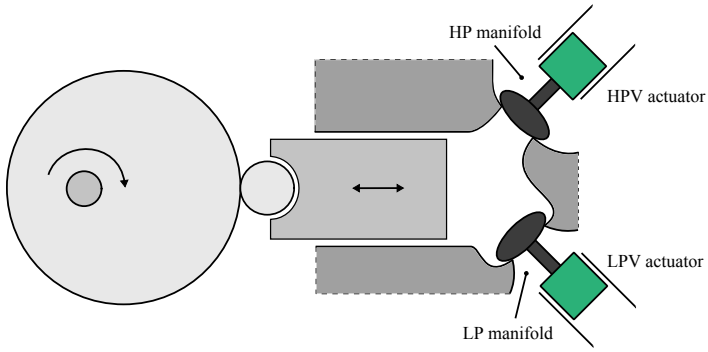

Figure 1.14: *DD pressure chamber with two seat type valves. The seat valves are actuated by relatively weak direct actuators, and the piston cycle is used to equalize the chamber and manifold pressure levels in order to facilitate opening of the seat valves.*

The three operation modes of a DD machine pressure chamber are shown in figure 1.15. Starting from the left, the simplest operation mode is so-called idling, where the LPV is kept open throughout the piston cycle. Oil is thus displaced to and from the LP manifold, with no effective displacement, and the pressure chamber remains at a low level.

In the middle of figure 1.15, the pumping operation mode is illustrated. Here, the LPV is actively closed such that valve closure is obtained at the bottom dead center of the piston movement. The enclosed oil is then pressurized as the piston compresses the chamber, up to the point where the chamber pressure exceeds the HP manifold pressure leading to a passive opening of the HPV. The piston then works to displace pressurized

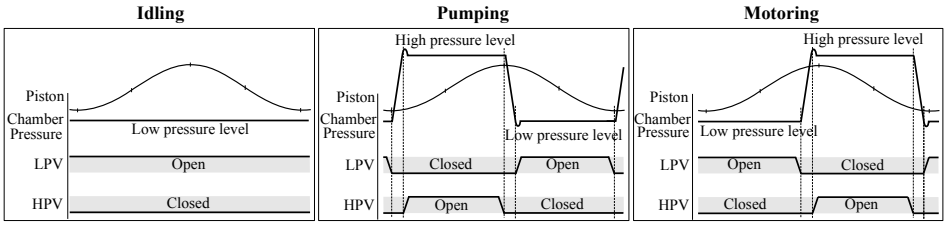

Figure 1.15: *Operation modes of DD machines. Idling, pumping and motoring operation is possible by changing the valve sequence.*

oil to the HP manifold, until the top dead center is approached, at which point the HPV is closed (either actively or passively depending on the machine topology). In turn, the chamber is depressurized following the downward piston movement until the LPV is passively opened when the chamber pressure is equalized with the LP manifold. Oil is then again withdrawn from the LP manifold until the LPV is re-closed to repeat the pumping operation cycle.

The motoring operation cycle (shown to the right in figure 1.15) is slightly more complicated, and requires active closing of both seat valves. During motoring operation, low pressure oil is displaced to the LP manifold as the piston moves from bottom dead center towards the top dead center. At an appropriate time when the piston is nearing the top, the LPV is actively closed leading to a pressurization of the chamber which, in turn, results in a passive opening of the HPV. Having opened the HPV, the piston is driven downward towards bottom dead center, extracting energy from the HP manifold. When the bottom dead center is neared, the HPV is actively closed leading to depressurization of the chamber allowing the LPV to open before the piston reach bottom dead center, and the resulting low pressure oil is then displaced to the LP manifold. Using the piston to pressurize the chamber eliminates the need for opening the HPV against high pressure forces, but it requires sufficient kinetic energy in the shaft to pressurize the chamber. Therefore, motoring operation is not available from zero rotational velocity without additional valve features.

A few comments to the above operation cycles:

- Both opening and closing forces are in general required from the valve actuator systems (closing force and holding force in the open position during displacement). However, the holding force may be realized by passive components, that is, preloaded springs or permanent magnets.

- Using passive means of providing opening holding force, idling operation may be obtained without actuator energy loss.

- Pumping may be obtained with an active LPV actuator only, where the HPV is kept default closed with a weak spring, which is opposed by the chamber pressure during pumping displacement to the HP manifold. If realized like this, the only valve timing aspect is LPV closing at the bottom dead center, and the remaining valve transitions happen passively during the cycle.

- Motoring is the most complicated cycle as it requires both valves to be closed actively, and the ideal valve timing includes estimating the effective oil stiffness, as opening the valves is a three step process before the piston reach top/bottom dead center.
- As part of the piston displacement is used for pressurizing/depressurizing of the chamber, the effective displacement may be significantly below the ideal piston displacement, especially for motoring in designs with large dead volumes. This should be taken into account when dimensioning DD machines.

Variable displacement control of DD machines

Having multiple pressure chambers operated in different operation modes as described above, variable displacement of the DD pump or motor in discrete steps is possible. The operation mode of each pressure chamber may be changed on a turn to turn basis, giving high displacement control bandwidth (assuming high piston displacement frequency). The displacement control resolution depends on the number of pistons per cycle, and the bandwidth is determined by the revolution speed and the number of cams in case of a cam ring concept.

Depending on the needed displacement of the machine, the pressure chambers are enabled and disabled in an appropriate sequence. If the machine is operated using some flow reference, a suitable technique for generating the desired mean flow is Delta-sigma modulation [25]. This modulation converts a given decimal number in range 0-1 into a stream of bits which may be used for enabling/idling the machine cylinders, as illustrated in figure 1.16. The effect of decreased displacement at higher operation pressures due to oil compressibility may be included when generating the displacement ratio (0-1) for accurate flow control.

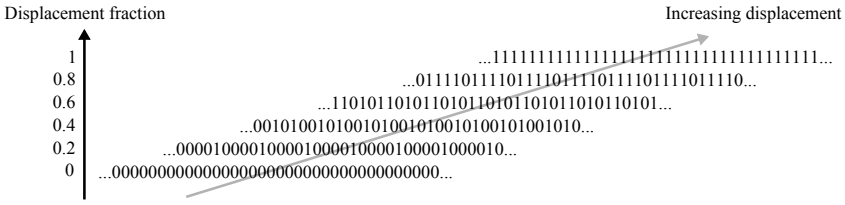

Figure 1.16: *Bit stream for increasing displacement fraction, the sequence of 0's and 1's is used for enabling/idling the individual cylinders leading to the desired mean displacement over time.*

Another technique is to utilize pressure control, where the decision to enable or idle each chamber is performed based on a pressure reference, measured pressure, history of previously enabled cylinder and system compliance [26, 25]. Ultimately, both methods outputs a bit stream for the cylinders to follow depending on the given operation point. Hydraulic accumulators may be used to limit the inherent pressure ripples resulting from the modulated machine displacement.

Efficiency of DD machines

As shown above, high bandwidth variable displacement control is a feature of the individual valve control of DD machines. In addition, a number of features of DD machines make it possible to obtain high efficiency in a broad operation range, opening new application areas for fluid power machines including wind turbine transmissions. These beneficial properties of DD machines when compared to traditional variable displacement machines are summarized below:

- Cylinders not contributing effectively to machine displacement are not pressurized, eliminating leakage from these idling cylinders. Furthermore, the flexibility of the piston/cylinder members may be utilized such that the sealing gaps are relatively large during idling operation, leading to very small friction losses of idling cylinders. Low energy loss of unused cylinders is the key for obtaining high part load efficiency.

- Using a radial piston base unit, the pressure chamber valves may be positioned at the outer circumference with room for generous opening areas, leading to low flow losses both for idling and enabled cylinders.

- Near zero leakage is associated with the valves, as these are seat valves without pilot stage or other leakage paths.

- Throttling losses due to sudden pressure equalization are eliminated independently of the operation pressure. The valves are self-acting during valve opening, and open passively when the chamber and manifold pressure is equalized.

- The electro-magnetic actuators are not required to overcome large pressure forces, and may therefore be compact and use little power.

These above advantages are also discussed in [27, 16]. Figure 1.17 shows the measured efficiency of a DD pump, a bent-axis variable displacement pump and a swash-plate type variable displacement pump. All pumps are rated for 175 kW power [28]. The effect of the above listed advantages of DD machines is clearly seen. At full displacement the DD pump is seen to exhibit a peak efficiency just above 95 % having losses much lower than the other pump types. For variable displacement the efficiency of the DD pump is also seen to be superior, with an efficiency of 92 % at 20 % displacement.

The specific equation for evaluating the efficiencies shown in figure 1.17 is not given, but the efficiency may have been determined with a simplified expression as:

$$\eta = \frac{Q_{out}\,\Delta p}{\tau\,\omega} \tag{1.1}$$

where η is the total pump efficiency, Q_{out} the measured flow output, Δp the generated pressure difference, τ the input torque and ω the rotational speed. In this case, the compression energy (which may be extracted again during decompression) is not included in the pump output, lowering the calculated efficiency. The compression energy may be

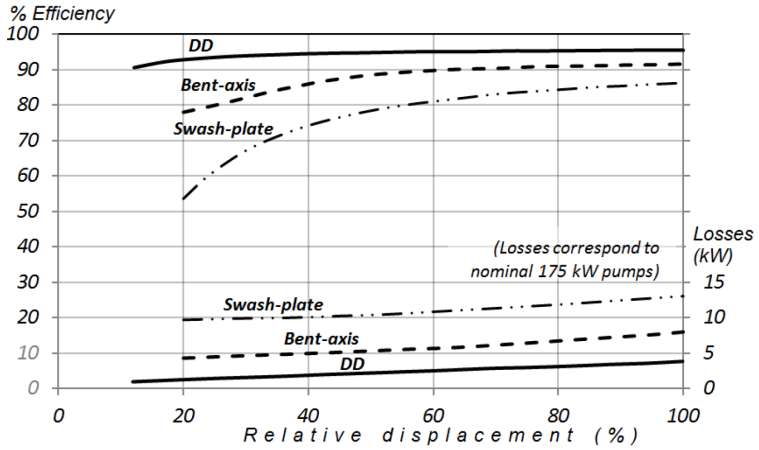

Figure 1.17: *Measured efficiency comparison between a 175 kW DD pump and corresponding curves for bent-axis and swash-plate type variable displacement pumps from [28]. The curves are taken at a fixed rotation speed of 1500 rpm.*

closely approximated by [29]:

$$E_{comp} = \frac{Q_{out}\Delta p^2}{2\beta} \Rightarrow \eta = \frac{Q_{out}\,\Delta p}{\tau\,\omega}\left(1 + \frac{\Delta p}{2\beta}\right) \tag{1.2}$$

with β being the oil stiffness, assumed to be constant. Inserting typical stiffness values, $\beta = 16000$ bar, and an operation pressure difference, $\Delta p = 350$ bar gives an 'increase' in efficiency of approximately 1 %. In total, the measured efficiency of the DD pump at 100 % and 20 % displacement may be as high as 96 % and 93 % respectively.

Existing DD machines and developments

The above mentioned DD machines represent state of the art of DD machines for wind turbine and automotive applications, and are all developed by AIP and lately also MHI.

Generally, DD pumps/motors, as described above, are part of the field of digital fluid power characterized in that discrete valued components are used actively to control the system output [30]. Also, for a general survey of the digital fluid power field, see [30]. Different branches of digital fluid power exist, with one being individual control of machine pistons with active on/off valves, here referred to as digital hydraulic machines or simply digital machines. A small number of developments, besides those driven by AIP, exist in this field.

A research team located at Tampere University of Technology has published their results on developing a digital hydraulic pump/motor prototype with individual active on/off valves for each piston [31, 32, 33]. The results given in [32] concerns a six piston boxer pump with a total displacement of 30 cc/rev (displacement not directly mentioned in

[32], but similar setup as in [34]), fitted with valves capable of switching in about 1 ms while having a flow rate of 23 l/min at 5 bar pressure difference. Here, a maximum total efficiency of 85 % is reported across a speed range of 500-1000 rpm and high pressure level range 20-180 bar (maximum power 8.5 kW). Furthermore, 30-80 % total efficiency were found for partial displacements in the range 6-60 %. Compared to the DD efficiencies shown in figure 1.17, the efficiencies reported in [32] are low, in particular at part displacements. Plausible reasons for the lowered efficiency are larger valve pressure loss, valve leakage and increased mechanical friction in the boxer pump. The valves used in [32] are pressure compensated and thus capable of opening against high pressure differential, which gives flexibility in motoring operation (zero velocity start-up possible), but introduces valve leakage, which is also present during idling, hence resulting in lowered part load efficiency. It seems that the focus of this research is more into different operation strategies and flexibility on a system basis, in particular with multiple consumers connected to each pressure chambers, than on obtaining the highest possible efficiency of the digital pump/motor machine itself.

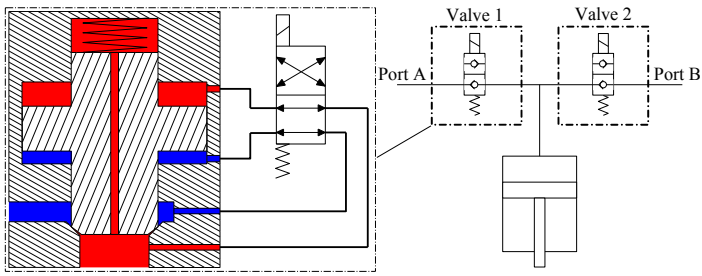

Figure 1.18: *Valve set for active piston displacement control presented in [35]. Each two-stage valve is operated as a bi-directional check valve.*

Another research team from Purdue University has also investigated digital hydraulic pump/motor machines, as reported in the papers [35, 36, 37]. Their approach is to use a set of two-stage valves for each piston, which is operated as bi-directional check valves, as illustrated in figure 1.18. By actively changing the working direction of the check valves, different modes of operation are obtained. In [35], experimental measurements are performed with a single piston pump running at 500 rpm and having a displacement of 3.2 cc/rev. The bi-directional check valve is realized using commercially available components. Different operation modes (full displacement, partial displacement and idling) are successfully tested by changing the state of the bi-directional check valve according to the piston movement. Partial displacement is obtained by utilizing only a part of the piston stroke, that is, the state of the check valve is changed at some point as the piston is moving towards top dead center. Another partial mode is also investigated, where the chamber is closed during piston movement towards bottom dead center, and intentionally cavitated to reduce the oil intake volume, also resulting in partial pumping. No information on the efficiency of the machine is given in [35]. However, a maximum pressure drop of approximately 4 bar is seen during idling operation, which is relatively large compared to the output pressure of 38 bar. In addition, leakage is present in the two-stage valve. In order to obtain very high efficiencies, a challenge with the valve setup

illustrated in figure 1.18, is that only passive switching is possible, which requires notable pressure difference in order to accommodate fast switching. This, in turn, inherently increases the energy losses, which degrades the machine efficiency.

As initial study into the development of DD machines, a prototype single piston DD pump has been developed and tested by the author and Per Johansen in their Master's project. Detailed information of this study may be found in [25]. This 3 cc/rev unit is illustrated in figure 1.19. A bi-directional solenoid actuator was used for actively manipulating the position of the LP valve, and the valve assembly was made as an integrated part of the pressure chamber. A passive check valve was used to connect the HP manifold.

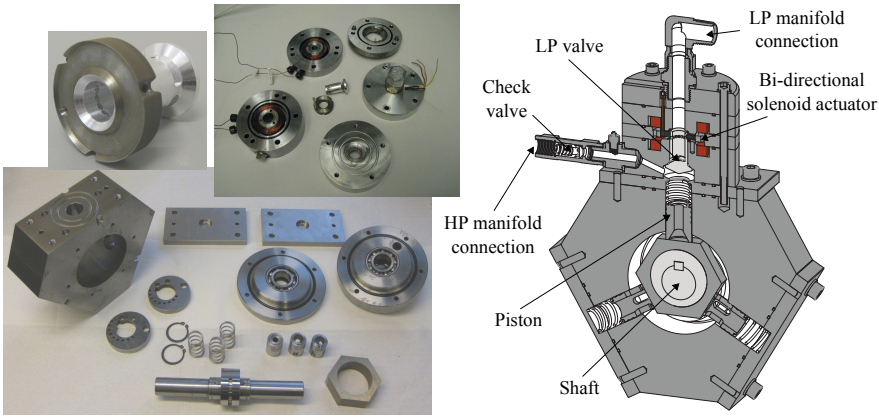

Figure 1.19: *Prototype single piston DD pump designed and constructed in 2011 by Roemer and Johansen [25].*

Primary focus in this study was on development of a LP valve enabling high efficiency operation of a DD pump unit. By experimental measurements, the developed directly-actuated valve was shown to have a closing time of approximately 3 ms and exhibit a pressure drop below 0.1 bar at 10 l/min. Successful operation in both pumping and idling was also verified by measurements with output pressures up to 250 bar. The prototype piston unit did, however, exhibit some problems with excessive leakage, and the measured efficiency was therefore low.

All other DD machines, than those described above, seem to be developed by AIP or in cooperation with AIP. Sauer-Danfoss (now, Danfoss Power Solutions) has a long-standing relationship with AIP on introducing DD machines to the off-road market, and Bosch Rexroth has a licensing agreement for DD machines in on-road equipment [38], but no commercial pumps or motors are available yet.

AIP and their founders have more than 20 years of experience with DD machines, and have developed a number of machines during this period. Some of them are briefly shown in the following. Figure 1.20 show pictures of three DD machines made by AIP. To the

left, the parts of the first DD pump prototype are shown (early 1990s). A six piston radial piston setup was used, with solenoid driven active LP valve and passive spring loaded HP valve. The black LP valve plungers were made of Carbon fiber reinforced PEEK (Poly-Ether-Ether-Ketone, polymer). The six pistons produced a displacement of 18 cc/rev with a power rating of approximately 15 kW (1500 rpm, 350 bar).

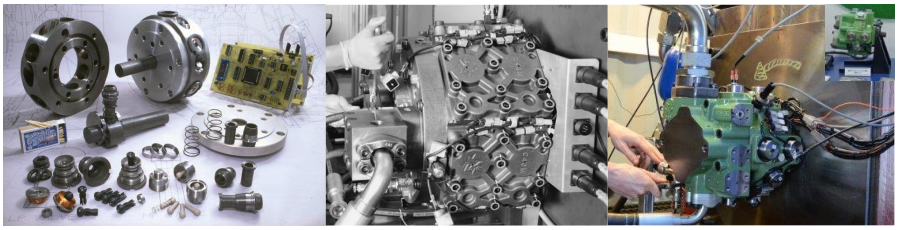

Figure 1.20: *Three DD machines developed by AIP. Left, first DD pump prototype [39]. Middle, 600 kW DD motor for an automotive transmission [28]. Right, recent 96 cc/rev DD pump [39].*

In the middle picture of figure 1.20, a more recent AIP DD pump/motor is shown. It is developed for large commercial vehicle use, with a displacement of 480 cc/rev. With an operation pressure of 350 bar and a maximum rotation speed of 2200 rpm the machine is capable of transmitting about 600 kW [28].

The right picture of figure 1.20 also shows a recently presented DD machine. This 96 cc/rev DD pump is said to be suitable for automotive hydraulic transmissions, as alternative to electric hybrid systems [39].

In addition to the 7 MW transmission shown in section 1.2, AIP has also developed a 1.6 MW hydrostatic transmission. This transmission is a smaller version of the 7 MW transmission, and consist of a slow rotating 1.6 MW ring cam DD pump and two fast rotating 800 kW DD motors. Pictures of the pump and the two motors are shown in figure 1.21. The two motors (shown left, orange color) have a rated speed of 1500 rpm and operate at 350 bar, giving an effective displacement of approximately 920 cc/rev. A surrounding LP manifold is utilized in these 800 kW DD motors, a concept which has been abandoned in the larger 3.5 MW motors shown in figure 1.11 on page 10.

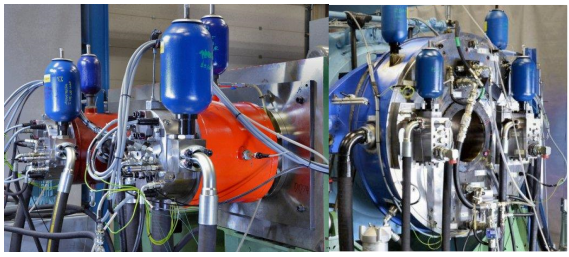

Figure 1.21: *Two 800 kW DD motors (left) and a 1600 kW DD pump (right) developed for a wind turbine hydrostatic transmission [39].*

1.4 Valves for DD machines

Having treated DD machines on a system level, focus is now turned specifically towards the valves in these machines. A review of current fast switching valves is given, and the valves used by AIP are discussed. Following the operation cycle description given in section 1.3, the optimum properties for DD valves for minimizing energy loss during the cycle are:

- Low pressure loss during displacement flow
- Low valve leakage
- Minimum of actuator power loss
- Fast active valve closing with independent and precise timing
- Low moving mass and low friction forces, facilitating quick valve opening driven by pressure forces
- Durability to withstand billions of opening/closing cycles

The above properties may be used to evaluate candidates for DD valves. Hydraulic on/off valves have been developed and used for several decades, why it is tempting to use existing valve technology for DD machines. A large variety of fast switching valves exist, but only a limited number of fast switching valves also feature a low flow coefficient k_f:

$$Q = \frac{1}{k_f}\sqrt{\Delta p} \Rightarrow k_f = \frac{\sqrt{\Delta p}}{Q} \tag{1.3}$$

where Q is the flow rate and Δp the pressure difference. Note that the flow coefficient k_f is defined inversely to the common form where the flow is directly proportional to the square root of the pressure difference. This inverse definition is used throughout the thesis, and as such the flow coefficient must be low to achieve efficient DD machine operation, with an ideal valve having $k_f \to 0$. Figure 1.22 compares a number of known fast switching valves, utilizing both spool plungers and seat plungers with direct and pilot actuation. Switching times of the valves may depend on the pressure levels, and in such case a characteristic value for the switching time is used in the figure, and should therefore be taken as a rough overview. Delays are not included in the switching time.

Referring to figure 1.22, an ideal valve would be placed at the origin. The existing valves having the lowest flow coefficient mostly use actuators based on pilot pressure (squares and stars). An increased switching time is seen for the lowest flow coefficients (MOOG N-DSHR / Parker D-NG10). Some prototype valves with pilot pressure actuator, exhibiting both a low flow coefficient and a low switching time has, however, been developed (Winkler et al, 2010 [45] and Winkler & Scheidl, 2007 [44]).

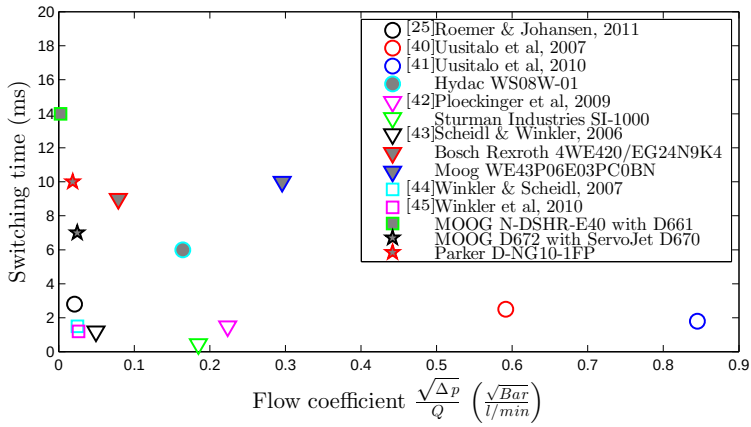

Figure 1.22: *Comparison between different existing fast switching valves. Lower values are better for both axes. Circles: Seat valve with direct actuator, Triangles: Spool valve with direct actuator, Squares: Seat valve with pilot actuator, Stars: Spool valve with pilot actuator. Grey fill: Commercially available, White fill: Prototype. Some valve parameters taken from [46].*

The valves with lowest switching time, below 5 ms, are dominated by prototype valves with direct actuators (circles and triangles), but a couple of valves with pilot pressure actuators are also present (squares). The fastest switching times are reported using spool-type valves, with a minimum of 0.45 ms (Sturman Industries SI-1000). Fast switching seat-type valves are also reported in Uusitalo et al, 2007 [40] and Uusitalo et al, 2010 [41]. However, these exhibit a relatively high flow coefficient.

The black circle valve (Roemer & Johansen, 2011 [25]) is the LP valve developed for the 3 cc/rev DD pump prototype previously mentioned. This valve distinguishes itself from the others by being specifically designed for use in a DD pump, and is therefore only designed to switch at times with low pressure differential. The other valves in figure 1.22 are designed to be capable of opening against high pressure differentials, which gives another set of design specifications, and a direct comparison is somewhat uneven. The best located valves, besides the DD prototype valve (black circle), is either valves with a pilot stage or a spool type valve with direct actuator. These valves typically exhibit leakage, inducing additional energy loss, and the valves with pilot stage actuator is typically somewhat more complicated in structure compared to valves with direct actuators.

The valves used by AIP are not included in figure 1.22 due to lack of information. However, based on the measured efficiencies of their DD units, the valves must be located among the best valves in the figure. If it is possible to develop a seat type valve with a direct actuator, which matches or surpasses the best valves in figure 1.22, it will be superior for the DD application with respect to energy efficiency. Such a valve would exhibit a simple structure, zero/low leakage and possibly a reduced switching delay due to the direct actuator. In the following work focus is therefore on this type of valve setup.

Artemis Intelligent Power DD valves

Some information on the valves developed by AIP is available, mostly from patents and patent applications, where illustrations are included which seem to resemble real valve designs. Together with pictures made available by AIP, these illustrations are presented and described in this section.

All valve assemblies designed by AIP have a cartridge type construction, where the actuator and the moving member are combined and able to be integrated closely with the pressure chamber. Some of the early valve designs developed for small DD units in the late 1980's are shown in figure 1.23. The HPV, shown left, has a permanent magnet latch which keeps the valve held open during displacement flow from/to the pressure chamber. A solenoid actuator is used for actively closing the valve forcing the valve plunger away from the permanent magnet.

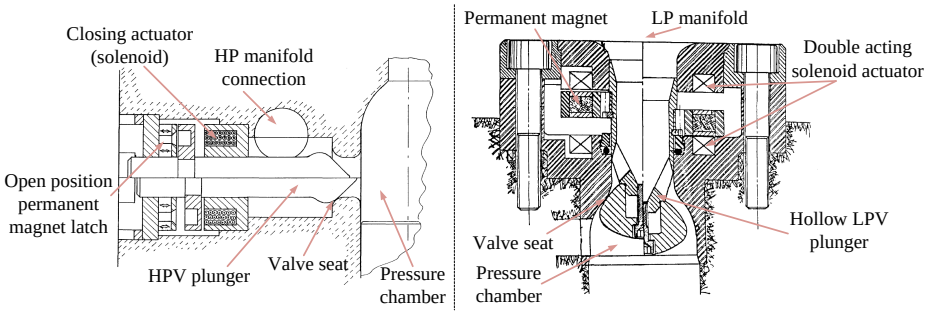

Figure 1.23: *Left, early AIP HPV design for small units shown in [47]. Right, early LPV design also for small units shown in [48].*

The LPV, shown right in figure 1.23, has a hollow plunger giving a nearly straight flow path between the LP manifold and the pressure chamber. A double solenoid actuator is able to apply both opening and closing force to the valve plunger, and a moving magnet is embedded in the moving member giving a bistable effect in this early LPV design (that is, the moving member latches in both the open and the closed position).

To reduce the moving mass while maintaining a large area gradient, valves with annular (ring-shaped) plungers are used for machines with larger displacements. Such design for a LPV is shown in figure 1.24. The plunger is made of carbon fiber reinforced PEEK and a permanent magnet latch is used for maintaining the valve open together with a small spring. A solenoid actuator is used to attract a steel part of the plunger constituting the armature of the actuator.

Annular valves are also used for the HPV in DD motors made by AIP. Figure 1.25 (right) shows a picture where the LPV, HPV and piston assemblies are placed on top of the motor block of the 800 kW DD motor previously mentioned (cf. figure 1.21, left). In addition, a patent application [51] includes the illustration of a HPV shown left in figure

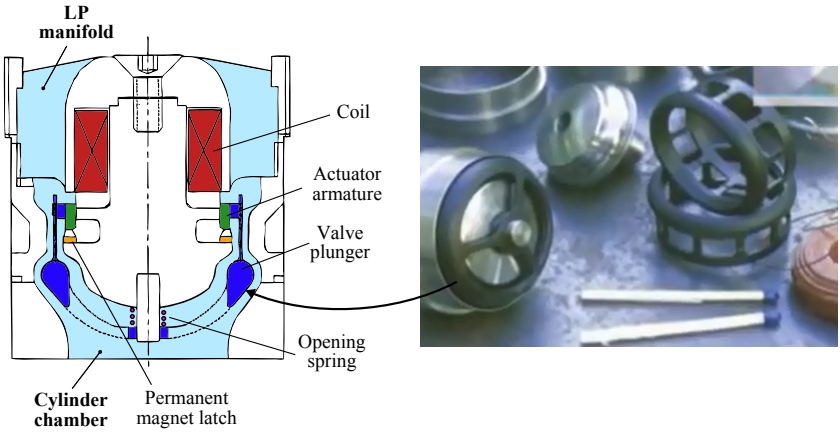

Figure 1.24: *Annular shaped LPV for larger machines, with plunger manufactured in reinforced PEEK [49, 50].*

1.25. The illustrated design show much resemblance with the pictured HPV, and may be close to the actual valve design used by AIP in more recent large scale units.

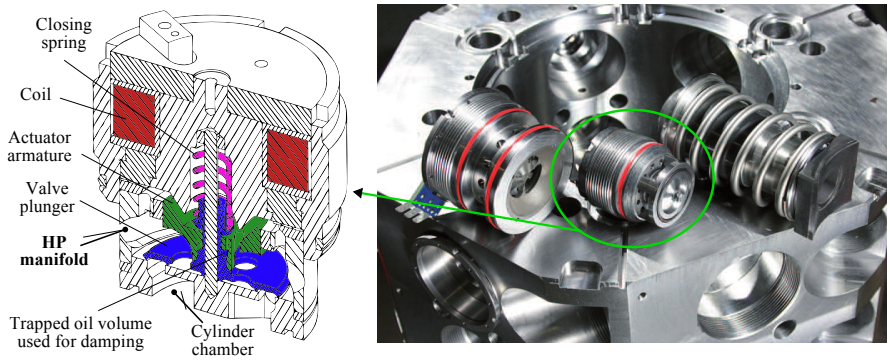

Figure 1.25: *Valves and piston assemblies from 800 kW DD motor (right) [38], and patent illustration showing a HPV design which seem to be very similar [51].*

Referring to figure 1.25, some changes in the HP valve design is seen compared to the early design shown in figure 1.23 (left). Besides being based on an annular type plunger with two flow edges, this HPV is seen to have a spring acting to close the valve, and a solenoid actuator is used to apply opening forces to the valve. This actuator type ensures that, in case of electrical failure, the HP valve is passively closed leading to idling operation of the cylinder (assuming the LP valve is kept open passively). If the HP valve is kept open passively in the event of actuator failure, the cylinder remains

pressurized while oil is displaced from/to the HP manifold, giving an increase in energy loss of the failed cylinder compared to an idling cylinder at low pressure. However, the cost of this improved characteristic in the event of actuator failure is an increase in HPV actuator power needed during normal operation, as the HP valve must be kept actively open against the spring while displacing oil from the HP manifold.

Another valve design feature seen in figure 1.25, is that the moving part of the valve is made up of two individual parts (marked with blue and green color). The green part is able to move some distance relative to the blue part. During valve closing (where the seat contact areas and the plunger impact), this relative movement is used to reduce the load on the contact areas. This is performed by using a small trapped oil volume, with only a small venting port, to absorb the kinetic energy of the green part in figure 1.25.

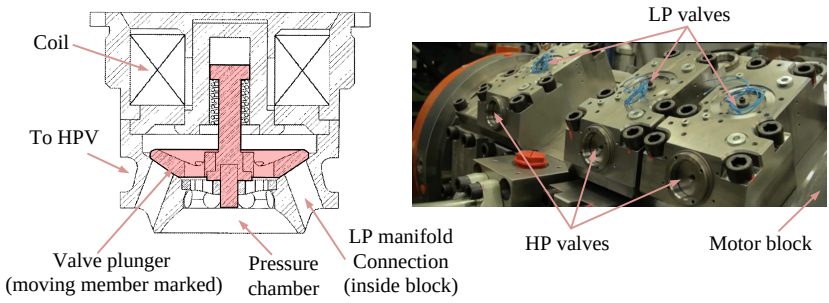

Figure 1.26: *Close-up picture of a 3.5 MW DD motor using internal LP manifold, with three valve modules visible (right) [18], and a LPV design facilitating internal LP manifold (left) [52].*

An external realization of the LP manifold (surrounding the unit) gives easy flow access with low pressure loss to the cylinders, but also imposes challenges with regard to the ease of performing service and maintenance. Alternatively, the LP manifold may be realized internally, allowing for the valves to be more easily replaced. One LPV design facilitating such internal LP manifold is shown to the left in figure 1.26, and may resemble more recent LP valves made by AIP. The moving part of the LPV is marked in red color, and the connection to the internal LP manifold is seen. The pressure chamber extends through holes in the plunger to the top side of the plunger disk. A spring is used for supplying a passive opening force, and a solenoid actuator is used for active valve closing.

As previously mentioned, the valves are not capable of opening against higher pressure differentials. Motoring operation thus relies on pressurization of the chamber by piston movement. When sufficient rotational energy is present, this limitation has no effect. However, start-up from zero velocity is not directly possible. In a wind turbine transmission, this initial start-up may be conducted by some external means, but for other applications this may limit the use of DD motors. A possible solution for this limitation is pointed out in [53], where a small parallel seat valve is embedded in the HP valve design, which may be opened against a high pressure differential, allowing the chamber to be pressurized close to zero speed to start rotation of the DD motor.

1.5 Aims and focus of the research

The overall aim of the research presented in this thesis has been to analyze, design and optimize fast switching valves needed in large scale DD motors. That is, the LP valve and the HP valve as outlined in the above introduction.

These valves are rather complex components to design, in the sense that multiple design aspects are present in these integrated valve units, with a number of conflicting objectives and interdependencies. Even though it is possible to model and analyze nearly all aspects of such valve units with reasonable accuracy, a general and complete model leading to optimum valve designs with all thinkable technological possibilities does not exist.

The designer is therefore left with the task of selecting some initial design, perhaps based on analysis of relatively simple models, inspiration from existing solutions, rough calculations or simply a good idea. This initial design is then subject to optimization which ideally lead to the best configuration of the chosen design given some constraints and objectives. Such an optimized design may be the global optimum, but is likely just a local optimum among a number of other local design optima corresponding to other initial design choices.

Even though globally optimal designs cannot be ensured, very good designs may be obtained by carefully selecting an initial design and subsequently optimizing the chosen design. An overview of the above described work flow when developing valves is illustrated in figure 1.27. The preface ends with the selection of some initial valve topology, which is then refined in the optimization design phase. Model based evaluation then determines whether or not the resulting configuration is acceptable for further work in the finalizing phase, ultimately leading to the final valve product.

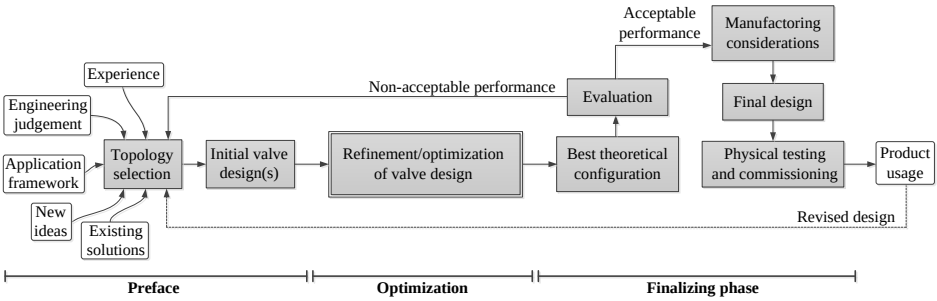

Figure 1.27: *Work flow during the valve design process. The process may be regarded as three main parts as indicated, with the optimization part being the main aim of the current research.*

All three phases (preface/optimization/finalizing) is covered to some extend in the present work, however, primary focus and aim of the research has been on the development of methods for the optimization part. Within the target application of DD machines, the methods should be widely useable, in the sense that the methods may be used independent of the specific initial design selected. The chosen reference/initial

designs in the presented work are based on preliminary calculations and basic reasoning considering the common valve topologies and actuator principles.

The initial designs were developed with the objective of creating the best possible valve setup, but shortcomings have later been identified. Especially the choice of using similar valve geometry for both the LPV and the HPV, for simplicity, seemed like an intriguing basis for development. However, due to increased stiction effects at high pressure levels, this design choice is not ideal and separate designs of the LP and HP valves seem more appropriate.

Experimental validation of the developed methods and models has also been aimed as part of the research, and a range of measurements have been conducted on three physical prototypes of valves and electro-magnetic actuators.

1.6 Main Contributions

An overview of the state of the art within digital hydraulic machines, with special focus on large scale units and their fast switching valves, has been conducted and used as basis in the valve topology selection.

A small scale digital hydraulic pump has been experimentally tested and a method for modeling the transient response of a seat valve in such units has been developed. Satisfactory performance of this small scale valve during idling and pumping operation was found both by simulations and experimental measurements.

A general method for specifying the valve requirements for digital motors has been developed. The requirements are set in terms of the valve flow coefficient and switching time in order to obtain a given target efficiency for arbitrary displacement volumes and rotation speeds. This method is useful in the valve design phase, as it does not require specific geometry or size information.

Using a transient 3D Computational Fluid Dynamics (CFD) model, detailed analysis of a large scale pressure chamber have been conducted and found to be operational with relatively weak valve actuators and passive springs as expected. The transient CFD was found to be computationally expensive and require a large effort for developing a suitable computational mesh. Therefore, a Lumped Parameter Model (LPM) method has been developed and shown to exhibit similar dynamic response while being computationally inexpensive to conduct.

A method for analyzing material stresses in the valve seat and valve plunger under pressure loading has been developed. This method is based on non-linear structural Finite Element Analysis (FEA), where contact elements are used to describe the valve seat surfaces and a fluid pressure penetrating load is applied to model the seat valve loading.

A design guideline for selecting the valve seat angle and stroke length with basis in the valve flow coefficient has been presented. Following this guideline, the selection of the valve stroke length is performed from data generated using steady CFD simulations.

Taking basis in the Reynolds equation, a stiction model for annular seat valves has been developed. This stiction model includes cavitation in the liquid squeeze film by utilizing different solution cases, and includes the possibility of liquid tension in some regions of the liquid film. Using this capability of including liquid tension, worst case studies of the valve stiction may be performed.

A method for evaluating the valve actuator performance in terms of valve switching time has also been developed. In this method, transient electro-magnetic FEA is used to simulate to transient actuator force build-up, while coupled to a model of the fluid opposing forces and an electronic circuit model.

A complete design method for seat valves suitable to digital hydraulic motors, including a number of the above methods, has been developed. This design method takes basis in a given valve topology and machine specifications. A number of subdomains within the valve design are optimized as part of the design method, and supporting studies are conducted to ensure a suitable framework for the valve optimization. The design method has been shown applied to an example valve design, suitable for a large scale digital motors, resulting in a design giving high-efficiency motor operation.

The transient force build-up, as predicted by the transient electro-magnetic actuator FEA, have been experimentally validated. This validation is performed on a prototype reflecting the design found using the above valve design method.

1.7 Reading guidelines

This dissertation consists of an extended summary and the appended collection of papers. The extended summary contains all main results and contributions of the project research, and the papers should thus be seen as supplementary material where additional details may be found. For some passages of the extended summary, appropriate text and figures from the papers have been directly inserted. References to specific appended papers are given throughout the extended summary.

The extended summary is divided into four chapters in addition to the introduction and the concluding chapter. A brief introduction to these chapters is given below:

Chapter 2: Preliminary Valve Studies This chapter presents studies on a small scale digital pump. Specific focus is on the modeling and the performance of an active LPV which has been specifically designed to gain experience in the field of DD valves. Acceptable performance and modeling results are found.

Chapter 3: Supporting Studies for Large Scale Valves Having studied a small scale valve, attention is turned towards large scale units and valves suitable for such units. A method for setting appropriate valve requirements is presented, and a valve topology is selected for further studies. Utilizing this chosen valve topology, detailed analysis of a motor pressure chamber is conducted using both a transient CFD simulation and a simplified analysis model.

Chapter 4: Optimization Method for Digital Motor Valves A valve design method is here presented, including a number of steps where different analysis methods are applied. The method is shown applied to the chosen valve topology, which leads to a valve design ensuring high efficiency operation of a target digital hydraulic motor.

Chapter 5: Experimental Results on Valve Prototype The valve design obtained in chapter 4 is manufactured, and a validation of the transient actuator performance when compared to simulations is given here. Manufacturing challenges with the composite material chosen for the valve plunger is then discussed.

Chapter 2

Preliminary Valve Studies

Studies and measurements based on a LP valve dimensioned for a small scale DD pump are presented in this chapter. The simulation models and engineering challenges for valves suitable to large scale DD units are somewhat similar to the ones for much smaller units, and a small unit is chosen for simplicity in these preliminary studies into the design and control of DD valves. For pumping operation, only an active LP valve is needed, making it possible to explore DD operation with a single valve prototype, serving as basis for further developments.

The valve design, construction and measurements, forming the basis for the following studies, were presented in [25]. The small scale pump unit fitted with this prototype LP valve was shown in figure 1.19 on page 18. A bi-directional, solenoid type, electromagnetic linear actuator was used as direct actuator, and the LPV flow path was designed with focus on minimizing flow losses. This design shares some similarities with some existing valves developed by AIP, giving insight into the characteristics of current state of the art DD valves.

Further details regarding the studies shown in this chapter may be seen in the papers [A] and [B]. The pumping operation measurements shown in the last part of this chapter has not previously been published.

2.1 Prototype LP valve and displacement unit

The prototype LP valve is presented in figure 2.1. Flow is conducted through the inside of the valve plunger, and the plunger is attracted to the open or closed position by linear actuators.

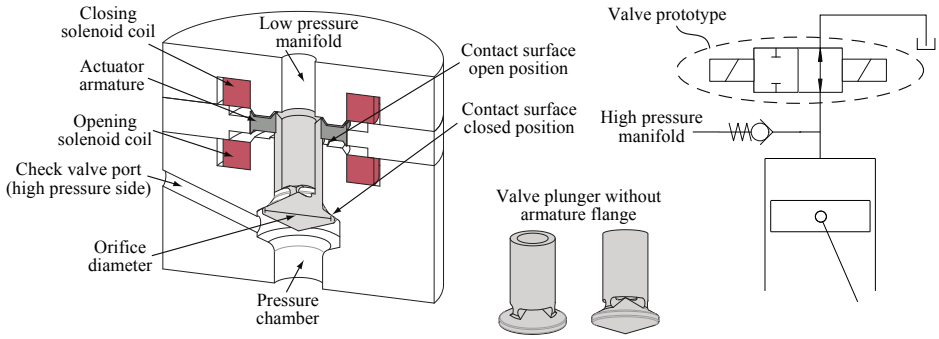

Figure 2.1: *Prototype LP valve section view. A passive check valve is used as HP valve.*

To obtain a fast switching valve, the mass of the plunger and actuation flange were sought reduced by considering material stresses that were calculated using structural FEA, and an aluminum alloy was chosen as plunger material. Furthermore, the end position contact surfaces were made small and a relatively loose guidance tolerance was selected to minimize valve movement friction forces. The actuator flange was designed with conical parts at the inner and outer radius [54], leading to an enhanced available force in the weak actuator positions with large air gaps, compared to an actuator using purely flat parallel surfaces. This improved the force vs. position actuator characteristics.

Specifications of the prototype LPV and the displacement unit are given in table 2.1.

Table 2.1: *Specifications of prototype LP valve and displacement unit.*

Orifice diameter	21 mm	Displacement	3.1 cc/rev
Stroke length	1.55 mm	Piston stroke/diameter	7.5/23 mm
Moving mass	39 g	Rotation speed	1500 rpm
Closing switching time	3 ms	Max displacement flow rate	14.7 l/min
Pressure loss @ 10 l/min	<0.1 bar	Max operation pressure	350 bar

The actuator applies opening or closing force to the valve plunger by use of two variable reluctance circuits (solenoids), as illustrated in figure 2.2. Energizing the upper coil will tend to generate a closing force, as the magnetic circuit seek to minimize the magnetic path reluctance. Low carbon steel is used for creating the valve actuator circuits. Laminations are not included in the magnetic path of the actuator, due to the impracticality of including these laminations in the axisymmetric design.

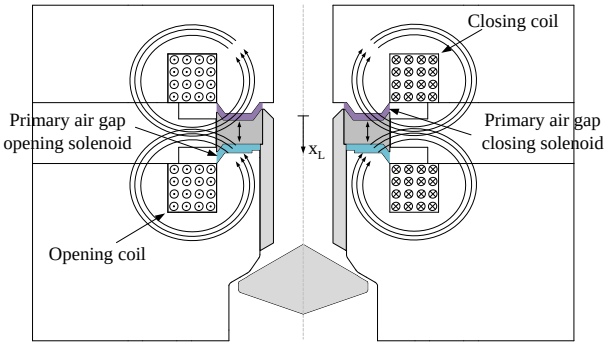

Figure 2.2: *Valve prototype actuator, opening and closing force may be generated by energizing the corresponding coil.*

2.2 Valve modeling in preliminary study

A valve model is used for simulating the behavior of the prototype LP valve. Two expressions are utilized for describing the valve dynamics and the flow rate:

$$m\,\ddot{x} = F_{act}(x,i,t) - F_{damp}(x,\dot{x}) - F_{stic}(x,\dot{x},t) + A_s\Delta p - F_{flow}(Q,x) \tag{2.1}$$

$$Q = C_d(Re)\,A\sqrt{\frac{2}{\rho}|\Delta\, p|}\; sign(\Delta p) \tag{2.2}$$

where F_{act} is the actuator force, F_{damp} the force arising from motion damping and F_{stic} the force resulting from stiction effects (termed suction in papers [A,B]). In addition, Δp is the pressure difference, A_s the shadow area, Q the orifice flow rate, C_d the discharge coefficient, Re the Reynolds number at the orifice, A the orifice area, m the moving mass and ρ the oil density. The valve position x, actuator current i and pressure p are all functions of time.

Both the damping force F_{damp} and the stiction force F_{stic} give rise to opposing friction force, and the separation in two distinct terms is somewhat elusive as both origins from fluid restrictive forces. Increased friction forces are present when moving the plunger close to the end positions, both when impacting a contact surface and when driving away from a contact surface. The term F_{damp} accounts for friction far away from the end positions and when impacting the end positions, whereas the term F_{stic} accounts for friction force when driving away from an end stop.

The flow force F_{flow} generally acts to close the valve, and may be estimated using common techniques [55]. Because DD valves exhibit large opening areas with low fluid velocities, the flow forces tend to be relatively small. A brief sum up of the remaining valve model functions is given next.

Actuator force model

When initially trying to model the solenoid actuator, a relatively simple linear magnetic reluctance model was assumed to be adequate for describing the behavior of the actuator. As such, the initial model strategy was to model the self-inductance L and actuator force F using the expressions [56]:

$$L(x) = \frac{N^2}{\mathcal{R}_{eq}(x)} \tag{2.3}$$

$$F(x,i) = \frac{1}{2}\frac{\partial L(x)}{\partial x}\, i^2 = -\frac{1}{2} N^2\, i^2\, \frac{\frac{d}{dx}\left(\mathcal{R}_{eq}(x)\right)}{\mathcal{R}_{eq}(x)^2} \tag{2.4}$$

where N is the number of turns and $\mathcal{R}_{eq}$ is the equivalent magnetic reluctance seen by the coil. The solenoid actuators were designed to operate mainly in the linear magnetic region of the steel path, and the steel path reluctance were therefore neglected for simplicity. A lumped parameter approximation of the equivalent reluctance as function of the armature position, $\mathcal{R}_{eq}(x)$, was then applied based on the actuator geometry (see paper [A] for details). Following the model in (2.3)-(2.4), the actuator force depends on the position of the armature (flange), x, and on the coil current, i, as expected. However during experimental measurements, the actuator force was found to also depend directly on time due to the effects of magnetic diffusion. That is, the actuator force build-up was delayed significantly compared to that expected from the coil current. This diffusion/delay effect has been found significant for non-laminated solenoid actuators when aiming for switching times in the millisecond range.

The term magnetic diffusion (or magnetic field diffusion [57]) covers the effect that it takes some time for magnetic flux to diffuse into electrically conducting material. This transient effect is interconnected to the presence of Eddy-currents seeking to prevent changes in magnetic flux. Seen from the coil, these Eddy-currents effectively decrease the magnetic flux linking the coil (transiently). This corresponds to a transient increase in magnetic reluctance $\mathcal{R}$, leading to a decrease in self-inductance and generated force, cf. (2.3)-(2.4).

To account for the magnetic diffusion effect, a model as illustrated in figure 2.3 has been utilized for approximating the dynamic behavior of the solenoid actuator.

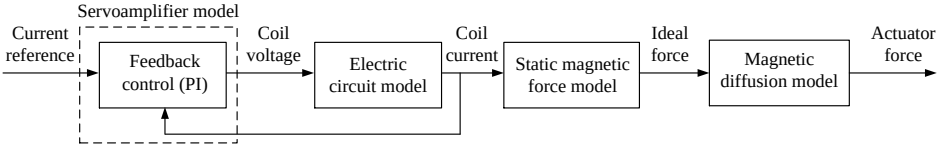

Figure 2.3: *Solenoid actuator model overview. The static magnetic force model is based on equation (2.4).*

The static magnetic force model, as shown in (2.4), is expanded by a magnetic diffusion model and the inductance used in the electric circuit model is set considering the effect

of Eddy-currents. These magnetic diffusion related parts of the actuator model are determined based on transient electromagnetic FEA simulations.

Figure 2.4 shows such FEA simulated transient actuator forces and corresponding voltage and current responses. The simulations are conducted by applying a voltage step which is followed by a constant current source when the rated current level is reached, cf. figure 2.4 (right). The effects of magnetic diffusion and Eddy currents are clearly seen, as the coil currents rise to the rated level in approximately 0.5 ms, whereas the actuator force rise is significantly slower. When targeting valve switching times in the ms range, this force rise time therefore needs to be taken into consideration.

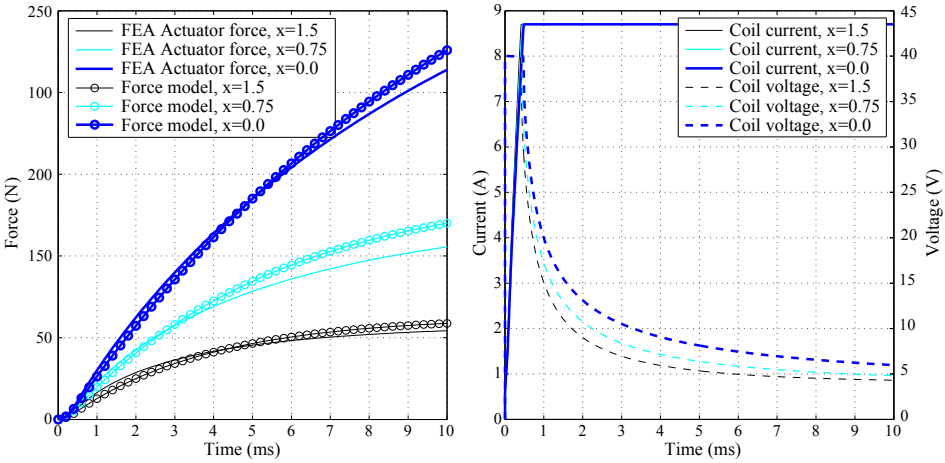

Figure 2.4: *Transient actuator force simulations, for three plunger positions, with corresponding voltages and currents. A simple first order actuator force model is plotted along with the FEM simulation results.*

For the actuator diffusion model a first order system with a position dependent time constant is utilized as an approximation. The time constant is set proportional to the static self-inductance and determined based on the FEA simulations, cf. paper [A]. The resulting force response of the diffusion model is also shown in figure 2.4.

Damping force

When moving in oil, viscous damping forces act on the valve plunger. The model found to approximate this damping force, in the preliminary studies, includes a viscous term proportional to the plunger velocity $\dot{x}$ and a drag term proportional to the velocity squared:

$$F_{damp} = B_v\left(x, \text{sign}(\dot{x})\right)\,\dot{x} + B_D\,\text{sign}(\dot{x})\,\dot{x}^2 \tag{2.5}$$

where B_D is a constant drag coefficient and the viscous damping coefficient $B_v\left(x, \text{sign}(\dot{x})\right)$ is modeled as the sum of a constant term and a position dependent term to account for

the increased damping present near the end positions of the plunger movement. That is,

$$B_v = \begin{cases} B_0 + B_{near,op}\, e^{-\frac{l_{sl}-x}{x_{0,op}}} & \text{for} \quad \dot{x} > 0 \\ B_0 + B_{near,cl}\, e^{-\frac{x}{x_{0,cl}}} & \text{for} \quad \dot{x} < 0 \end{cases} \tag{2.6}$$

where the coefficients $x_{0,op}$ and $x_{0,cl}$, influences the rate of decrease for the exponential terms and denotes the distance where the exponential term has decreased to ∼37%. The constant damping term B_0 sets the minimum value of B_v, which is dominant for plunger positions away from the open and closed positions. The coefficients are determined based on experimental measurements. As later research has shown, other terms also influence the opposing fluid forces, cf. section 4.7.

Stiction force in preliminary studies

The term stiction is used to describe the force required to quickly separate two surfaces placed closely together [58, 59]. Large stiction forces may arise when quickly opening the valves in DD machines, especially the HP valve which is forced open by the chamber pressure at high pressure levels. The stiction force is limited by cavitation, as liquid tension (negative pressures) only briefly persists before vaporization occurs in the fluid gap.

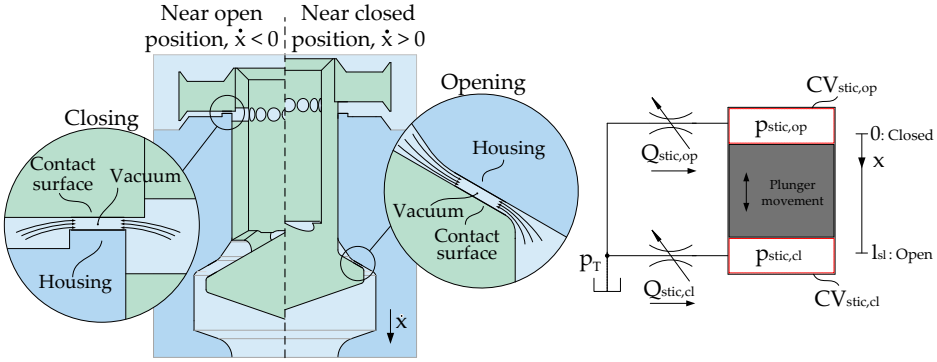

Figure 2.5: *Plunger stiction principle and the utilized stiction model in the preliminary valve study.*

Stiction forces, denoted F_{stic}, were modeled in the preliminary study by considering two fictive control volumes affected by the plunger movement and connected to two variable orifices, as illustrated in figure 2.5. To obtain the wanted stiction effect, where a vacuum is created when driving the plunger away from contact, the variable orifice is chosen to be a function of the plunger position. In particular, each flow ($Q_{stic,op}$ and $Q_{stic,cl}$) is determined as $Q = k(x+h_i)^3\Delta p$, where k is an adjusted proportional factor, h_i an initial height and Δp the pressure difference across the fictive orifice. This relation between the pressure difference and the flow rate is inspired from laminar flow between two parallel plates.

The pressures in the fictive control volumes are calculated with basis in the continuity equation, where pressure dependent oil stiffness is included to somehow account for cavitation effects. Finally the resulting control volume pressures are translated into the stiction force F_{stic}, using a characteristic area. Further details on this approach may be found in paper [A].

The stiction model outlined above has a number of parameters not directly related to physical quantities. These parameters are found by model tuning to experimental measurements, rendering the model unfit for model based design. A stiction model based on known physical parameters has later been developed, cf. section 4.5 and paper [J].

Valve flow model

Valves suitable for efficient DD machines have large opening areas and tend to operate at low Reynolds numbers. Therefore, laminar flow characteristics may be expected for some part of the operation range, depending on the valve dimensioning.

A modified version of the classical orifice equation, $Q = C_d A\sqrt{2/\rho\,\Delta p}$, is used to model the valve flow. The discharge coefficient, C_d, is made a function of the Reynolds number is order to cover both the laminar and the turbulent flow regime. That is,

$$C_d(Re) = \begin{cases} C_{turb}\,\frac{\sqrt{Re}}{\sqrt{Re_t}} & , Re < Re_t \\ C_{turb} & , \text{else} \end{cases} \qquad \text{and} \qquad Re = \frac{d_h}{\nu}\,\overline{v} = \frac{d_h}{A\,\nu}\,Q \tag{2.7}$$

where C_{turb} is a constant discharge coefficient for the turbulent flow regime and Re_t determines the transition from laminar to turbulent flow description. For calculating the Reynolds number, $d_h = \frac{4A}{O}$ is the hydraulic diameter with O being the wetted perimeter, and ν the kinematic oil viscosity. Inserting (2.7) into (2.2) leads to a linear flow-pressure relation for laminar flows (Re below Re_t) and a cubic relation for larger Reynolds numbers. The parameters C_{turb} and Re_t may be roughly estimated, but generally need experimental measurements to be accurately determined.

In addition to the above flow model, a Computational Fluid Dynamics (CFD) analysis of the valve flow characteristics has been performed using the software package Ansys Fluent. More details on these valve flow models are given in paper [B].

2.3 Experimental results

The experimental results from the preliminary studies are summarized below, where the experimental results are compared to corresponding simulated responses using the above valve models.

Static actuator force characteristics

The static performance for three different plunger positions are given in figure 2.6, shown together with the corresponding FEA and analytic model forces.

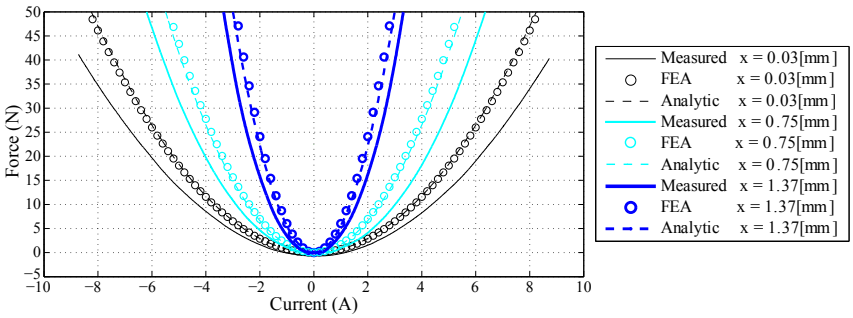

Figure 2.6: *Static actuator forces for different current levels for three fixed plunger positions (opening direction).*

Good correspondence between the FEM analysis and the analytic model is seen, however some deviation is present in comparison with the measured actuator forces (material saturation is not pronounced in the given current range). The models predict the change in actuator force for different positions and the parabolic characteristic well, but the measured force levels are lower than the models.

The lower measured actuator force is assumed to be caused by geometry deviations between the model and the physical prototype. Instead of being perfectly axisymmetric, the prototype has some holes for fixing screws in the actuator armature, spring holes and position measurement which is neglected in the models, cf. figure 1.19. These holes add to the magnetic circuit reluctance of the actuator. In addition, manufacturing tolerances are likely to contribute significantly to the force deviation, as air gap length changes of 0.1-0.2 mm in the primary air gaps give similar force deviations as those measured. The PWM voltage source may also contribute to the static force deviation by continuously generating Eddy-currents, but this effect is thought to be minor compared to the effect of the above geometric deviations.

To account for the increased reluctance found in the actuator prototype circuit, a correction term is added to the analytic reluctance model. Using this correction, the force deviation between the analytic model and the measurements are below 10 % in the operation range, and this corrected model is used as basis for comparing the dynamic measurements with the valve model in the following.

Dynamic valve response

The valve opening and closing response experiments are conducted using a fixed force reference throughout the valve stroke. That is, the current needed to obtain some constant force reference is continuously calculated and used for current reference. Deviations may therefore be present between the generated force and the force reference, but similar deviations should be present in the measurements and the simulations.

The valve closing response for different actuator forces are shown in figure 2.7. The dynamic behavior is largely captured by the developed model for different actuator

forces, and a minimum valve closing time of 3 ms is obtained. The oscillatory behavior seen at larger currents is a result of unwanted disturbance in the position measurement, giving an oscillating current reference. Only the simulated coil voltages are shown, as PWM voltages were used in the measurements.

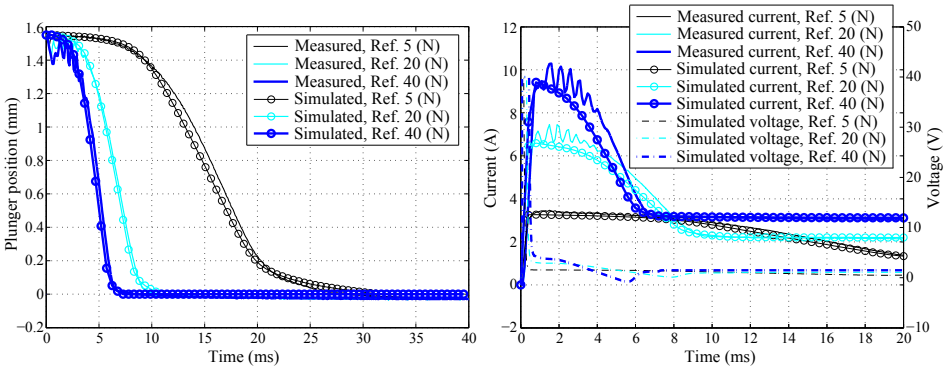

Figure 2.7: *Valve closing response for various actuator force references. Oil temperature* 20^oC *and atmospheric pressure.*

Opening valve responses are shown in figure 2.8, where an increased switching time of 4.5 ms is obtained due to larger stiction forces compared to valve closing, as expected from the larger contact area when opening. It is noted that active opening of the valve in DD operation is usually not performed, as pressure forces are utilized for passive opening of the valve, but the response in figure 2.8 serves to evaluate the valve model.

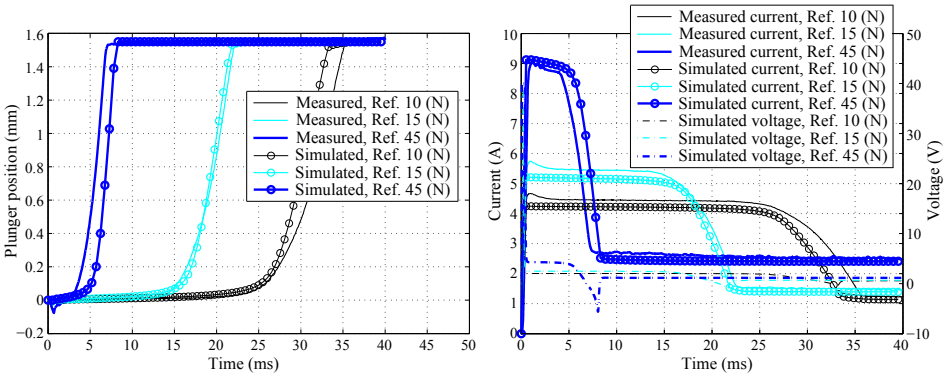

Figure 2.8: *Valve opening response for various actuation force references. Oil temperature* 20^oC *and atmospheric pressure.*

Valve flow characteristics

The valve flow characteristics are determined by measuring the pressures before and after the valve prototype at various flow rates, see paper [B]. Similar flow characteristics are found for flow in both directions, and only the result for flow intake to the chamber is presented here. Figure 2.9 (left) shows the measured pressure loss as a function of the valve flow rate. The CFD analysis predicts a pressure loss which is generally higher than the measurements, however, the overall characteristics are maintained. In addition, the orifice flow model shown in figure 2.9 (left) is seen to follow the main valve flow characteristics.

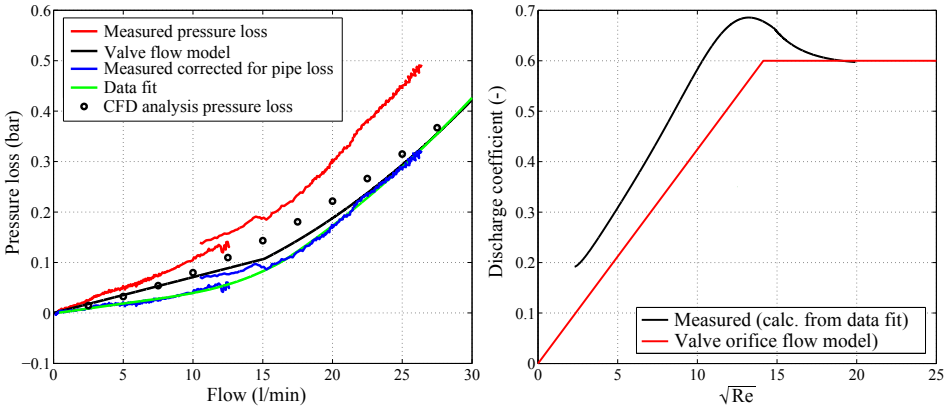

Figure 2.9: *Measured pressure loss compared to the CFD analysis and valve orifice flow model (left). The shown data fit used for calculation of the discharge coefficient shown right.*

Comparing the measured discharge coefficient to the model as a function of $\sqrt{Re}$ leads to the result shown in figure 2.9 (right). A distinct linear region is present, and the transition from pure laminar flow region is also seen. The peak in discharge coefficient is not included in the model, and some deviation is thus expected. The extension to include the laminar flow region in the orifice flow model is seen to correspond to measurements, even though experiments with larger flow rates are needed to confirm the model for higher Reynolds numbers. The measured relation between $\sqrt{Re}$ and C_d corresponds well with that shown in the classic book by Herbert E. Merritt [55].

Pumping operation

Experimental results of both full displacement and partial displacement of the DD pump using the prototype LPV have been obtained. These measurements are taken with the pump running 1500 rpm, an output pressure of approximately 200 bar and a low pressure very close to atmospheric pressure. A manually adjustable orifice is used to create an output load. Depending on the LP valve control, the intake oil is either displaced to the high pressure output through the passive HP valve, or returned to the low pressure

connection. A model of the pressure chamber and the passive HP check valve has been developed and combined with the LP valve models above, in order to compare the measured pumping response with the response predicted by models.

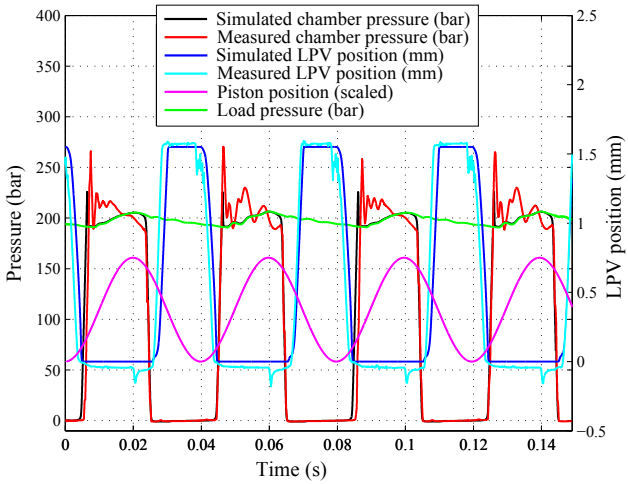

Figure 2.10: *Measured and simulated response for full displacement cycles.*

Figure 2.10 shows three (and a half) pumping cycles, where the LP valve is closed in each cycle to give full displacement. The piston movement is included in the figure, and high pressure oil is seen to be displaced as the piston moves from the bottom dead center towards the top. The modeled pressure chamber and valve movement response is shown together with the measurements, and reasonable correspondence is seen. Some coupling between the valve position measurement and valve actuator is present, leading to slight offsets and squirts when the coils are energized.

Referring to figure 2.10, the LP valve closing is initialized shortly before the piston reach bottom dead center and valve closure is obtained relatively close to bottom dead center. As the piston reaches the top dead center, the check valve allows some oil to reenter the chamber before closing, reducing the effective displacement of the prototype pump. An active LPV opening actuator force was necessary to obtain an acceptable pumping cycle, due to the very low pressure level, limiting the passive opening force during the cycle.

Part displacement is easily obtained by letting the pressure chamber idle (LP valve kept open during the entire piston cycle) during some of the piston cycles. Figure 2.11 shows the measured pumping response when modulating the cylinder chamber to obtain 15 % displacement. Instead of obtaining variable displacement by a modulation sequence as given in figure 2.11, part displacement is possible by closing the valve at some intermediate piston position, whereby only some portion of the piston stroke is used for effective displacement. This strategy has also been successfully tested on the prototype pump. A significant downside of this strategy is the increased loading on the

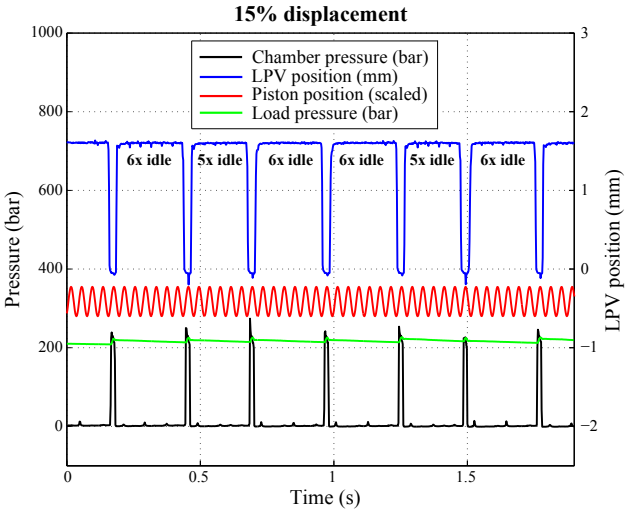

Figure 2.11: *Measured 15 % partial displacement using a modulation sequence of idle and pumping cycles.*

LP valve seat as the valve is closed at times with large flow rates and piston displacement. This was clearly evident from the increase in noise level and pitch during testing of this strategy compared to the modulated partial displacement.

The prototype pump unit used in the above measurements suffered from excessive leakage at the piston interfaces, which degraded the total efficiency to approximately 60 % at full displacement.

2.4 Discussion of preliminary studies

A small size DD pump prototype has been experimentally tested and modeled successfully. Considering the LP valve, which was developed specifically for the DD pump unit, the performance was largely as expected with no game stopping findings. The dominating characteristics were modeled with reasonable accuracy, albeit a number of non-physical parameters were needed.

At this point a number of challenges for further improving the performance of DD valves and scaling into larger units are apparent; on the model side, the models should all be based on known physical parameters to facilitate a model based design process. Furthermore, accurate models of additional aspects are needed to improve the valve design, in particular the dynamic pressure loads on the valve plunger and material stresses at the valve seating regions. On the design side, scalability of the valve to large displacement units should be investigated and the transient performance of the solenoid actuator should be considered. The prototype LP valve has a very large opening area

compared to the piston displacement, as evident from the largely laminar flow regime operation. This is beneficial for ensuring low flow losses, but space considerations may come into play for large displacement units. Some method for dimensioning DD valves is needed in this regard. The solenoid actuator in its basic non-laminated form proved to exhibit relatively slow force rising, especially when considered for fast rotating units of 1000 rpm and above. Clearly means of improving the transient performance exist (voltage boosting, lamination, circuit optimization), but other linear actuator types may offer improved performance.

Chapter 3

Supporting Studies for Large Scale Valves

In this chapter the focus is turned towards valves for large scale DD motors. A general method for determining the valve requirements is initially described, which applies to DD motors of any displacement and rotational speed.

Different possibilities for the valve seat geometry and actuator type are then discussed, and a suitable valve design topology for further work is selected. This leads to a reference design study, where a detailed CFD simulation is developed and compared to a corresponding lumped parameter model simulation. These studies suggest that the chosen design topology is suitable for efficient large scale DD motors, and this topology is therefore used as basis for the valve optimization in the next chapter.

3.1 General valve requirements for DD valves

When designing valves for efficient DD machines it is clear that the valves should exhibit low pressure losses and fast switching capabilities. At the same time it is apparent that both parameters in combination influences the efficiency; no matter how fast the valves switch, poor efficiency results if the valves exhibit high pressure losses and, conversely, slow valve switching also deteriorates the efficiency by increasing the percentage of flow conducted with semi-opened valves. One problem is therefore to quantify the general requirements for the valve switching time and the pressure loss to ensure efficient operation. When going to large scale DD machines such requirements are useful for initial valve dimensioning.

To obtain these requirements, a simplified generic model of a DD motor is utilized, where only the valve flow losses are considered. This may be used to set requirements for the DD valve in terms of switching time and pressure drop, for a given target efficiency. The target efficiency must be set conservatively high to account for other energy losses not

included in this simplified analysis. Additional information on the method described in this section may be found in paper [C].

The simplified model is illustrated in figure 3.1. Only a single pressure chamber is modeled, as the machine efficiency is independent on the number of pistons when neglecting energy losses other than flow losses.

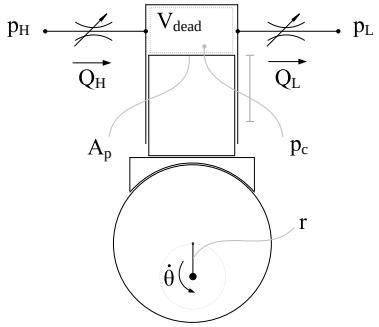

Figure 3.1: *Pressure chamber model. Shown in the top piston position ($\theta = 0$).*

The model consists of a reciprocating piston volume which is connected to a low pressure manifold and a high pressure manifold through two variable orifices, as illustrated in figure 3.1. The low pressure p_L, high pressure p_H and the rotation speed $\dot{\theta}$ are set constant.

For modeling the chamber pressure dynamics, the continuity equation is used:

$$\dot{p}_c = \frac{\beta}{V}\left(Q_H - Q_L - \dot{V}\right) \tag{3.1}$$

where p_c denotes the chamber pressure, Q_H and Q_L denotes valve flow of the high and low pressure valve respectively, β the effective bulk modulus of the oil and V the total chamber volume.

Including a dead volume V_{dead} and denoting the displacement volume $V_d = 2rA_p$, the cylinder volume is described by:

$$V(\theta) = \frac{V_d}{2}(1 - \cos\theta) + V_{dead} \tag{3.2}$$

$$\dot{V}(\theta, \dot{\theta}) = \frac{V_d}{2}\dot{\theta}\sin\theta \tag{3.3}$$

The volume function $V(\theta)$ shown in (3.2) is exact for the piston/eccentric assembly illustrated in figure 3.1. Other piston/eccentric topologies may differ from (3.2), but typically the dominating piston movement is sinusoidal and (3.2) is taken as a general approximation. DD machines typically exhibit relatively large dead volumes due to the large flow passages for the valves, and the dead volume is set equal to the displacement volume as a rough approximation, i.e. $V_{dead} = V_d$.

The orifice flow Q_L is described by:

$$Q_L = \frac{\overline{x}_L}{k_f}\sqrt{|p_c - p_L|}sign(p_c - p_L) \tag{3.4}$$

where $\overline{x}_L$ describes the normalized valve movement and k_f is the flow coefficient of the valve. A similar equation is used to describe Q_H, and equal flow coefficients are assumed for the HPV and the LPV.

Valve opening and closing is simplified to be only a function of the valve switching time t_s, and thereby independent of the specific valve geometry and mass. Doing so enables a general study of different sizes of machines without determining the specific design and dimension of each machine. Specifically, valve switching is assumed to be an ideal movement with constant acceleration and subsequent deceleration for half the stroke, leading to an acceleration/deceleration of $\ddot{\overline{x}} = 4/t_s^2$.

Even though each valve movement itself is independent of the pressure forces, the passive opening of the LPV and HPV is modeled by letting the valve opening movement initialize when a positive pressure difference is present in the opening direction, eg. for the HPV when $p_c > p_H$ and $\overline{x}_i = \dot{\overline{x}}_i = 0$. Valve closings are controlled using two parameters θ_{LPV} and θ_{HPV}, which specify the angles at which valve closings are initialized.

Recall that for motoring operation, the LPV is closed when approaching the piston top dead center (TDC) to allow for the pressure chamber to pressurize and the HPV to open in time for the piston to be driven back towards bottom dead center by high pressure. This situation, before TDC, is illustrated in figure 3.2. Knowing the revolution speed $\dot{\theta}$, valve switching time t_s, oil stiffness β, pressure levels p_L,p_H and chamber geometry V_d and V_{dead}, enables calculating θ_{LPV} such that the chamber pressure approximately equals the HP manifold level in time for the HP valve to be opened at the piston TDC. This calculation takes basis in the simplified pressure curve shown in solid black in figure 3.2, cf. paper [C] for details.

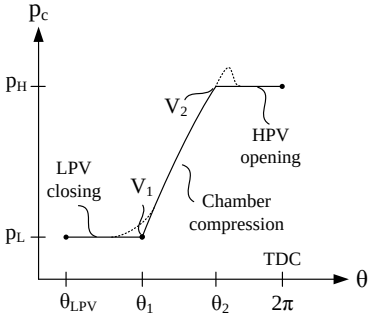

Figure 3.2: *Simplified pressure characteristics close to TDC used for calculating* θ_{LPV}.

Having determined the valve closing angles, the model consist of a number of parameters as shown in table 3.1. Setting the four variable input parameters to some example values

results in the motoring and idling response shown in figure 3.3. Pressure overshoot is seen at the piston top dead center (and undershoot for the bottom dead center), resulting from the valve dynamics.

Table 3.1: *Input parameters used in the simplified model.*

Variable parameters		Fixed parameters		Value
Displacement volume	V_d	High pressure	p_H	350 bar
Revolution speed	$\dot{\theta}$	Low pressure	p_L	5 bar
Flow coefficient	k_f	Oil stiffness	β	16000 bar
Valve switching time	t_s			

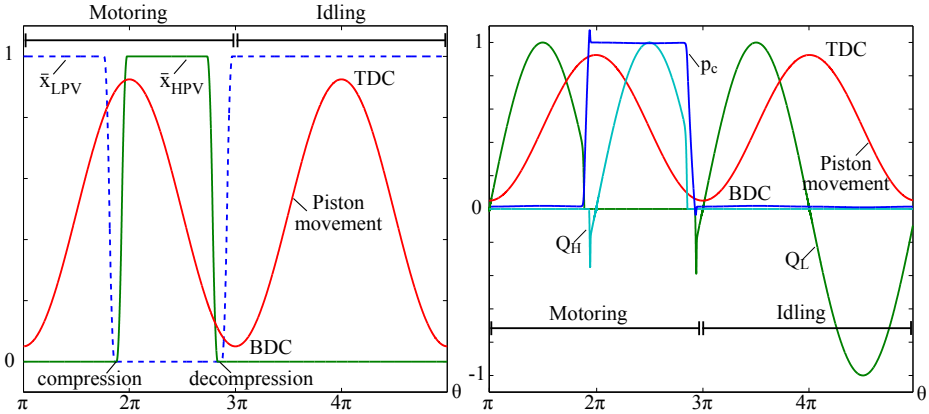

Figure 3.3: *Example response using the parameter set: $V_d = 100$ cc, $\dot{\theta} = 1500$ rpm, $k_f = 0.5 \cdot 10^5$ $\sqrt{Pa}{\cdot}s/m^3$ and $t_s = 1$ ms. The cycle time is 40 ms, and the maximum valve flow is 471 l/min.*

For a given set of machine parameters, (V_d,$\dot{\theta}$,k_f,t_s), the efficiency of the DD motor is evaluated with basis in the simulated energy losses during motoring and idling. Specifically, a part load efficiency is defined based on these losses[1]:

$$\eta = \frac{E_{out}}{E_{in}} = \frac{E_{in} - E_{loss}}{E_{in}} = 1 - \frac{E_{loss}}{E_{in}} \tag{3.5}$$

$$\eta_\alpha = 1 - \frac{\alpha E_{loss,motoring} + (1-\alpha) E_{loss,idling}}{\alpha E_{in,motoring} + (1-\alpha) E_{in,idling}} \tag{3.6}$$

where α is the displacement ratio in the range 0-1. The specific losses are evaluated for each specific set of machine parameters, using numerical integration on the simulation data, cf. paper [C] for detailed expressions.

[1]Sometimes, the machine efficiency is split in a volumetric efficiency and a hydromechanical efficiency; $\eta = \eta_v \, \eta_{hm} = \frac{Q_{out}}{\omega V_g} \frac{\Delta p V_g}{\tau} = \frac{Q_{out} \, \Delta p}{\tau \, \omega}$, where V_g is the geometrical displacement. Looking at η_v and η_{hm} separately for DD machines may then lead to confusing values, where η_{hm} evaluate to values above 1, due to some designs giving low values of η_v as a relatively large portion of the piston stroke is used for compression/decompression.

Conducting a machine simulating using the above model takes approximately 10 s, and a large number of simulations have been conducted to study the machine efficiency dependency on valve parameters k_f and t_s for a given machine size and speed, V_d and $\dot{\theta}$.

The resulting efficiency space does not need four independent parameters to be spanned, but may be described using two normalized parameters. These two parameters, termed the normalized switch time $\bar{t}_s$ and the normalized flow coefficient $\bar{k}_f$, is thus used to construct a general efficiency map of a DD motor based on the above model:

$$\bar{t}_s = \frac{t_s}{T_{rev}} \quad \text{with} \quad T_{rev} = \frac{2\pi}{\dot{\theta}} \tag{3.7}$$

$$\bar{k}_f = \frac{k_f}{\sqrt{p_H - p_L}/Q_{mean}} \quad \text{with} \quad Q_{mean} = \frac{V_d}{\pi/\dot{\theta}} \tag{3.8}$$

The resulting efficiency map $\eta(\bar{t}_s, \bar{k}_f)$ is given in figure 3.4 for 20 % displacement and full displacement. From the figure it is seen that even with very low flow coefficients, the efficiency still drops below 90 % if the normalized valve switching time exceed 14% of the revolution time, when only accounting for valve flow loss. Decreasing the normalized valve switching time to be within 10 % of the revolution time significantly improves the motor efficiency, and preferably a normalized switching time of 2-3 % should be obtained, where further decrease in switching time tend to have limited improvement in motor efficiency.

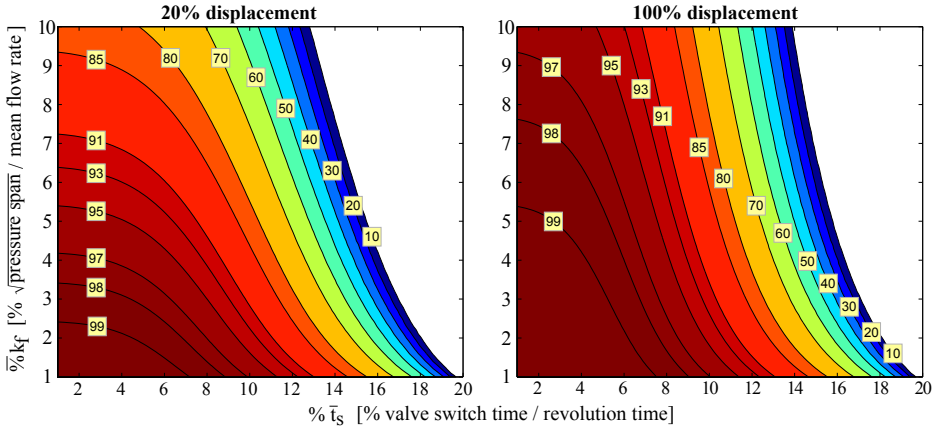

Figure 3.4: *Efficiency maps for part and full displacement of DD motors as function of the normalized valve switch time and the normalized valve flow coefficient.*

Using the above results, valve requirements may be estimated for a given machine displacement and rotation speed based on a target efficiency. This result is general and useful during the valve design process, as it gives the designer a good estimate of the maximum allowed switching time when knowing the specific valve flow properties, or alternatively gives the needed flow coefficient for a known switching time. A third application of the results is evaluation of the maximum displacement and rotation speed

for a given valve, for instance, a commercially available one. Paper [C] shows that a high-performance commercial valve is only suitable for relatively low rotation speeds, or small displacements for larger rotation speeds (max 700 rpm, though).

3.2 Valve topology selection

When faced with the task of selecting the design topology, the designer undertakes one of the most difficult engineering assignments, as the optimum choice seldom can be clearly identified even for relatively simple systems. For DD valves, when taking basis in directly actuated valves, two main topology selections are to be made: What flow/seat geometry is most appropriate and what actuator system is most suitable?

For the seat geometry one or multiple flow (metering) edges is possible. The complexity tends to increase with multiple flow edges, but more compact designs with large flow areas are possible with multiple flow edges.

For the actuator system, a number of different types of electro-magnetic linear actuators exist. Passive components may be included in the actuator system to add default positions.

Seat and plunger topology

Three possible seat and plunger topologies are shown in figure 3.5. For larger valve diameters, seat geometries with more than one flow edge are appealing, as large diameter edges may be realized without having to withstand the pressure force acting on the corresponding shadow area of the outer diameter. This makes it possible to reduce the moving mass, and at the same time obtain the benefit of an increased area gradient.

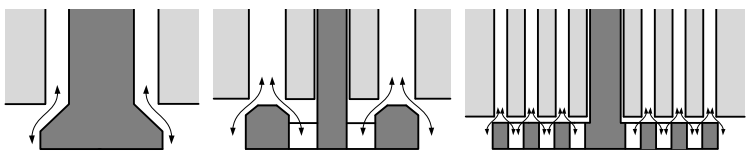

Figure 3.5: *Seat and plunger geometry concepts with single, double and multiple flow edges.*

The drawback of multiple flow edges is a more complicated stationary seating construction, as it has to provide multiple stiff seating edges. For the DD valve a seat topology with two flow edges is chosen for the initial design, being a compromise between a large area gradient and construction complexity. As such, an annular valve plunger is used, as shown in the middle of figure 3.5.

The plunger material should exhibit low density and high strength to minimize the moving mass. A material property chart with material density and strength has been constructed by M. Ashby [60], cf. figure 3.6. The strongest (highest failure strength)

materials are metals, ceramics and composites. Composite materials, in particular Carbon Fiber Reinforced Polymers (CFRP in figure 3.6), have high strength and low density compared to materials with similar strength.

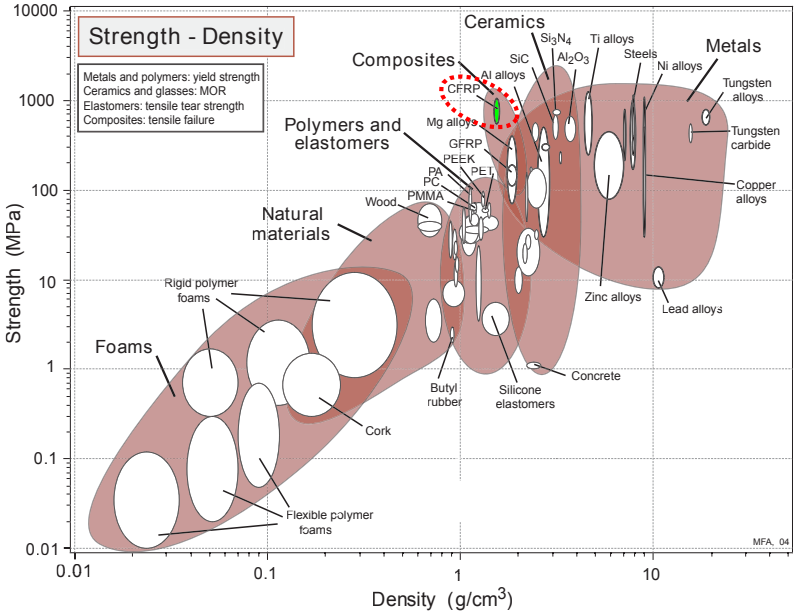

Figure 3.6: *Material property chart showing density and strength for a large range of materials [60].*

One version of CFRP uses Poly-Ether-Ether-Ketone (PEEK) as the polymeric filler (one of the strongest polymers available, also shown in figure 3.6), resulting in a high-performance composite material. In addition, this composite is reported to withstand $1.5{\cdot}10^9$ cycles[2] when tested as valve poppet under high pressure loading [61]. However, no details on the material condition after the durability test are given in [61]. The relatively low elasticity of 25 GPa allows the plunger to somewhat adapt to imperfections in the steel seat, via localized deformations.

Based on the above, carbon fiber reinforced PEEK is selected as plunger material in the following studies. In particular, a small fiber reinforced PEEK with 30 % carbon fiber ratio is chosen for its reasonable compromise between ductility and strength [62].

[2] 20 years of continuous full-displacement operation at 1500 rpm yield $15.8 \cdot 10^9$ cycles, but part displacement may reduce the number of cycles significantly.

Actuator topology

For both the LP and the HP valve actuator similar requirements are present. Basically, the actuator system needs to support two tasks:

- Apply closing force to facilitate fast valve closing at controllable times.
- Apply opening force to keep the valve open during piston displacement flows, where pressure and flow forces seek to close the valve. For the LPV, this is during flow from the chamber to the LP manifold at idling or motoring operation. For the HPV, this is during flow from the HP manifold to the chamber at motoring operation.

Figure 3.7 illustrates the timing and relative size of these actuator forces for idling, pumping and motoring operation. Motoring operation is the most complicated cycle, where opening force must be applied to keep the valves open during piston displacement in addition to valve closing forces.

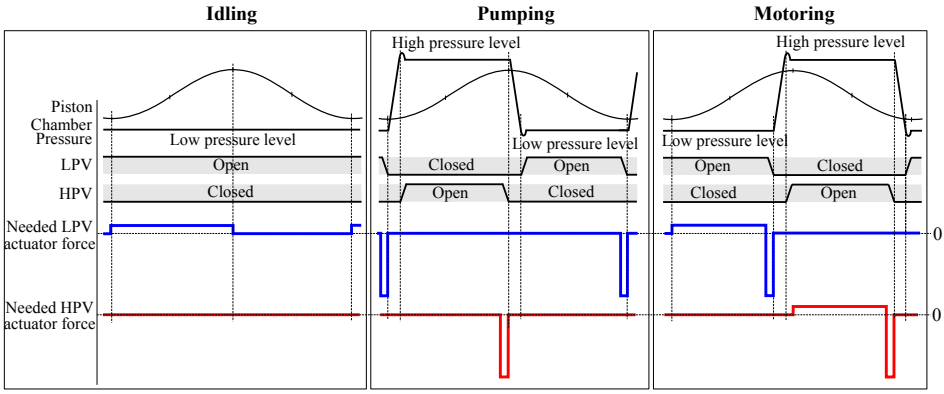

Figure 3.7: *Operation cycles of a DD machine with the corresponding needed actuator forces for the LPV and the HPV. Opening forces drawn positive, closing forces negative.*

As indicated in figure 3.7, relatively small opening forces are needed resulting from generous valve opening areas giving small pressure and flow forces. The closing forces are only needed for short periods of time in form of pulses with relatively high amplitude. Different combinations of active and passive (springs/permanent magnets) components in the actuator system are possible, but the most simple combination with respect to valve control seem to be a system with a passive component for applying opening forces, and an active component for applying the closing pulse. This way, the electromagnetic actuators are only energized for short periods of time and idling operation is performed without any actuator power loss. The actuators must counteract the spring force to close the valves. As previously mentioned, a drawback of this actuator combination is the risk

of being stuck in the unwanted state of 'high pressure idling' in case of a HPV actuator failure, where high pressure oil is displaced to and from the HP manifold repeatedly. This increases friction and leakage of the faulty cylinder compared to one defaulting to a low pressure idling state in the event of an HPV actuator failure.

An actuator system consisting of one or more preloaded springs to apply the opening forces, and an active electro-magnetic linear actuator for applying closing pulses are selected for further studies. The linear actuator must be able to quickly generate force pulses at precise times to enable high speed DD operation. Various types of linear actuators exist, and an investigation of three common linear actuator types is conducted in the following to get an idea of the response characteristics of these actuator types.

Transient performance of different linear actuator topologies

Having previously discovered a relatively slow transient force buildup of a solenoid actuator in the preliminary studies, particular attention has been paid to the transient behavior of the linear actuators. Three reference designs are used as basis for the comparison. These reference designs have been designed to generate a given static force level, while considering the moving mass and compactness of the actuator systems. Using transient electro-magnetic FEA, the transient performance of the three reference actuator designs have been compared. This analysis has been published in paper D, where further details may be found in addition to the following information.

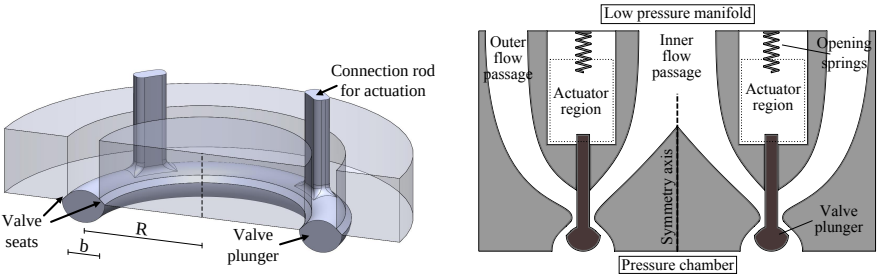

Figure 3.8: *Valve design basis used for developing three suitable reference actuator designs. Corresponding parameters are shown in table 3.2.*

Some representative valve design basis is needed to develop the actuator reference designs. This basis is illustrated in figure 3.8, for the LPV, with specifications given in table 3.2. A similar design is assumed for the HPV. This design basis is an initial guess for an effective valve for DD machines, dimensioned for a motor running at 1500 rpm with a displacement of 100 cc/rev for each cylinder. The valve pressure drop is predicted using CFD to be 0.37/0.43 bar for the maximum displacement flow rate of 471 l/min into and out of the pressure chamber respectively. This corresponds to a normalized flow coefficient $\overline{k}_f = 2.2$ %, following the above method for evaluating the efficiency. From figure 3.4, a normalized valve switching time $\overline{t}_s = 5$ % leads to an efficiency of approximately 99 % at 20 % displacement, when considering only valve flow losses. This

corresponds to a switching time of 2 ms, which is used as target switch time for the actuator reference designs in the following.

Table 3.2: *Specifications for the basis design shown in figure 3.8.*

Diameter (2R)	60 mm	Flow passage, b	8 mm
Stroke length	3 mm	Assumed moving mass (incl. armature)	75 g
Target switching time	2 ms	Target static act. force (open position)	250 N
Spring force	75 N	Plunger material	PEEK
Maximum supply voltage	50 V	Maximum supply current	50 A

The three reference designs are based on three actuator topologies, which differ in the way actuator force is generated. The reference actuator concepts are shown to the right in figure 3.9, for the valve in the open position. To close the valve, an upward actuator force must be applied to the armature. All three actuators generate a static closing force of approximately 250 N in the shown position when the selected maximum current is conducted.

The moving magnet topology, shown in the top of figure 3.9, utilizes two coils connected in series, which generate force in a push-pull configuration. The upper coil magnetic circuit attracts the moving magnet and the lower coil circuit repels the magnet. Linear actuators using a moving permanent magnet configuration is reported to be fast-acting [63, 64] and quick latching [65]. The specific configuration used is inspired from the work by Bruno Lequesne presented in [63].

The variable reluctance (middle figure 3.9) topology uses two separate coils (one for closing and another for opening force), and generates force because the magnetic circuit reluctance is lowered for the upper (coil) circuit when the plunger is moved upwards. This concept is widely used in fluid power on/off valves, and was also tested in the preliminary valve studies, cf. chapter 2.

The moving coil (bottom figure 3.9) utilizes a coil fixed to the moving plunger, and generates force based on the Lorentz force law. This type of linear actuator is also widely used, including applications requiring high frequency response [66, 67, 68, 69, 70]. Moving coil actuators are often referred to as voice coil actuators for its usability in speakers.

Each topology has been designed for minimum size, with a constraint for maximum steady flux density using an iterative manual process. All topologies may generate force in both directions, which may be needed during low temperature operation condition of the DD pump/motor as the flow pressure drop here increases, rendering the opening springs force insufficient to maintain the valve open.

In order to compare the performance of the actuator topologies, they are assumed to be driven by a power supply having a controllable voltage in the range ± 50 V and a maximum current of 50 A. In the transient response analysis of the topologies, maximum voltage is applied until the coil current reaches the maximum level, where after a constant current is conducted using the needed voltage to maintain the current.

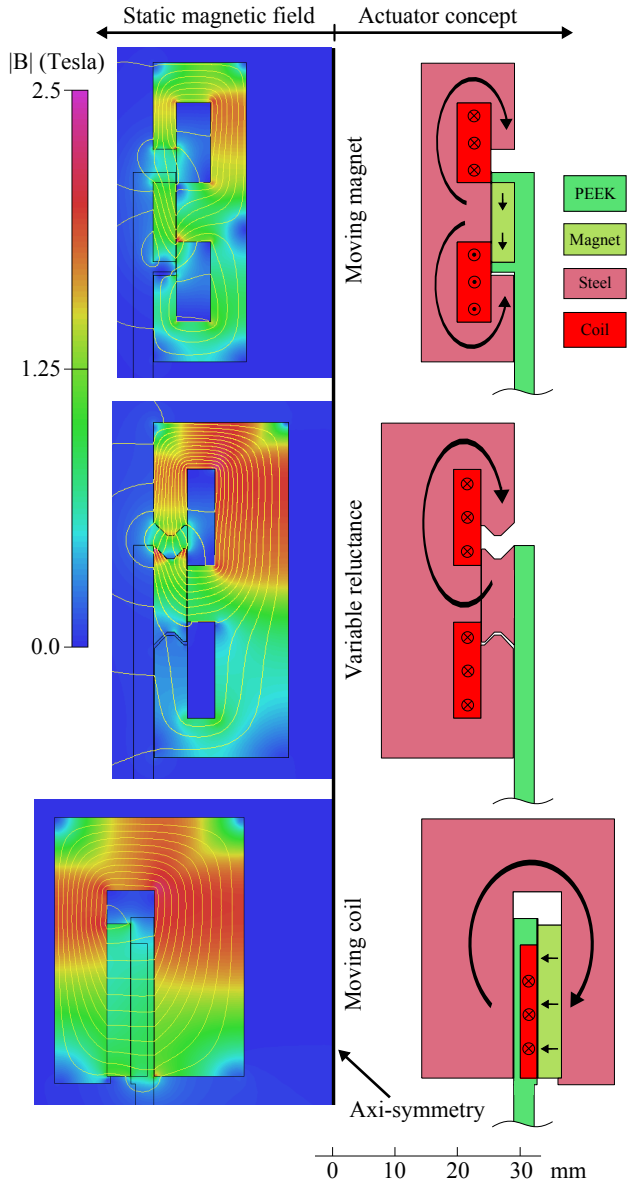

Figure 3.9: *Reference designs for a DD valve actuator (right), and the corresponding steady state flux density fields (left). The generated steady state actuator force is in the range* $258 - 266$ *N for a coil current density* 40 A/mm^2. *Number of windings N is 2x48, 47(only upper coil used for closing) and 40 for the topologies listed from the top, and the corresponding coil resistances R are 2x0.13, 0.12 and 0.15* Ω. *The wire diameter for all topologies is* 1 *mm and a* 0.67 *fill factor is assumed.*

Solving the transient response of the three reference actuator designs using transient electro-magnetic FEA using the software package Cobham Opera-2d, results in the voltage, current and force response shown in figure 3.10. Further description of the FEA may be seen in paper [D].

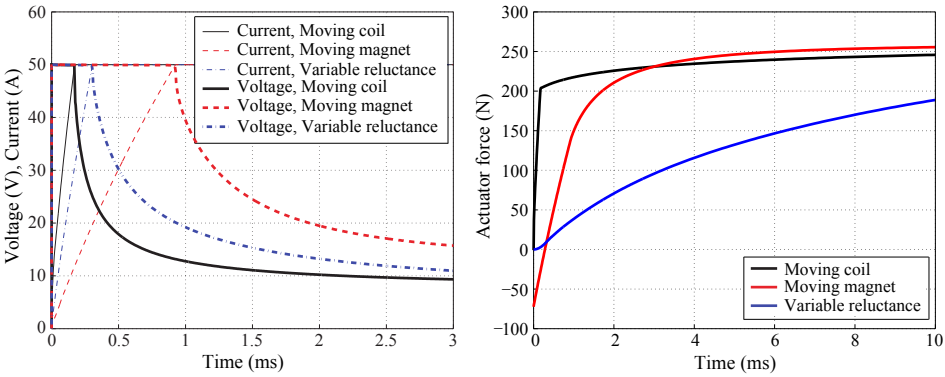

Figure 3.10: *Left, the voltage and current response of the three actuator reference topologies. Right, corresponding transient actuator force buildup.*

Referring to figure 3.10, large differences in the force build-up time are seen, as the moving coil topology reaches 200 N in 0.17 ms, followed by the moving magnet topology in 1.7 ms and lastly the variable reluctance topology in 11.6 ms. This superior transient force characteristics of the moving coil concept shows that as this actuator concept is not slowed down by Eddy current effects as the moving magnet and variable reluctance concepts are.

The moving coil concept takes advantage of the presence of a stationary magnetic field generated by the permanent magnet. This actuator is thus not dependent on a magnetic field to be developed as response to energizing the coil, but generates force as soon as current is conducted in the armature coil. In addition, Eddy currents seeking to reduce the change in flux effectively limits the transient self-inductance seen by the coil. This decreases the current rise time and thereby also the force rise time. That is, the Eddy currents improves the transient response of the moving coil actuator, contrary to the two other actuator concepts. It is noted that the coil bobbin must be electrically non-conducting for the above to apply.

The main disadvantage of the moving coil actuator for DD valves is the need for some flexible wire solution to connect the moving coil, which may be a challenge when considering durability. The moving coil linear actuator is very different from the variable reluctance (solenoid) actuators used in current state of the art DD valves, but the moving coil actuator seems very suitable for the DD valve application. In particular, it is excellent in supplying short force pulses with large amplitudes, as seen needed in figure 3.7. This leads to precise timing of the valves and high initial accelerations, resulting

in low switching times. In addition, when compared with the variable reluctance concept (solenoid), the moving coil actuator is bi-directional enabling the possibility to aid the passive opening spring in low temperature operation conditions and minimizing the valve impact energy (and noise) by applying braking force before impact.

A number of parameters could be further investigated and optimized for the reference designs above. However, the comparison serves as a basis for comparing the actuator topologies, and based on the above, the moving coil concept is considered as actuator topology in the following studies despite the construction challenges.

3.3 Motor reference geometry

The remainder of this chapter concerns modeling of large scale DD motor pressure chambers using the selected valve topology. Focus is on detailed modeling of the valve dynamics and pressure dynamics, to obtain knowledge of the characteristics of large scale motors and corresponding modeling methods. For simplicity, the actuator model is simplified to an ideal force with a given ramp time in these studies.

In order to facilitate such detailed analysis, a reference motor design is needed. Therefore, a large scale motor design have been developed with inspiration from current large scale DD units. This reference motor is designed to be suitable for driving a generator in a wind turbine, as part of a wind turbine transmission. This motor design is briefly introduced in this section and used as basis in the following sections, where a CFD model is developed and compared to a lumped parameter model. Specifications of the designed motor are given in Tab. 3.3.

Table 3.3: *Specification of a reference motor used as basis for detailed analysis.*

Rotation speed	1500 rpm	Cylinders	64
Displacement total/cyl.	9024/141 cc	Cyl. dead volume	274 cc
Manifold pres. high/low	350/5 bar	Power total	7.3 MW
Valve diameter/stroke	60/3 mm	Cyl. bore/stroke	60/50 mm
Overall size	Ø1.2x1.5 m	Valve moving mass	70 g

The reference motor topology is shown in figure 3.11, where the high pressure manifold input, low pressure manifold output and shaft is shown. In principle, changing the rated motor power may simply be done by changing the number of slices, while considering the strength of the shaft. A minimum of energy loss is associated with fluid flow to and from the LPVs as a result of the surrounding low pressure manifold.

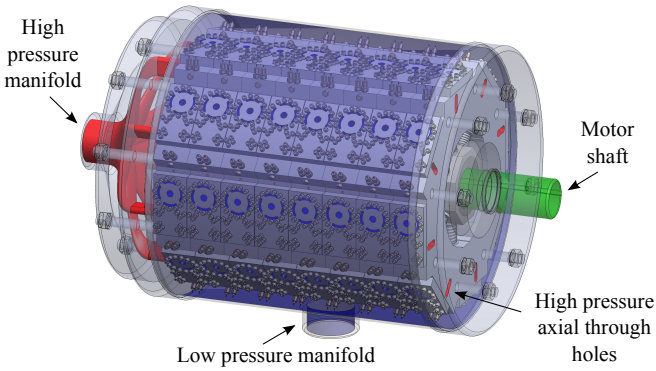

Figure 3.11: *Digital hydraulic motor with 64 pressure chambers. Eight slices having eight pressure chambers each are stacked axially and the pistons act on a common shaft. The low pressure manifold surrounds the stacked slices, and the high pressure working oil is distributed by the high pressure manifold through axial holes in the slices.*

Figure 3.12 shows a section view of one of the slices in figure 3.11. Eight pressure chambers are arranged radially, each connected to a reciprocating piston and two annular seat valves (LP and HP). Low pressure loss for the LPV is prioritized above the HPV pressure loss to improve part load efficiency, and the LPV is thus positioned directly above the piston. The moving coil actuators act directly on the annular seat valves, and are assumed capable of applying a net closing force of 300 N on the valve plungers (including spring counter-acting), with a ramp time of 1 ms.

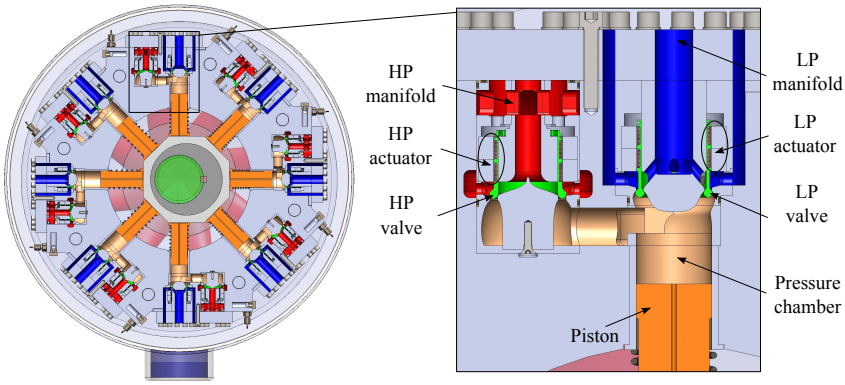

Figure 3.12: *Section view of the motor slice, illustrating the radial piston setup with eight pressure chambers. Each pressure chamber is connected to the LP manifold and the HP manifold with annular seat valves.*

Opening springs are included in the valve design as seen in figure 3.13. Each valve assembly is made to fit a cartridge, which may then be easily replaced in case of a valve failure.

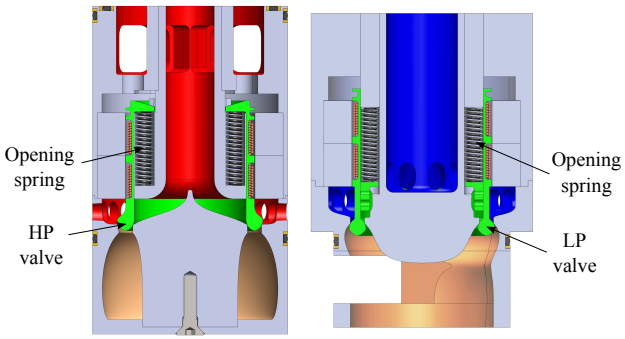

Figure 3.13: *High pressure (left) and low pressure (right) valve cartridge assemblies, both shown in a section view revealing two of the four opening springs. The springs are dimensioned to keep the valve in the open position (both valves shown closed) during piston displacement flows.*

The pressure chamber together with the LP - and HP manifold shown in figure 3.12 (right) is the fluid domain forming the basis for the detailed analysis in the following sections. Only a single chamber is considered, whereby the pressure loss of the complete manifold is disregarded.

3.4 Transient CFD model of DD motor

The most detailed analysis of a fluid domain is based on the Computational Fluid Dynamics (CFD) method. This method uses discretization and numerical methods to solve the governing Navier-Stokes equations for a given fluid domain. Current CFD software packages are able to simulate transient flow problems with dynamically changing boundaries in three dimensions. Thereby, a complete fluid analysis of a DD motor pressure chamber is possible including piston and valve movement. Such analysis is, however, complicated by the valve movement being coupled to the fluid forces, and that the movement cannot be accurately predetermined. In addition, the completely closing nature of seat valves imposes a simulation challenge, as the fluid mesh cannot easily collapse totally.

Closure of the valves is therefore simulated by not allowing fluid to flow through the valve orifice when the opening is below 0.1 mm, and the valves are stopped at this distance

from the seat. Valve stiction effects is thus not present in the fluid field solution, and must then be included by other means in the valve movement description. This is most important for the high pressure seat valve, as this valve is surrounded by high pressures during valve opening. A later attempt to include the stiction effect into the transient CFD model was not successful, as doing so forced the solver to take very small time steps, resulting in several weeks of simulation time for a single motoring operation cycle. The overall response of the motor is, however, still considered valid as the stiction effects have minor influence on the overall motor operation. The CFD model is later used as basis for developing a lumped parameter model where stiction effects may be implemented.

This section presents a transient CFD simulation of the pressure chamber based on the reference motor design. The CFD model is developed both to get knowledge of the details of the fluid flow and resulting valve fluid forces, but also to gain knowledge of how computationally heavy such models are and to gain insight into the level of effort needed for developing such CFD model. Further details may be found in paper [E].

Computational Fluid Dynamics Model and mesh

For simulation of the fluid domain, the fluid volume is divided into a finite number of volumes and each volume is solved using Navier-Stokes equations (continuity and momentum) in discretized form. The flow is dominated by viscous forces, indicated by Reynolds number being in the range 0-1500 at the valve orifices. However, transition from laminar into the turbulent flow regime may appear at orifices with Reynolds number being only a few hundreds, as also seen in the preliminary studies, cf. section 2.3. To account for the turbulent flow effects, Reynolds-Averaged Navier-Stokes (RANS) equations with a turbulent-viscosity model are used as fluid dynamics model, specifically using the $k\epsilon$-model to simulate turbulent flow effects. The CFD software package FLUENT 14.0 has been used for solving the fluid domain problem. Details of the specific governing equations and solver settings may be seen in paper [E].

DD motors typically operate at low pressure in the LP manifold, and very low pressures close to the cavitating level may therefore occur. At such low pressures, effects of entrained air are present, which lead to reduced effective density and oil stiffness. A pressure dependent density and stiffness is used to model this effect, as discussed and experimentally validated in [71]:

$$\rho(p) = \frac{\rho_{F0}\,(1-\alpha) + \rho_{A0}\,\alpha}{(1-\alpha)\left(1+\frac{m\,(p-p_0)}{\beta_0}\right)^{-\frac{1}{m}} + \alpha\left(\frac{p_0}{p}\right)^{\frac{1}{\kappa}}} \tag{3.9}$$

$$\beta(p) = \frac{(1-\alpha)\left(1+\frac{m\,(p-p_0)}{\beta_0}\right)^{-\frac{1}{m}} + \alpha\left(\frac{p_0}{p}\right)^{\frac{1}{\kappa}}}{\frac{1-\alpha}{\beta_0}\left(1+\frac{m\,(p-p_0)}{\beta_0}\right)^{-\frac{m+1}{m}} + \frac{\alpha}{\kappa\,p_0}\left(\frac{p_0}{p}\right)^{\frac{\kappa+1}{\kappa}}} \tag{3.10}$$

where $\rho_{F0} = 870$ kg/m^3 and $\rho_{A0} = 1.14$ kg/m^3 is the density at atmospheric pressure of pure oil and air respectively, $\alpha = 0.5\%$ is the assumed air ratio at atmospheric pressure, β_0 the reference stiffness, $m = 11.4$ the stiffness pressure gradient and $\kappa = 1.4$ the adiabatic constant of air. This value of air to fluid ratio, α, was used during the experimental

verification in the preliminary study, where reasonable simulation correspondence was found.

A pressure dependent dynamic fluid viscosity is also applied [29]:

$$\mu(p) = \mu_0 \, e^{B\,p} \quad \text{with} \quad B = 0.0026 - 10^5 \lambda \tag{3.11}$$

where $\mu_0 = 0.04002$ Ns/m^2 and $\lambda = 40°C$.

The piston and valve movements are dynamically solved during the motor cycle simulation, by continuously calculating the velocities and updating the positions according to the time step taken by the solver. Specifically, the valve velocities $\dot{x}_{lpv}$, $\dot{x}_{hpv}$ and piston velocity $\dot{x}_p$ used for updating the mesh to next time step is calculated as:

$$\text{Valves:} \quad \dot{x}(k) = \frac{F_{res}(k-1)}{m}\Delta t + \dot{x}(k-1) \tag{3.12}$$

$$\text{Piston:} \quad \dot{x}_p(k) = \frac{l_{\text{stroke}}}{2}\dot{\theta}\sin(\theta(k)) \tag{3.13}$$

where k denotes the current time step, F_{res} the resulting force (sum of fluid pressure, shear forces and actuator force) in the movement direction, m the moving mass, Δt the step size, l_{stroke} the piston stroke and θ the shaft angle. Fluid forces acting on the valve plunger boundary are determined by numerical integration over the corresponding mesh surfaces. The supporting functions of the core CFD solver is custom coded using user defined functions (UDF, c-language) and scheme files.

An adaptive time step solver is used. As such, each step size is adjusted according to the present level of gradients in the fluid. Upper limits for the step size are set based on valve velocities and positions, such that small step sizes, and thereby small mesh changes, are ensured when either of the valves are close to their end positions.

The FLUENT solver is able to utilize unstructured non-conformal meshes and includes dynamic mesh algorithms suitable for deforming meshes as found in the pressure chamber due to piston and valve movement. The fluid domain mesh of the motor reference design is illustrated in figure 3.14, where only half the fluid volume is meshed due to the symmetric geometry of the pressure chamber and manifolds. A constant pressure boundary condition is applied to both the low pressure manifold faces and the high pressure manifold face. A common challenge when developing a CFD mesh is the compromise between solution accuracy and computational cost, determined by the mesh quality and the number of cells. In [72], acceptable correspondence between a CFD simulation and experimental measurements were obtained on an external gear pump, investigated experimentally using particle tracking methods. The mesh densities shown in [72] have therefore been used as basis for selecting a sufficient number of mesh cells. Reasonable accuracy of the described CFD model is therefore expected, although subject for further experimental validation.

The resulting mesh consist of approximately 350k cells depending on the piston and valve positions. To ensure proper mesh refinement together with a mesh topology able to change throughout the CFD simulation, the fluid domain is separated into 26 regions which are meshed individually and combined using interfaces to join the mesh zones.

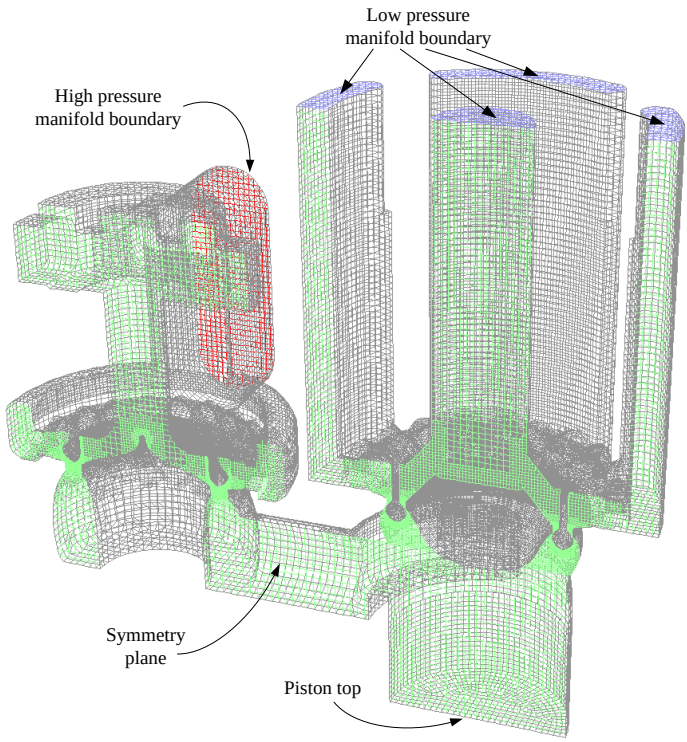

Figure 3.14: *Fluid domain mesh consisting of approximately 350k cells. Constant pressure boundary conditions are set on the high and the low pressure manifold faces. Piston and valve plunger faces are moved during simulation and the mesh is updated using layering zones.*

Figure 3.15 shows the mesh topology, having three types of mesh parts: Stationary zones (dark blue), moving zones (purple) and layering zones (green). While the stationary and moving zones have a constant number of cells with fixed sized, the layering zones changes when stretched or compressed. New cell-layers are added when the size is increased and vice versa when decreased [73].

Layering zones are well suited for the linear motion connected with valve and piston movement, however it requires parallel layers in the mesh zones near the moving faces with well-defined cell lines parallel with the moving face, as seen in figure 3.15 below the LPV. In most cases this entail the use of time consuming structural mesh zone development. During development of the mesh topology different dynamic mesh algorithms other than layering were considered, relaxing the mesh development requirements. However, local re-meshing algorithms failed to be effective due to large deformation ratios and the need for multiple expansions and compressions for the same mesh region. The non-axisymmetric parts of the mesh have been generated in ANSYS Meshing using a

Cut-Cell Meshing method with local refinement [74], whereas the axisymmetric parts have been generated using the ICEM CFD meshing package.

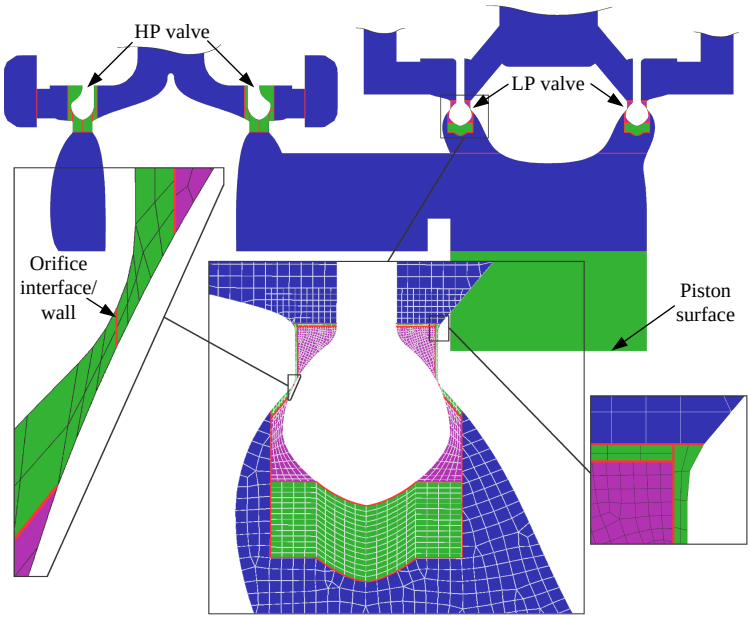

Figure 3.15: *Mesh topology with detailed view at the LPV. Green regions indicate layering zones, dark blue is stationary zones and purple are moving (but non-deforming) zones.*

The problem of simulating the seat valve closure is solved by changing the orifice interface to a wall, with zero fluid flow across, and changing the wall back to an interface as the valve plunger leaves the seat, cf. figure 3.15. This wall/interface change is performed at 0.1 mm.

Simulation results

Figure 3.16 (left) shows an example of the magnitude of the velocity field at the symmetry plane for motoring intake flow. The velocity field is shown for the piston in middle position, with $\theta = 90°$C, where the intake flow is greatest. As expected the LPV is closed and the HPV is fully open with flow into the pressure chamber. Figure 3.16 right shows the pressure field corresponding to the velocity field. A pressure drop of approximately 5 bar is present from high pressure manifold inlet to the top face of the piston, which is mainly introduced in the orifice region. A similar example during motoring discharge flow to the LP manifold may be seen in paper [E].

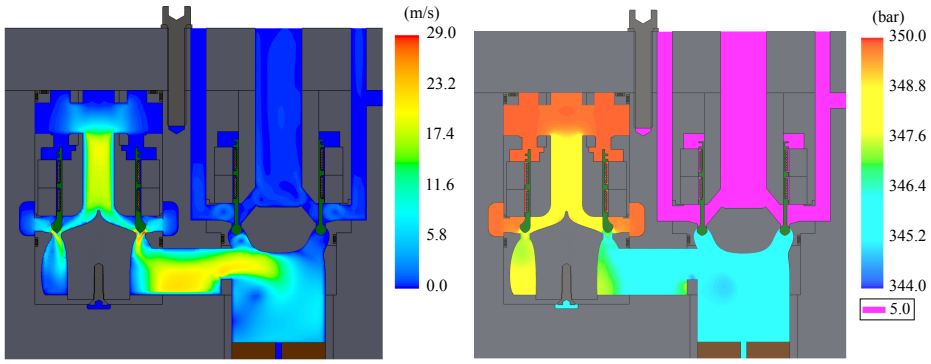

Figure 3.16: *left, magnitude of the velocity field taken at $\theta = 90°$ during motoring action. Flow is from the HP manifold through the HPV and into the pressure chamber. Right, corresponding pressure field.*

The dynamic response for an idling cycle followed by a motoring cycle is given in figure 3.17, where the chamber pressure is represented by the average pressure in the chamber fluid volume. A proper initial condition for the analysis is obtained by simulating a complete revolution with the LPV open before activating the valve control. In the motoring cycle, the LPV closing and the HPV closing is set as close to piston top and bottom position as possible respectively, while still having sufficient piston stroke left to pressurize/depressurize the chamber and subsequently open the HPV and LPV. When near optimum valve operation is achieved, only small amounts of valve back-flow happen during motoring operation, as seen in figure 3.17. Valve closing signal angles for the simulated system are -42 and 133 degrees for the LPV and HPV respectively, with 0 degrees being the piston top position.

The lower parts of figure 3.17 show the forces acting on the valve plungers. Actuator forces are seen to be small compared to the maximum fluid forces, which act to close the valves. The largest simulated fluid opening force is present at the time when opening and the valve reaches the end stop, as shown in figure 3.17. These force peaks arise as a result of a hard velocity reset during simulation, and would be limited in a physical setup due to flexibility of the plunger material and increased damping near the end surfaces.

Some key figures of the DD simulation are given in Tab. 3.4. A simulated overshoot in average chamber pressure of 6 bar compared to the HP manifold is obtained, resulting from a fast acting HPV with opening spring force, near optimum valve actuator timing and no stiction effects. Due to the decompression and compression period, where both valves are in the closed positions, the pressure chamber is only connected to the HP manifold for some fraction of the piston stroke. A relatively low utilization of the piston displacement is thus obtained (93%), which is a general characteristic of DD motors.

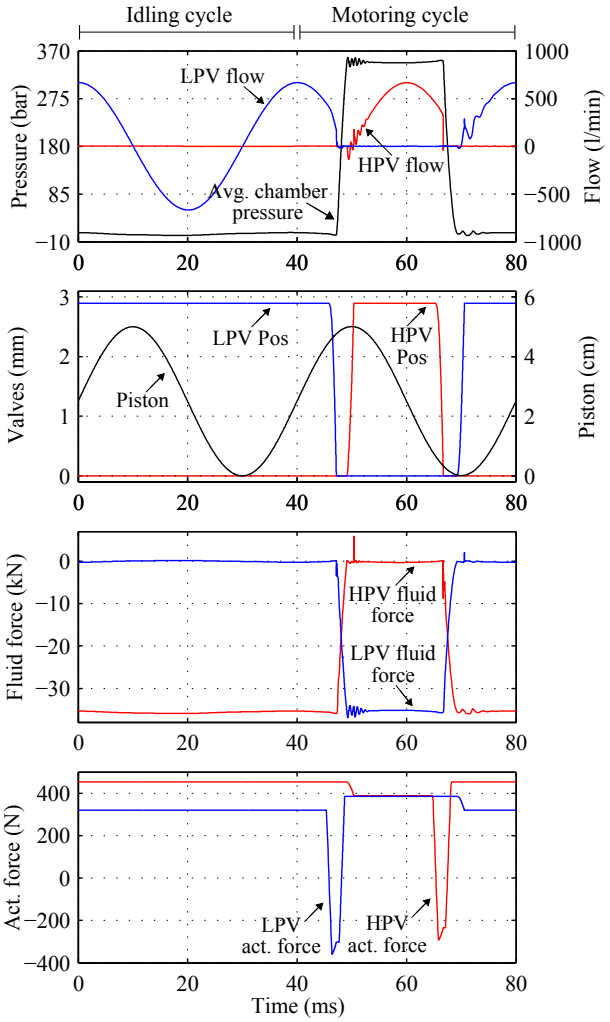

Figure 3.17: *Simulated dynamic response of DD motor for idling and motoring operation. The LPV is kept open during the idling cycle, and closed when the piston approaches top position, resulting in pressurization of the pressure chamber, which in turn forces the HPV to open when close to piston top position. The motoring stroke is ended by closing the HPV, leading to depressurization of the chamber, in turn forcing the LPV open.*

Table 3.4: *Reference DD motor simulation results*

Cycle time	40 ms
Min/max avg. chamber pressure (idling)	2.4/8.1 bar
Min/max avg. chamber pressure (motoring)	2.6/356 bar
Actuator force (net closing)	300 N
Opening time HPV/LPV	1.3/1.4 ms
Closing time HPV/LPV	1.5/1.4 ms
Impact velocity HPV/LPV (closing)	4.4/4.6 m/s
Max closing fluid force HPV/LPV	36/37 kN
Max closing fluid force intake/discharge (LPV/HPV)	258/254 N
Max opening fluid force HPV/LPV (not impact)	0.3/0.2 kN
Max opening fluid force HPV/LPV (impact)	5.8/1.9 kN
Utilized displacement	93%
Simulation time (idling+motoring cycle):	
3.4 Ghz, 12 GB ram, single core config.	37 hours

The efficiency of the motor predicted by the transient CFD analysis is evaluated by use of the simulated manifold flows, orifice flows, boundary movements and average pressure in the chamber and at the piston surface. Integrating over the motoring cycle and the idling cycle enables calculation of the simulated efficiency. The calculation details may be seen in paper [E]. Efficiencies of 98.3/93.9 % is found for the transient CFD simulation at 100/20 % displacement respectively. Comparing these efficiencies with those obtained using the method for setting the valve requirements (section 3.1) leads to approximately the same efficiencies. Specifically, this method predicts efficiencies of 98/92 % for the switching times simulated, and flow coefficients evaluated using steady CFD analysis[3].

For 'smooth' operation, the above transient CFD model is solved within a reasonable time frame (1-2 days). Such 'smooth' operation is obtained when the valves are closed near piston top dead center and bottom dead center, where the flow rates are relatively small, and when the valve plungers are not quickly forced open by large pressure differentials, i.e. when significant stiction is not present. When these 'non-smooth' operations appear during the simulation, the solver is still able to converge to the solution, but the resulting time steps taken by the adaptive solver is very small, and the simulation effectively stops (several weeks of simulation needed to get past the 'non-smooth' stage). Increasing the residual tolerance within reasonable levels did not improve the simulation speed significantly.

Mesh refinements and smoother mesh density transitions may improve the simulation speed at these 'non-smooth' stages, and a refined fluid mesh of approximately 2M cells (original mesh 350k) was developed and attempted. Unfortunately, the general simulation speed with this refined mesh was found too slow to be feasible for motor cycle analysis.

[3] Flow coefficients k_f for the LPV and HPV may be found using steady CFD taking the pressure drop from the manifold input to the piston surface for the rated flow. For the reference motor design this gives $\overline{k}_{f,lpv} = 5.9\%$ and $\overline{k}_{f,hpv} = 7.8\%$. Using the average value as equivalent gives $\overline{k}_{f,avg} = 6.8\%$. The switching times shown in table 3.4 gives approximately $\bar{t}_s = 3.5$ %. Figure 3.4 then gives the predicted efficiencies of 98/92 %.

In total, as expected and given the characteristics of the developed transient CFD model, this type of simulation is not very useful at the design stage. The main drawbacks are the computation expense of simulating the motor operations, and the large effort needed in developing a compatible dynamic mesh. The model gave, however, insight into the characteristics of large scale DD units and was used to develop a simplified model which may be used more efficiently in the design phase. This lumped parameter model is described in the following section.

3.5 Lumped parameter model of DD motor

This simulation model seeks to combine the accuracy of CFD analysis with the rapid simulation speed of a Lumped Parameter Model (LPM). The main idea is to use steady CFD analysis to evaluate the flow characteristics of a given motor design, taking the complicated flow geometry of the manifolds, valves and chamber into consideration. The found flow parameters are then incorporated into a LPM with rapid simulation speed compared to a transient CFD analysis. The LPM method is shown applied to the above reference motor design (section 3.3) and the dynamic response is compared to the transient CFD solution. The LPM method is presented in paper [F].

The basis of the LPM is illustrated in figure 3.18. Here x_p, x_h, x_l are the piston and valve positions (h denotes hpv and l denotes lpv), A_p the piston area, V the chamber volume, p_c the chamber pressure, β the effective oil bulk modulus, p_h, p_l the high and low pressure manifold pressures, Q_h, Q_l valve volumetric flow rates, A_h, A_l variable valve orifice areas, m_h,m_l valve moving mass, $F_{fluid,h}$,$F_{fluid,l}$ fluid forces acting on the valves, $F_{act,h}$,$F_{act,l}$ valve actuator forces and $F_{fric,h}$, $F_{fric,l}$ friction forces opposing valve movement.

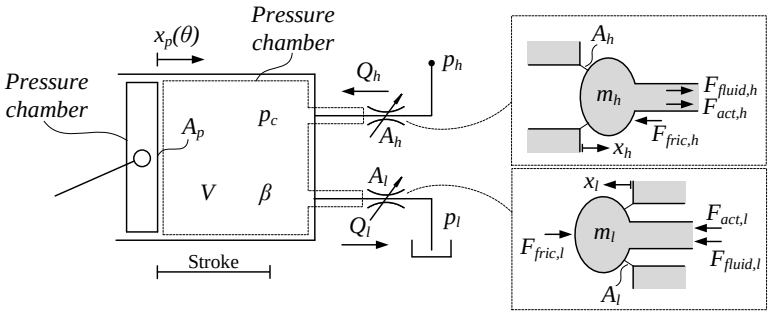

Figure 3.18: *Lumped Parameter Model (LPM) of the digital hydraulic motor.*

The motor operation is simulated by letting the piston movement x_p follow a movement corresponding to a rotating shaft and manipulating the valve actuator forces $F_{act,h}$ and $F_{act,l}$ depending on the operation mode. In order to obtain continuity, the chamber

pressure p_c is determined using:

$$Q_h - Q_l = -A_p\dot{x}_p - A_{pl}\dot{x}_l + A_{ph}\dot{x}_h + \frac{V}{\beta}\dot{p}_c \tag{3.14}$$

where A_{ph} and A_{pl} are the shadow areas of the HPV and LPV affecting the control volume. The total chamber volume is given as: $V = V_{dead}+A_p(l_{stroke}-x_p)+A_{ph}x_h-A_{pl}x_l$, with l_{stroke} being the stroke length and V_{dead} the chamber dead volume. The effective bulk modulus is modeled as pressure dependent by including the effect of entrained air [71], as previously shown in (3.10) on page 57.

In general, the valve flow rate may be laminar (linear relation between pressure drop and flow rate), turbulent (quadratic relation) or some combination depending on the characteristic Reynolds number of the oil flow. Orifice areas are generally large compared to the flow rate in digital hydraulic motors, giving relatively low Reynolds numbers, and a flow-pressure relation taking both the laminar and the turbulent region into account is therefore suitable. A flow-pressure relation having the form $\Delta p = k_1Q^2 + k_2Q$ is thus used, see [75] for further discussion. Assuming positive coefficients k_1 and k_2, this leads to a single positive solution for each valve flow:

$$Q_h = A'_h\text{sign}(p_h - p_c)\frac{\sqrt{k_{2h}^2 + 4k_{1h}|p_h - p_c|} - k_{2h}}{2k_{1h}} \tag{3.15}$$

$$Q_l = A'_l\text{sign}(p_c - p_l)\frac{\sqrt{k_{2l}^2 + 4k_{1l}|p_c - p_l|} - k_{2l}}{2k_{1l}} \tag{3.16}$$

where A'_h,A'_l are the normalized orifice areas. In equation (3.16), different sets of coefficients (k_1,k_2) may be used for positive and negative flow direction, depending on the specific flow geometry.

The valve dynamics are determined by:

$$F_{fluid,h} + F_{act,h} = m_h\ddot{x}_h \ , \quad F_{fluid,h} = \gamma_h(Q_h, x_h)A_{ph}(p_c - p_h) - B_h\dot{x}_h^2\text{sign}(x_h) \tag{3.17}$$

where $F_{fluid,h}$ is the total fluid force acting on the valve plunger (pressure and flow forces), $F_{act,h}$ the actuator force, $\ddot{x}_h$ the plunger acceleration, $\gamma_h(Q_h, x_h)$ a force-pressure correction function and B_h a drag coefficient. A similar expression is used for the LPV. Viscous friction and virtual mass terms does not dominate the valve movement in the reference valve design, and are neglected in this version of the LPM for simplicity. However, these terms may easily be included in (3.17).

Determination of LPM parameters

The unknown parameters are determined based on a number of steady CFD simulations for various flow rates and directions with open valve positions, which is in turn combined to yield k_1,k_2 and $\gamma(Q, x)$ for each valve and for all valve positions. The steady CFD simulations are conducted on the geometry shown in figure 3.14 on page 59, with similar solver settings as those used in section 3.4. Depending on the open/close state of the HPV and LPV, the inactive manifold is disabled in the analysis. The boundary conditions are

specified by setting the manifold pressure constant and specifying a flow velocity at the piston top surface.

The resulting pressure difference between the piston surface and the manifold boundary is related to the energy dissipation and should therefore be included in the LPM. However, some corrections are needed when calculating the fluid force acting on the plunger resulting from this pressure difference, as only part of the total difference apply to the plunger itself (see right side of figure 3.16). Thus, $\gamma(Q, x)$ in equation (3.17) is in the range [0-1].

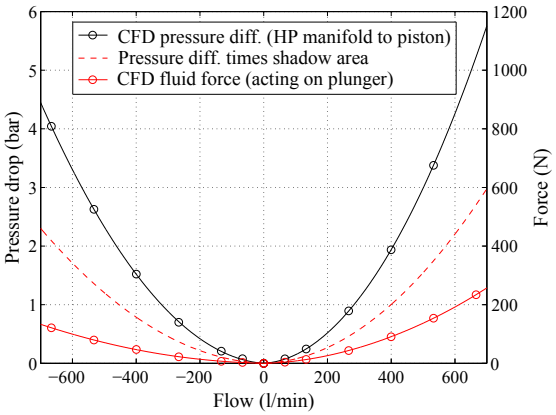

Figure 3.19: *Pressure difference as a function of flow rate and corresponding total force acting on the plunger from the surrounding fluid.*

Figure 3.19 shows the pressure difference between the HP manifold and piston surface and the corresponding plunger fluid force as a function of the flow rate, obtained using steady CFD results. As discussed above, the pressure difference times the shadow area leads to an overestimate of the fluid force, cf. figure 3.19. In addition, the pressure difference and forces are seen to be asymmetric with respect to flow direction.

The coefficients k_{1h} and k_{2h} (for each flow direction) is found directly from the CFD results in figure 3.19. In order to model the fluid force, the force-pressure correction function γ is determined as:

$$\gamma_h(Q_h, x_h) = x'_h f(Q_h) + (1 - x'_h) \ , \quad f(Q_h) = \frac{F_{\text{fluid}}(Q_h)}{A_{ph}\Delta p_h(Q_h)} \text{ for } \Delta p \neq 0 \qquad (3.18)$$

where x'_h is the normalized valve position, F_{fluid} the fluid force function obtained from the CFD analysis and Δp_h the corresponding pressure difference from the CFD analysis. At zero flow and thus zero pressure difference, $f(0) = 1$ is set to account for the singularity. This yields the pressure correction function γ shown in figure 3.20. For larger flow rates and open valve position, a force-pressure correction coefficient of 0.3 and 0.4 is necessary for the reference motor geometry. The form shown in (3.18) ensures unity γ at

times of closed valves, where the whole pressure difference acts on the plunger directly. Similar expressions are used for the LPV.

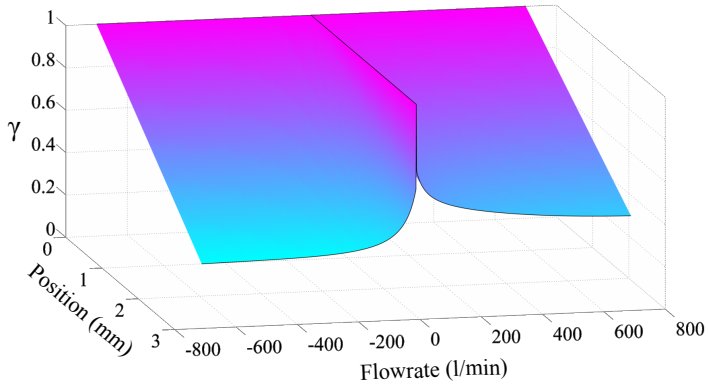

Figure 3.20: *Force-pressure correction coefficient γ as function of flow rate and valve position.*

The drag coefficients B_h and B_l are estimated using:

$$B_h = \frac{1}{2}\rho K A_{\text{fronth}} \ , \quad B_l = \frac{1}{2}\rho K A_{\text{frontl}} \tag{3.19}$$

where ρ is the fluid density, A_{fronth} and A_{frontl} frontal areas of the valve plungers and K a drag coefficient. The drag coefficient is, in general, dependent on Reynolds number. The flow induced drag force is included in the steady CFD analysis, and thus included in the first term of $F_{fluid,h}$ in (3.17), and the second term including B_h is included to account for the drag force resulting from valve movement in the LPM. The Reynolds number is low during valve switching, and a characteristic low-Reynolds-number drag coefficient $K = 5$ is thus chosen as an estimate [76].

Results comparison

The Lumped Parameter Model (LPM) and the transient CFD simulations are made using similar initial and boundary conditions; $p_h = 350$ bar, $p_L = 5$ bar, crankshaft rotation speed 1500 rpm. The valve actuator control is set to perform one idling operation cycle followed by a motoring operation cycle. Figure 3.21 shows a comparison between the LPM and the transient CFD model simulation.

From figure 3.21 it is seen that the LPM follows the overall characteristics of the CFD model, and that the CFD model exhibits a more oscillatory behavior compared to the simpler LPM. The major deviation appears in the valve opening (lower-left in figure 3.21), especially for the LPV opening which is offset by 1.5 ms. The force peaks present in the CFD solution (HPV force at 50 ms and LPV force at 71 ms) are due to reset of valve velocity as end positions are reached. The LPM predicts an efficiency of 98.0/93.2 %[4] while the CFD model predicts an efficiency of 98.3/93.9 % at 100/20 % displacement.

[4]In paper [F], the full displacement efficiency is incorrectly stated to be 97.1% due to erroneous parameter mismatch.

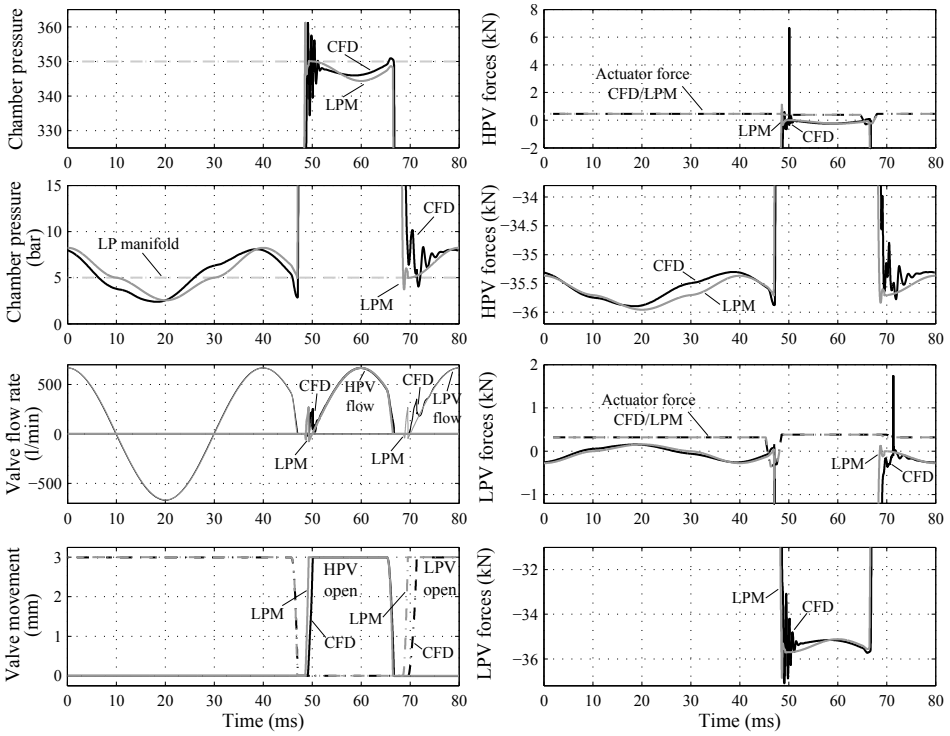

Figure 3.21: *Comparison between the Lumped Parameter Model (LPM) and the computationally expensive transient CFD model. The CFD chamber pressure is taken as the volumetric average.*

In total, the LPM response predicts the dynamic response with reasonable accuracy for the given design, even though the simulation is carried out in a small fraction of the time (< 1 min) it takes to conduct the transient CFD analysis.

The LPM can easily be used to study a range of operations, including the 'non-smooth' ranges which proved challenging using the transient CFD model above. Stiction effects may also be included in the LPM and the influence on the dynamic response may then be studied, as will be performed later in the next chapter with an optimized valve design. The LPM is thus considered much more useful in the design phase of large scale digital motors.

Chapter 4

Optimization Method for Digital Motor Valves

In this chapter an optimization method for DD motor valves is presented. With basis in a chosen valve topology, the method optimizes a number of subdomains within the valve design. An overview of the method is given in figure 4.1. Specifications of the target DD motor/pump unit and a valve topology selection forms the basis of a series of method elements (C-I), including three separate optimizations of design subdomains (C+D+I). The remaining elements are supporting studies, which are used in the design iterations or for rejecting a selected valve topology. The design method is described and shown applied in the following sections, with specifications suitable for a large scale DD motor in a wind turbine transmission.

The overall method is also discussed in paper [G], and the main elements are also presented in the papers [H-K], where additional details may be found.

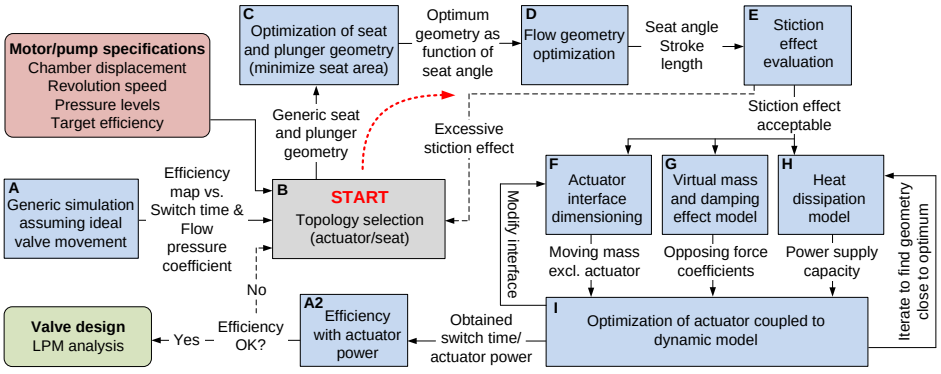

Figure 4.1: *Valve design optimization method overview. Solid arrows indicate normal design process flow and dashed lines are alternative routes in case the selected topology is found infeasible.*

4.1 Motor specifications

When aiming to replace current MW wind turbine drive trains with a hydrostatic transmission using DD units, the total drive train efficiency should be somewhat comparable with current known solutions. As discussed in the introduction chapter (figure 1.5 on page 4), current drive trains exhibits a full load efficiency of approximately 95 % and 85-90 % efficiency at 20 % load. Targeting, for instance, a total drive train efficiency of 85 % at 20 % load, and assuming a typical generator efficiency of 98 % and the hydraulic piping to have an efficiency of 99 %, the pump and motor unit must both maintain a total efficiency of:

$$\eta = \sqrt{\frac{0.85}{0.98 \cdot 0.99}} = 93.6\% \tag{4.1}$$

This corresponds well with the 20 % part load efficiency of state of the art DD machines (figure 1.17 on page 16). Payne et al. [77] shows a typical distribution of different losses in a small scale DD machine, where it is shown that valve losses accounts for approximately 12 % of the total energy losses at 20 % displacement. These results are derived based on experimental measurements.

This, in turn, corresponds to an estimated needed efficiency for the drive train pump and motor of 99.2 % when disregarding losses other than valve flow losses! Indeed, this highlights the tough requirements for the valves in efficient DD machines. A 99 % efficiency at 20 % displacement is thus used as target in the valve design method given in this chapter, which initially only includes flow losses.

The remaining motor specifications are set based on current state of the art MW DD motors, as shown in table 4.1. The specific displacement chosen is somewhat arbitrary, but is in range of the existing large scale motors made by AIP. A similar cylinder bore/stroke ratio as that chosen for the design example is mentioned in [77].

Table 4.1: *DD machine specifications for example valve design*

Chamber displacement	141 cc
Cylinder bore/stroke	60/50 mm
Revolution speed	1500 rpm
Pressure levels	350/5 bar
Target efficiency	>99% @ 20% displacement

An overall motor construction using a number of stacked 'slices' as illustrated in figure 3.12 on page 55 is assumed, and the maximum valve dimensions are hereby constrained by the width of such a 'slice'. For compact motor designs, the cylinder bore should be comparable in size to the 'slice' width, with some appropriate overhead. As a result, the maximum diameter of the valve is close to the cylinder bore.

4.2 Ideal efficiency evaluation and topology selection (element A/B)

Referring to figure 4.1, element A and B of the design method is to obtain a general efficiency map giving the overall valve requirements and to do a topology selection based on these overall requirements and the machine specifications. These steps were discussed previously in section 3.1 and 3.2. Annular valve seat geometry and a moving coil topology are used as basis for the valve design optimization, as illustrated in figure 4.2.

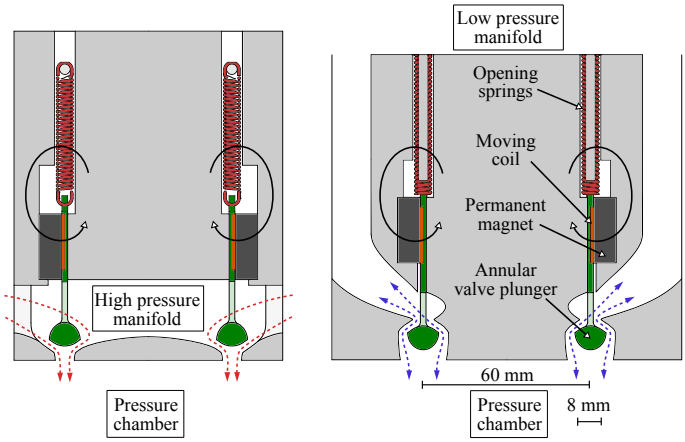

Figure 4.2: *HPV (left) and LPV (right) valve topologies selected for design optimization. Preloaded springs act to open both valves.*

The HPV and the LPV are assumed similar in size and topology, and the design method steps therefore apply to both valves. A valve diameter of 60 mm is selected based on the assumed cylinder bore, and a flow width of 8 mm is somewhat arbitrarily selected. Large flow widths compared to the valve diameter increases the difference in loading of the inner and outer seating surfaces, which is undesirable for the chosen seating geometry with equal inner and outer seat lengths. This aspect is discussed later in the following section.

4.3 Optimization of seat and plunger geometry (element C)

Having selected a seat topology and overall size, an optimization of the seat and plunger geometry may be conducted. The seat and plunger geometry and its design parameters are shown in figure 4.3. The valve plunger is made of reinforced PEEK contacting the steel seat with two surfaces. As the seat geometry is shown in figure 4.3, high pressure loading is applied from below during operation (chamber pressure for the LP valve and manifold pressure for the HP valve).

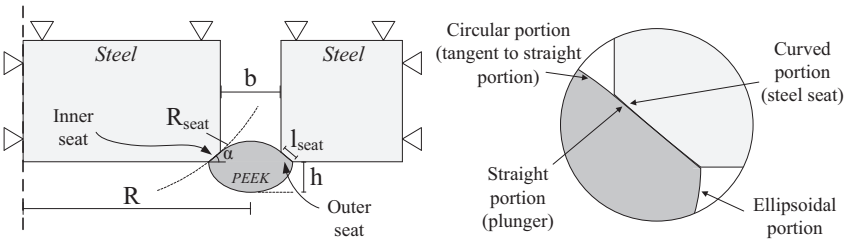

Figure 4.3: *Geometry parameters of the valve seat and plunger.*

For fast switching performance, the seat area should be minimized while maintaining the material stresses below the allowed threshold. In order to obtain force equilibrium, the seat forces must counteract the resulting pressure force acting on the plunger (upwards in figure 4.3). Small values for the seat angle α decrease the needed seat area, whereas larger angles require larger contact areas to counteract the increased seat force without exceeding the allowable material stresses. Therefore, low values of α might seem like the logical choice, however such geometry also increases the pressure drop of the valve by creating a less streamlined flow path. Some combined optimization is thus needed to determine the best choice of seat angle, which is later done in element D, cf. figure. 4.1. Initially, the seat and plunger geometry is optimized for a range of seat angles in this section (element C).

The plunger geometry, shown in figure 4.3, is determined by an upper circular part, a lower ellipsoidal part sized by h and two straight parts which are angled at α with respect to horizontal. The steel valve seat is curved with a radius set by R_{seat}, and the seat has a length determined by l_{seat}. In total four design parameters exist for the annular seat valve. The steel seat curvature is included to enable a reasonable contact pressure distribution of the seats, as two parallel surfaces would result in undesirable contact pressure peaks. The issue of obtaining approximately uniform contact pressure is discussed in [78].

When the pressure chamber is pressurized, the plunger is forced towards the seat and should be capable of transferring this fluid pressure force to the steel seats without experiencing undesirable large material stresses. In addition, the seat contact surface should preferably experience an even pressure distribution throughout its length, in order to minimize the seat length and thereby limit the stiction effect when opening

the valve. The following sections describe the model used for evaluating the plunger material stresses and seat pressure distribution under fluid pressure load. The cylinder chamber load pressure is set to 400 bar, corresponding to a manifold pressure of 350 bar with overhead to account for pressure peaks in the dynamic pressure chamber response.

Material model

The carbon fiber reinforced PEEK material[1] is modeled by assuming isotropic material properties, and using a Multi-linear Isotropic Hardening model, by which the stress-strain curve of the material is approximated by a piecewise linear curve [79]. Data for the engineering stress-strain curve are taken from [62], and in turn converted to true stress-strain. The assumption of isotropic material properties follows the idea that the short reinforcement fibers are all oriented randomly in all directions. However, some extend of main fiber orientation is expected [80], inducing an uncertainty in the model results shown for the example design. If the anisotropic properties of the material and the manufacturing details are known, the 2D model described in the following is able to account for the anisotropic effect (assuming the main fiber alignment to be along the radial, longitudinal or angular direction).

Young's modulus and Poisson's ratio used in the material models for PEEK/steel are 25/200 GPa and 0.4/0.3 respectively. The steel seat material is modeled to behave linearly due to the relatively large strength compared to the plunger material. The relatively large stiffness ratio is beneficial with respect to the sealing capabilities of the valve, as the PEEK material is able to adapt to the stiffer steel seat effectively.

Meshing of solution domain

The axisymmetric geometry shown in figure 4.3 is meshed from CAD data using an unstructured meshing algorithm with relatively small elements in the seat region and coarser meshing away from the seating area. A typical mesh consist of 10k elements. Due to the relatively low stiffness of the plunger material compared to the steel seat, the plunger slides a small distance relative the steel seat when subjected to the fluid pressure load. To accurately model this effect contact elements are utilized in the seat region. Specifically, the surface-to-surface contact elements TARGE169 and CONTA172 available in the ANSYS software package is used. A detailed view of the seat and plunger region mesh in given in figure 4.4. Contact element configuration settings follow the guidelines given in [81].

A coefficient of friction of 0.1 is specified for the seat surfaces, estimated on basis of data from [62]. Here a coefficient of friction of 0.28 is specified in dry condition, and a lowered coefficient of friction is expected due to the oil-lubricated operation condition of the valve.

[1] Simply referred to as PEEK for convenience, specific name Victrex 450CA30. Reinforced with 30 % short carbon fibers.

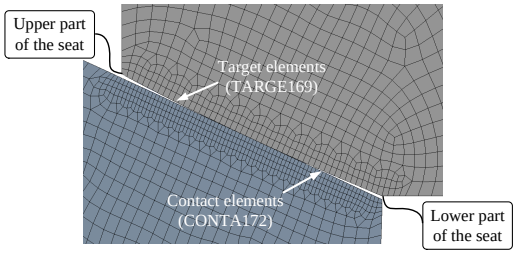

Figure 4.4: *Detail view of seat region meshing, the mesh is refined near the seat edges, and contact elements specified to allow simulation of relative motion between plunger and steel part of the seat.*

Fluid pressure load

Due to the penetrating nature of a pressurized fluid, the actual load experienced by the plunger is dependent on the deflection of the plunger itself. It is therefore not directly possible to apply the fluid pressure load to some predetermined shadow area. The area of the plunger which is subjected to the pressure load depends on the magnitude and distribution of the seat contact pressure. To accommodate this behavior in the model, the fluid pressure load is updated at each load iteration performed by the solver, such that fluid pressure is only applied in regions where the contact pressure is below the fluid penetrating pressure. An example of this load situation is shown in figure 4.5.

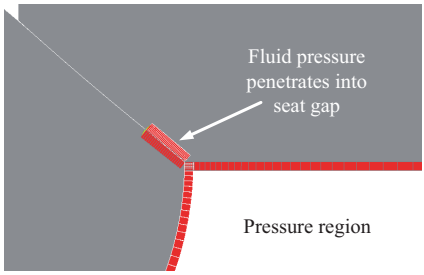

Figure 4.5: *Detailed view of seat region when applying penetrating fluid pressure. Fluid pressure load is applied to regions where the contact pressure is below fluid pressure level. The fluid pressure load is updated at each solver iteration.*

The fluid pressure load is applied in three load steps in order to improve/enable convergence of the solution. Firstly, the lower half of the plunger nodes are displaced 2 μm towards the seat in order to initiate seat contact in a stable controlled way [81]. Secondly, the displacement constraint from load step one is removed and replaced with a non-penetrating fluid pressure corresponding to the reaction force present due to the initial displacement load. Lastly, the penetrating fluid pressure is applied starting from load step two. This approach has been found necessary to ensure stability/robustness of the solution when used for a wide variety of geometries.

The finite element analysis (FEA) described above is non-linear due to the non-linear stress-strain relationship of the plunger material, the contact elements and the corresponding fluid penetrating pressure load. That is,

$$\underline{K}(\mathbf{u})\,\mathbf{u} = \mathbf{F^a}(\mathbf{u}) \tag{4.2}$$

where $\underline{K}$ is the stiffness matrix, $\mathbf{u}$ the displacement vector and $\mathbf{F^a}$ the applied load vector. As the stiffness matrix and load vector depend on the displacement itself, equation (4.2) is non-linear and $\mathbf{u}$ satisfying (4.2) is found using a Newton-Raphson iteration method [82]. Convergence of the iteration method is only guaranteed for an initial guess close to the exact solution, and therefore each load step is applied in smal increments where each new increment uses the solution from the previous increment as initial guess.

Material stress evaluation

Having a fracture elongation of only 1.5%, the short fiber reinforced PEEK plunger material is classified as a brittle material. In addition, the composite PEEK material is uneven, that is, exhibits a larger compressive strength compared to the tensile strength. A yield criterion commonly used for strength evaluation of ductile materials is thus not applicable. Therefore, to find an effective material stress comparable to the design tensile strength, a modified-Mohr effective stress is utilized. The effective material stress is then given as,

$$\begin{aligned}
\widetilde{\sigma} &= max\left(C_1, C_2, C_3, \sigma_1, \sigma_2, \sigma_3\right) \\
C_1 &= \frac{1}{2}\left[|\sigma_1 - \sigma_2| + \frac{2S_{ut} - |S_{uc}|}{-|S_{uc}|}\left(\sigma_1 + \sigma_2\right)\right] \\
C_2 &= \frac{1}{2}\left[|\sigma_2 - \sigma_3| + \frac{2S_{ut} - |S_{uc}|}{-|S_{uc}|}\left(\sigma_2 + \sigma_3\right)\right] \\
C_3 &= \frac{1}{2}\left[|\sigma_3 - \sigma_1| + \frac{2S_{ut} - |S_{uc}|}{-|S_{uc}|}\left(\sigma_3 + \sigma_1\right)\right]
\end{aligned} \tag{4.3}$$

where $\sigma_1, \sigma_2, \sigma_3$ are the principal stresses and $S_{ut} = 245$ MPa and $S_{uc} = 300$ MPa is the ultimate tensile and compressive strength respectively [78]. The principal stresses are solved within the FEA and used to evaluate $\widetilde{\sigma}$ throughout the PEEK material region.

Seat wear is expected to be limiting for the lifetime of the plunger, and assumed dominating compared to material fatigue, as the plunger and seat material primarily experiences compression loading. An allowable effective stress $S_{allow} = 170MPa$ is set based on the ultimate tensile stress and a safety factor of approximately 1.5 to account for uncertainty in material data and model results. The compressive fatigue strength is assumed to be larger than S_{allow} based on the manufacturer specifications of the fatigue strength in tension, however, this is a topic for further research.

Optimization algorithm

By varying the design variables $\mathbf{x} = [\alpha, h, l_{seat}, R_{seat}]$ and solving the FEA, a set of design solutions may be found. Different optimization strategies could be applied for seeking optimum designs, but a low level method has been applied for the example design.

The method used is termed brute force, as it simply analyses all design variations in a grid imposed on the design space. This method is computationally expensive but gives insight into the characteristics of the whole solution space, and does not require gradient information. Figure 4.6 illustrates the algorithm used for finding optimal design points, where the algorithm framework and file handling is implemented in Matlab.

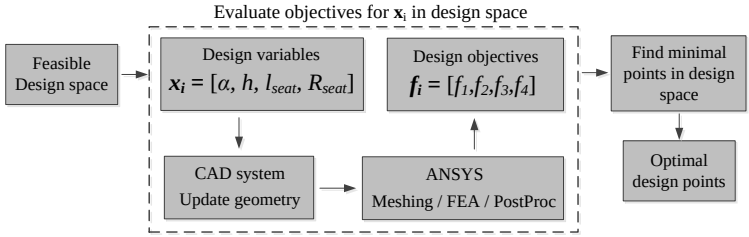

Figure 4.6: *Algorithm used to locate optimal design points, for each design point the CAD system (SolidWorks) is used to update the geometry description before conducting the FEA analysis.*

To evaluate the design solutions, four objectives $\mathbf{f} = [f_1, f_2, f_3, f_4]$ are utilized. These objectives are evaluated for each design $\mathbf{x}$, based on the solution of the non-linear FEA.

An overview of the design objectives is given in table 4.2. These objectives indicate, if close to zero, a design with proper utilization of the plunger material strength and a proper utilization of the contact seat. Objective f_1 is calculated as the absolute difference between the allowable effective stress and the maximum effective stress in the plunger region, where the effective stress is found from (4.3).

Table 4.2: *Design objectives used for evaluating design points*

f_1	$\lvert S_{allow} - max\,(\widetilde{\sigma}\lvert_{\text{Plunger region}})\rvert$	$\widetilde{\sigma}$ calculated using (4.3)
f_2	$\lvert U_{ref} - U_{L,mean}\rvert$	Seat excess lower
f_3	$\lvert U_{ref} - U_{U,mean}\rvert$	Seat excess upper
f_4	Bad contact pressure distribution?	Output 1 or 0

The objectives f_2, f_3, f_4 are most easily described by considering a solution example. Figure 4.7 shows a typical example of seat contact pressures. Examples of effective stress distributions are given later in this section, cf. figure 4.10 and 4.11. As seen in figure 4.7, the excess seat lengths $U_{L,mean}$ and $U_{U,mean}$ describe the mean distance from the seat ends to a contact pressure above zero. Further, $U_{L,mean}$ and $U_{U,mean}$ is normalized to the seat length. Following the example of figure 4.7, $U_{U,mean} = 5\%$ and $U_{L,mean} = 17\%$. The reference for seat excess length is selected to be $U_{ref} = 5\%$, as a small excess length is desired, but some length is needed to account for variations between inner and outer seat pressure distribution. This variation in contact pressure for the inner and outer seat is a consequence of the difference in inner and outer seat area in the axisymmetric geometry.

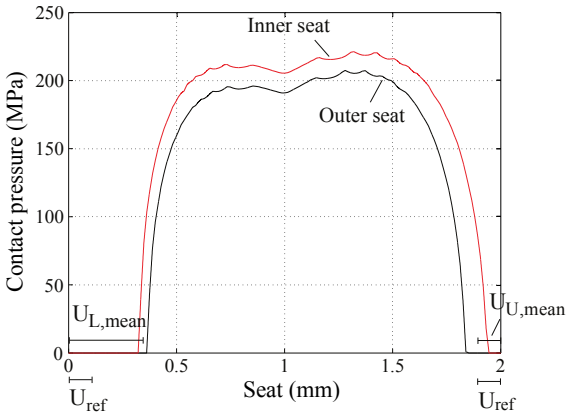

Figure 4.7: *Example of contact pressure distribution in outer and inner plunger seat.*

The last design objective f_4 is included to capture contact pressure distributions which, when evaluated only based on seat excess lengths $U_{L,mean}$ and $U_{U,mean}$, seem to give good utilization of the seat region, but exhibit spike behavior typically at the upper part of the seat (the part away from the fluid pressure, cf. figure 4.4). Proper 'decreasing towards seat ends' pressure distributions as shown in figure 4.7 are wanted, as other distributions indicates that the design is or is close to slide onto the seat end. Objective f_4 is either 1 or 0, and calculated by computing the mean seat contact pressure and comparing this value to the mean pressure when taken over only the last 10% of the pressurized seat length. If the last 10 % of the seat exceeds the mean contact pressure, $f_4 = 1$. For a given design, all four end locations are checked (lower and upper part of both inner and outer seat).

Having multiple objective functions, some method for selecting optimum designs from these objectives is needed. Designs with $f_4 = 1$ are directly discarded. The remaining designs are then tested for the condition $f_1 < 25$ MPa, and those not fulfilling discarded. Finally, the optimum (minimum) design $\mathbf{x}_{min}$ is then considered to be,

$$\mathbf{x}_{min} = \{\mathbf{x} \in M_\alpha | min(|f_2(\mathbf{x})| + |f_3(\mathbf{x})|)\} \tag{4.4}$$

where M_α is the set of feasible designs fulfilling the above requirements for f_1 and f_4, for the seat angle α. This selection of optimum selects the design with best seat utilization, which in turn minimizes the seat length.

Design grid for the brute force optimization

The main drawback of using a brute force algorithm for finding the design minimums is the computational expense. Having four design variables, the total number of computations needed quickly becomes enormous if care is not taken to limit the problem size. The strategy used for the example design is to calculate initial guesses for the design region and then search in a region somewhat close to the initial guess.

Due to the seat valve application, the seat angle α is limited to be in the set $\{20, 25, ..., 70\}$ deg, and the height h is assumed to be within the set $\{0.5, 1.5, ..., 1.5b\}$ mm. The remaining design variables l_{seat} and R_{seat} are harder to intuitively set limits on, and are therefore estimated based on analytic force calculations. As simplifying assumptions to these analytic expressions, the seat contact pressure is set constant throughout the seat length, and equal in size for both inner and outer seat. Using this, the seat length l_{seat} may be estimated by virtue of force equilibrium:

$$\widehat{l}_{\text{seat}} = \frac{b\, p_{\text{load}}}{2\cos\alpha(p_{\text{cont}} - p_{\text{load}})} \tag{4.5}$$

where p_{load} is the pressure chamber load pressure and p_{cont} the contact pressure. The load pressure is 40 MPa, and from initial analysis studies it is known that a contact pressure in the region of 200 MPa leads to effective stresses in the vicinity of S_{allow}, and this contact pressure level is thus used for estimation purposes. As this seat length estimation is based on 100% utilization of the plunger seat, it falls in the lower region of feasible seat lengths. The feasible seat length set is then set to $\{\widehat{l}_{\text{seat}}, \widehat{l}_{\text{seat}} + 0.1, \cdots, 2.0\widehat{l}_{\text{seat}}\}$.

The seat radius R_{seat} is estimated using the analytical solution for cylinder-on-cylinder (infinite radius for the straight special case) elastic contact. This analytic expression take into account different material properties of the target and contact part [78], and is illustrated in figure 4.8. Here, $\nu_{\text{steel}} = 0.3$ / $\nu_{\text{PEEK}} = 0.4$ is Poisson's ratio for

$$\widehat{R}_{\text{seat}} = \frac{\pi \widehat{l}^2_{\text{seat}} L_{\text{seat}}}{16 F_{\text{seat}}(m_{\text{steel}} + m_{\text{PEEK}})} \tag{4.6}$$

$$\text{with} \quad L_{\text{seat}} = 4\pi R \quad \text{and} \quad F_{\text{seat}} = \frac{2\pi R\, b}{\cos\alpha}\, p_{\text{load}}$$

$$\text{and} \quad m_{\text{steel}} = \frac{1-\nu^2_{\text{steel}}}{E_{\text{steel}}} \quad m_{\text{PEEK}} = \frac{1-\nu^2_{\text{PEEK}}}{E_{\text{PEEK}}}$$

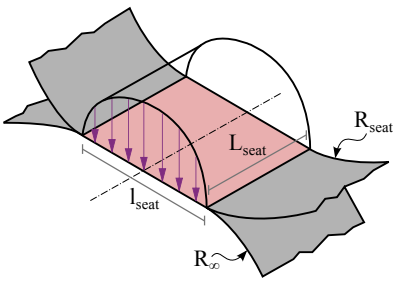

Figure 4.8: *Pressure distribution seat contact.*

the steel and PEEK material respectively and $E_{\text{steel}} = 200GPa$ / $E_{\text{PEEK}} = 25GPa$ are Young's modulus for the materials. Using (4.6) the feasible set of R_{seat} is set to $\{0.5\widehat{R}_{\text{seat}}, 0.5\widehat{R}_{\text{seat}} + 1.0, \cdots, 1.25\widehat{R}_{\text{seat}}\}$ mm.

Using these sets as input for the brute force design search, the feasible set contains approximately 12k points. Some distances between the design points are present in the brute force search, and small improvement may therefore be expected in a refined optimization. A typical design takes a couple of minutes to simulate, and the final optimization analysis was completed in 2-3 weeks.

Results

The resulting set of minimal points $\mathbf{x}_{min}$ is shown graphically in figure 4.9, where the height h, length l_{seat} and radius R_{seat} are shown as a function of seat angle α. The needed seat length increases with increasing seat angle, which is expected as the projected area decreases with larger seat angles. The needed height h decreases linearly with increasing seat angles.

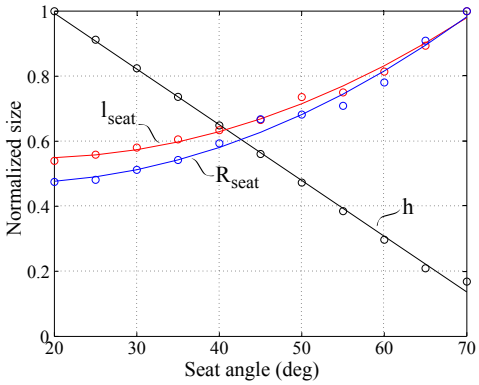

Figure 4.9: *Minimal design point values as a function of seat angle, Non-normalized maximum values:* $h = 8.31$ *mm,* $l_{seat} = 2.8$ *mm and* $R_{seat} = 45.1$ *mm.*

Two effective stress distributions of minimal design points are given in figure 4.10 and 4.11, clearly showing the increasing tendency of the seat length and decreasing tendency of the height with increasing seat angle. The contact pressure of the inner seat is generally larger than the outer seat by a relatively small margin, which follows from the static plunger torque equilibrium where the ratio of the inner and outer seat force is larger than the ratio of the inner and outer seat area[2]. This difference increases for larger b/R ratios, and different inner and outer seating areas may be included in the design to account for this effect. For improper valve designs with larger b/R ratios, this asymmetric effect may lead to poor valve sealing, which is also discussed in [83].

[2]Consider a simple flat annular plate with an uniform pressure difference, width b, a mean radius R and reaction forces F_o,F_i for the outer and inner plate edges respectively. Due to the axisymmetric geometry, the outer reaction force is larger than the inner, with the ratio $\frac{F_o}{F_i} = \frac{R+b/6}{R-b/2}$. Assuming an equal inner and outer seat length leads to a ratio between inner seat pressure and outer seat pressure $\frac{p_i}{p_o} = \frac{R+b/2}{R+b/6}$>1. For the example design $\frac{p_i}{p_o} = 1.09$.

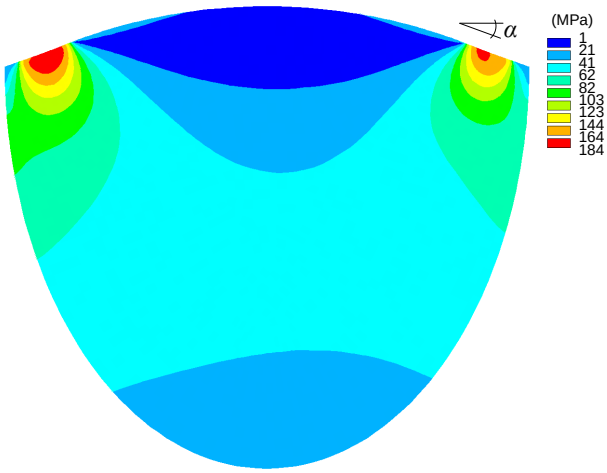

Figure 4.10: *Effective stress $\widetilde{\sigma}$ distribution in plunger region for a minimal design point, $\alpha = 20deg.$* $\mathbf{f} = [14.96, -0.15, 0.03, 0]$

In general, the plunger mass may be used as additional design objective. For the example geometry, however, only a slight difference of a few grams were observed throughout the chosen design space, which is small compared to the total moving mass. Mass was therefore not explicitly used as objective for the example design.

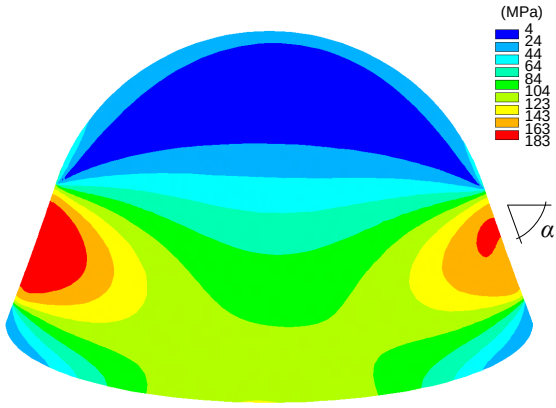

Figure 4.11: *Effective stress $\widetilde{\sigma}$ distribution in plunger region for a minimal design point, $\alpha = 70deg.$* $\mathbf{f} = [13.46, -0.08, 0.03, 0]$

4.4 Flow geometry optimization (element D)

From the result of method element C, the optimal plunger and seat geometry is known for a given seat angle. However, this does not give an answer as to which seat angle to select. Clearly, a large seat angle gives a smaller area gradient but does allow for a more smooth flow passage of the valve plunger and conversely for a small seat angle. What combination of seat angle and stroke length should then be selected? In this method element, steady CFD simulations are carried out for various seat angles and stroke lengths, in order to find a suitable combination when considering efficiency.

Figure 4.12 illustrates the fluid domain and boundary conditions used for conducting the CFD analyses. Both positive and negative inlet velocity may be applied to simulate flow in both directions. Different selections of seat angle alter the valve geometry as shown in the square boxes in figure 4.12, corresponding to the results from element C.

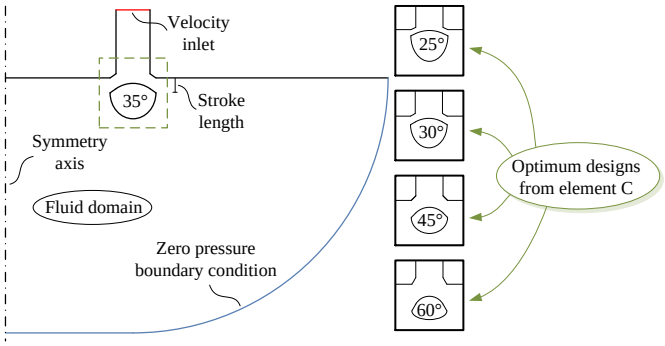

Figure 4.12: *Fluid flow problem description. The valve stroke length and seat angle is varied, and a zero pressure boundary condition is applied together with a velocity inlet.*

The steady CFD analyses are carried out using the commercial software package Ansys Fluent 14.5, including a viscous RNG k-ϵ model with enhanced wall treatment, similar to the previous CFD simulations. An unstructured, quad-dominant, mesh is used to model the fluid domain, typically containing 35k elements (depending on specific geometry). Each solution is converged until all scaled residuals are below 10^{-4}.

The mesh density is increased near the seating area to account for increased field gradients, and a mesh independence study has been used to select a prober compromise between solution accuracy and computational cost. Increasing the number of elements to 95k lead to a variation in valve pressure drop below 1 percent, whereas a solution using 12k elements changed the pressure drop 7 percent when compared to 35k elements.

An example of the resulting velocity and pressure field of a CFD analysis with nominal flow rate is shown in figure 4.13 and figure 4.14. As expected, the main pressure drop occurs in the valve seat region, and the largest flow velocities are seen between the seating faces.

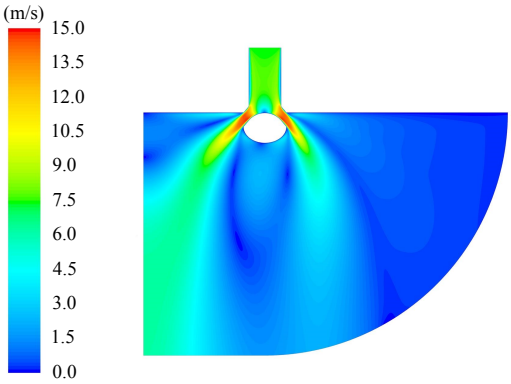

Figure 4.13: *Resulting velocity field for a CFD analysis. Inlet velocity* 666 *l/min, stroke length* $l_s = 3.5$ *mm and seat angle* $\alpha = 50$ *deg.*

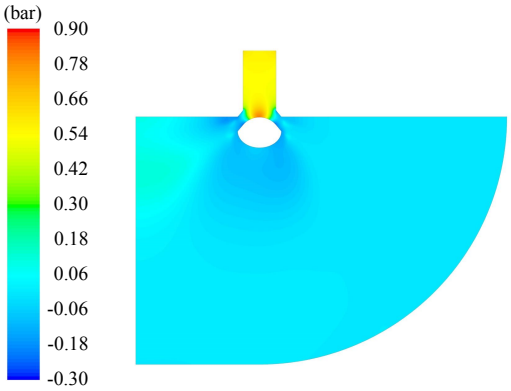

Figure 4.14: *Pressure field (Pa) corresponding to the velocity field shown in figure 4.13. Pressure difference between inlet and zero pressure boundary is* 0.57 *bar.*

During displacement operation of the reference motor, the seat valves are subjected to flow rates in the range ±666 l/min, and the pressure drop is generally not symmetrical for positive and negative flow rates. In order to describe the flow-pressure characteristics of each valve design conveniently with a single scalar quantity, the orifice equation is utilized:

$$Q = \frac{1}{k_f}\sqrt{|\Delta p|}\,\mathrm{sign}\Delta p \tag{4.7}$$

where Q is the flow rate, k_f the flow coefficient and Δp the pressure drop across the valve. For high efficiency, low values of k_f are pursued. This relationship (using one k_f for positive flow and another for negative flow) approximately fits the simulated pressure drop for flow rates in the application range, as shown in figure 4.15.

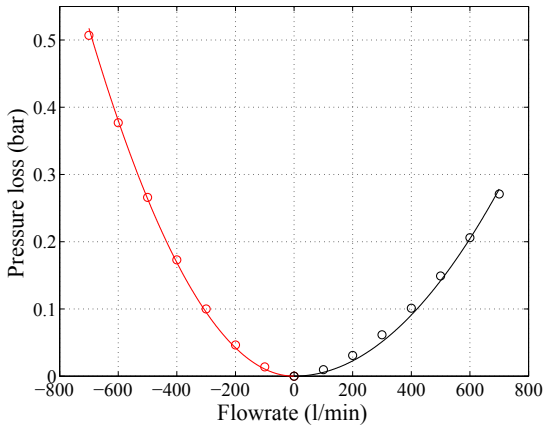

Figure 4.15: *Pressure drop vs. flow rate comparison between CFD results (circles) and a model using equation (4.7). Different values of k_f are used for positive and negative flow directions.*

To ease further analysis, an equivalent flow coefficient $k_{f,eq}$ is introduced, combining the in - and outflow coefficient. This equivalent flow coefficient is derived by assuming equal energy loss between a valve with an asymmetrical flow-pressure relationship (figure 4.15) and one with a symmetrical relationship:

$$E_{loss,sym} = E_{loss,asym} \tag{4.8}$$

Using equation (4.7), the valve energy loss is given as:

$$E_{loss} = \int Q\Delta p dt = \int Q\,\mathrm{sign}(Q)Q^2k_f^2 dt = \int |Q|^3 k_f^2 dt \tag{4.9}$$

For asymmetric flow-pressure relation this leads to a cycle energy loss:

$$E_{loss,asym} = k_{f,in}^2 \int_{in} |Q|^3 dt + k_{f,out}^2 \int_{out} |Q|^3 dt \tag{4.10}$$

The absolute value of valve flow, $|Q|$, is equal during intake and discharge of a reciprocating piston, leading to equal values of the integrals in equation (4.10). Denoting these integrals C, and making the analogue expression for the symmetrical loss gives:

$$\left.\begin{array}{c} E_{loss,asym} = Ck_{f,in}^2 + Ck_{f,out}^2 \\ E_{loss,sym} = 2Ck_{f,eq}^2 \end{array}\right\} k_{f,eq} = \sqrt{\frac{k_{f,in}^2 + k_{f,out}^2}{2}} \tag{4.11}$$

where $k_{f,in}$, $k_{f,out}$ and $k_{f,eq}$ are the inflow, outflow and equivalent flow coefficient respectively. This selection of flow coefficient ensures equality in energy loss between a valve with an asymmetrical flow relation and one with a symmetrical flow relation. In the following the equivalent flow coefficient will be denoted simply as k_f. In addition, the normalized flow coefficient $\overline{k}_f$ is utilized (as previously introduced, cf. section 3.1):

$$\overline{k}_f = \frac{k_f}{k_f^*} \quad \text{with} \quad k_f^* = \frac{\sqrt{p_H - p_L}}{Q_{mean}} \tag{4.12}$$

The normalized flow coefficient is used as design parameter for evaluating the result of each CFD analysis. The seat angle is varied from 20-70 deg in 5 deg increments, and the valve stroke is varied from 1-10 mm in 0.5 mm increments.

Results

Contours of $\overline{k_f}$ as a function of the valve seat angle and stroke length are given in figure 4.16. Generally the flow coefficient increases when lowering the stroke length, as expected. When considering the combined valve performance, it is desirable to limit the stroke length in order to minimize the switch time. Looking at the individual contour lines in figure 4.16, it is apparent that a minimum stroke length is present for a given flow coefficient, indicating that for a wanted flow coefficient, there is a seat angle leading to a minimum needed valve stroke. This minimum is most clearly seen for $\overline{k}_f < 3.5\%$.

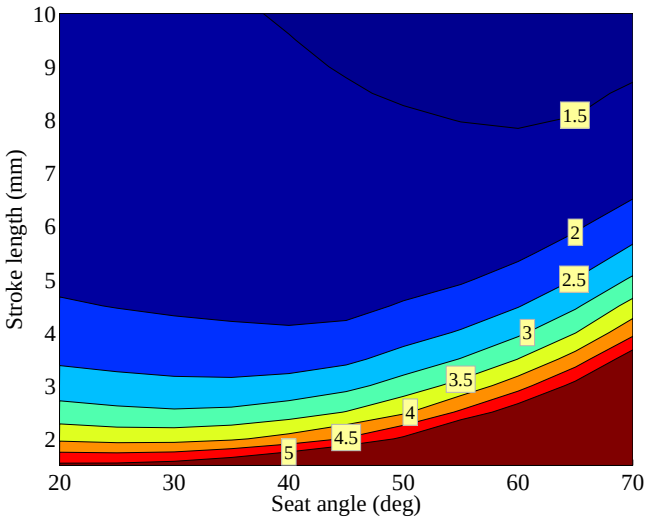

Figure 4.16: *Contours of normalized flow coefficient $\overline{k_f}$ (%) as function of seat angle and valve stroke length.*

Selecting the lowest stroke length for each flow coefficient leads to the relation between seat angles, stroke length and flow coefficient as shown in figure 4.17. Both the valve stroke length and valve seat angle increases with lower levels of normalized flow coefficient, with a rather steep increase in gradients for flow coefficients below $2 - 2.5$ %.

As previously outlined in method element C, the valve seat angle defines the optimum seat length, radius and plunger height (cf. figure 4.9). Thereby, the result given in figure 4.17 sets up a complete set of design dimensions for the annular seat valve example, with the normalized flow coefficient as parameter. The choice of flow coefficient is performed by considering the dynamics of the valve. The requirements for the valve actuator

increase with larger stroke lengths, as switching times must be kept low, preferably in the range 2-3 % of the revolution time, cf. figure 3.4 on page 46.

A compromise of $\overline{k}_f \approx 2.25\%$ is selected, where the lowest flow coefficient is obtained while avoiding the steep increase in stroke length for lower values of $\overline{k}_f$ seen in figure 4.17. Following this selection, the stroke length is set to 3.5 mm and the seat angle to 35 deg. This corresponds to a seat length l_{seat}=1.87 mm, a seat radius R_{seat}=28.3 mm and a plunger height $h = 6.1$ mm.

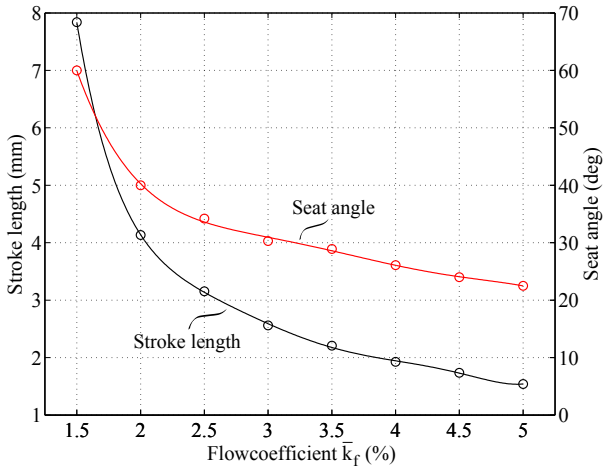

Figure 4.17: *Valve stroke length and seat angle as a function of normalized flow coefficient, $\overline{k}_f$. Best selection of stroke length and seat angle increase with lower values of flow coefficient.*

4.5 Stiction effect evaluation (element E)

Having determined the seat geometry in the preceding method elements, in particular the seat length and seat angle, the stiction effect during valve opening may be investigated. When attempting to drive to closely spaces parallel plates away from each other, as happens during passive opening of the DD valves, a restrictive force is present due to the pressure drop developed in the fluid film between the seat surfaces. Both the term 'stiction force' and 'squeeze force' have been used by different authors to denote this restrictive force, even though the term stiction (from static friction) is somewhat misleading as the restrictive force is temporal and dependent on the separation speed and surface distance. The force is here termed the stiction effect as some recent and historical publications adapts this terminology. Stiction forces are primarily of concern when opening the seat valves, as the contacting surfaces relevant for valve stiction during closing may be made small. The stiction effect is expected to be significant for the HPV, which is forced open at a high pressure level.

The effect of oil stiction within valve technology has been covered in several articles. In the field of compressor valves a number of papers treat the stiction effect, and models based on Reynolds theory are typically utilized, see e.g. [84, 85, 86]. A more advanced quasi-static model of fluid stiction is presented by Resch & Scheidl in [58], where the classical Reynolds theory based model is expanded to include a central cavitated zone, which is shown to provide good agreement with measurements for circular plates. In [59], a finite volume stiction model capable of including complex geometries is presented and shown to correspond well to a Reynolds theory based model for simple geometries. The models in [58, 59] are, however, applied to gaps with a considerable initial gap height compared to that present in pressure closed seat valves.

In design method element D, treated in this section, a stiction model for annular seat valves in DD applications is described, used to estimate the effect of stiction for the example valve design. Shortly before the valve plunger is driven away from seat contact, the plunger is pressed firmly against the seat with high pressure differential, and the initial height of the squeezed film is therefore near zero. In this situation, negative pressures in the fluid film (tension) has been observed for hydraulic seat valves [58]. An attempt has been made to include this negative pressure effect in the proposed stiction model, in combination with a dynamic cavitation zone.

A dynamic chamber pressure is combined with the stiction model for the seat valve, giving a simulation of the stiction effect when the HPV and the LPV is forced open by a dynamic pressure difference.

System model

The stiction analysis is performed with basis in the annular valve geometry shown in figure 4.2, where similar seat geometry is present for both the HPV and the LPV. Each valve have two seat surfaces (inner and outer), also of similar geometry but with different radius. When conducting time simulation of the stiction effect, the initial time is considered to be the instant where the chamber pressure equals the manifold pressure.

The chamber pressure primarily applies the valve opening force acting to drive the valve plunger away from the seat. This chamber pressure, p_c, is modeled considering a reciprocating piston to be connected to a closed volume using the continuity equation including a pressure dependent oil stiffness, similar to the pressure chamber models applied previously (see paper [J] for specific details).

The valve movement y_p is then determined from:

$$m\ddot{y}_p = A_{ps}(p_c - P) + F_{spr} - F_s(y_p, \dot{y}_p) \tag{4.13}$$

with m being the moving mass, A_{ps} the pressure shadow area, P the manifold pressure level, F_{spr} the opening spring force and F_s the stiction force arising when the average seat film pressure drops below P. Time integration of equation (4.13), with some initial position, gives the resulting plunger movement. The simulation is performed until the plunger position reaches $0.1mm$, at which point the stiction force is much smaller than the opening forces. An unrestricted ($F_s = 0$) plunger movement is simulated simulta-

neously, and the difference in time between the restricted and unrestricted arrival at $y_p = 0.1$ mm is denoted as T_{stic} and used to quantify the valve stiction effect.

Stiction model

The seat region pressure distribution is modeled with basis in Reynolds theory, commonly applied to problems containing thin fluid films, where the pressure across the film may be approximated as constant. Figure 4.18 illustrates the film geometry and the chosen parameters. A quasi-static approach is utilized, whereby the pressure distribution is assumed independent of time for a given set of boundary conditions. That is, for a given plunger position and velocity, the pressure distribution is given, which has been shown to yield accurate results for thin fluid film problems [58]. The annular valve studied in the present paper is rotational symmetric, but is modeled as a straight film in the angular direction due to the relatively low curvature. It may then be represented by the Reynolds equation in the following form [87]:

$$\frac{\partial}{\partial x}\left(\frac{h^3}{12\eta}\frac{\partial p}{\partial x}\right) = \frac{\partial}{\partial x}\left(\frac{hU}{2}\right) + \dot{h} \tag{4.14}$$

where p is the film pressure, η the dynamic fluid viscosity, U the relative velocity of the two surfaces in the x direction and $h(x), \dot{h}$ the film height and velocity respectively. In the following, $h(x)$ is simply denoted h.

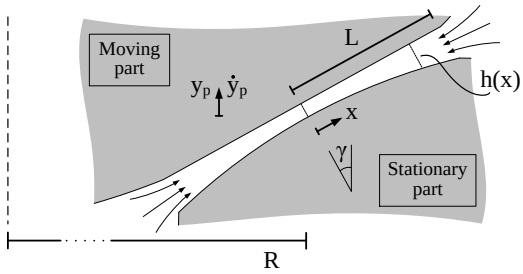

Figure 4.18: *Valve seating liquid film geometry. A flat surface (moving part) is forced away from the curved surface (stationary part), and stiction force arise as a local low pressure region in formed in the seat region.*

In equation (4.14) the first right hand term accounts for the wedge effect created as h varies with x and a relative velocity is present. While this effect is present for the seat film, it is insignificant as the curvature of the stationary part is small (that is, $\frac{\partial h}{\partial x}$ is small and also $\frac{\partial U}{\partial x} = 0$). In addition, the wedge effect for the geometry in figure 4.18 has no effect on the average pressure in the simplest solution of Reynolds equation, and does there not affect the total stiction force. For simplicity this term is therefore neglected,

leading to a general solution of equation (4.14) in the form:

$$p = \int \frac{\int e^{\int F(x)dx} M(x)dx + C_1}{e^{\int F(x)dx}} dx + C_2 \tag{4.15}$$
$$F(x) = \frac{h}{3}\frac{\partial h}{\partial x} \quad M(x) = \frac{12\eta}{h^3}\dot{h}$$

where C_1, C_2 are integration constants depending on the boundary conditions imposed. The film height h is described by,

$$h = kx^2 + y \quad \text{where} \quad y = y_p \cos\gamma \quad \text{and} \quad \dot{h} = \dot{y}_p \cos\gamma \tag{4.16}$$

where k is used to describes the seat curvature. This leads to the following general pressure distribution expression for the problem considered:

$$p(x) = \frac{1}{4}\frac{C_1\, kx - 12\,\dot{h}\,\eta\, y}{yk\left(kx^2 + y\right)^2} + \frac{3}{8}\frac{C_1\, x}{y^2\left(kx^2 + y\right)} + \frac{3}{8}\frac{C_1 \arctan\left(\frac{kx}{\sqrt{yk}}\right)}{y\sqrt{yk}} + C_2 \tag{4.17}$$

Further, the mean fluid velocity $\overline{u}$ is given by [87]:

$$\frac{\partial p}{\partial x} = \mu\frac{\partial^2 u}{\partial y^2} \quad \text{with} \quad u(y=0) = u(y=h) = 0 \Downarrow \tag{4.18}$$
$$\overline{u} = \frac{1}{h}\int_0^h u(y)\,dy = -\frac{1}{12\eta}\frac{\partial p}{\partial x}h^2 \tag{4.19}$$

The simplest solution for the seat pressure distribution $p(x)$ is obtained with Dirichlet boundary conditions, $p(L) = p(-L) = p_0$, leading to:

$$p(x) = \frac{L^4k^3p_0 + 2L^2k^2p_0y + kp_0y^2 + 3\dot{h}\eta}{k\left(L^2k + y\right)^2} - \frac{3\dot{h}\eta}{k\left(kx^2 + y\right)^2} \tag{4.20}$$

where p_0 is the boundary pressure. Whenever cavitation effects are not present, equation (4.20) describes the film pressure distribution. As the moving part is pressed strongly against the stationary seat just before opening, the initial height is near zero (especially at the film center where $x = 0$), and equation (4.20) approaches negative infinity as $y \to 0$, for $x = 0$. Thus, local cavitation in the seat film may occur even for valves surrounded by high pressure levels when initiating motion with very small initial heights.

When quickly separating parallel surfaces, liquid is able to withstand pressures below the vaporization pressure without cavitating for short periods of time [88]. This may lead to stiction forces exceeding the expected maximum stiction force (from the seat area and pressure difference between the surrounding and the vaporization pressure). Typically, such negative pressures (tension) only exist in fractions of a millisecond, but may be several times the atmospheric pressure (~ -4 bar reported in [58]). Physically, this behavior is connected to the fact that it takes some amount of time for cavitation bubbles to form (liquid to vaporize), before a cavitated zone is created with near zero pressure inside. This process is difficult to model accurately, and also highly dependent on the surrounding surfaces and liquid impurities (nucleations), which may vary with valve operation [88].

In the stiction model a tensile strength (minimum negative pressure) is defined, $p_{min} = -5$ bar, to account for the possibility of added stiction force due to tensile stress in the film liquid. The main idea is that this model should be able to simulate worst case scenario with respect to oil stiction.

Stiction force model with central cavitation zone

In case of cavitation, the seat film is separated in three zones; a central cavitation zone with zero pressure and liquid filled zones described by the Reynolds equation. The below model has been developed with inspiration in the work conducted by Resch & Scheidl [58], but the model is expanded with the possibility of liquid tension and the cavitation zone dynamics is interpreted differently.

Depending on the velocity and position development over time, the seat film may cavitate or stay above the minimum pressure and avoid cavitation. Three situations of the fluid film is included in the stiction model with the Reynolds equation boundary conditions shown below:

1. No cavitation present
   $p(L) = p(-L) = p_0,\ x \in [-L, L]$

2. Cavitation zone expanding
   $p(L) = p_0 \wedge p(x_{min}) = p_{min} \wedge \left.\frac{\partial p}{\partial x}\right|_{x_{min}} = 0,\ x \in [0, L]$

3. Cavitation zone contracting
   $p(L) = p_0 \wedge p(x_{cav}) = 0,\ x \in [0, L]$

Case 2 and 3 are solved in the interval $[0; L]$ and perfect symmetrical conditions in the pressure distribution and flow evaluations are assumed, as $L \ll R$. Figure 4.19 illustrates the three cases of film pressure distribution.

Typically, when forcing the valve plunger away from the seat, all three cases are covered in a 1-2-3-1 sequence. Initially, the film pressure equals p_0 (case 1) and then quickly drops below p_{min} and transitions to case 2, where the cavitation zone expands (flow out of cavitation zone). As time progresses, the height increases and at some instant of time the cavitation zone stops expanding, and starts refilling the cavitation zone (case 3). When the cavitation zone is completely refilled, the pressure distribution is again covered by case 1 at which point the stiction force typically decreases rapidly, releasing the valve plunger.

In the following sections the stiction force evaluation is presented for the three cases.

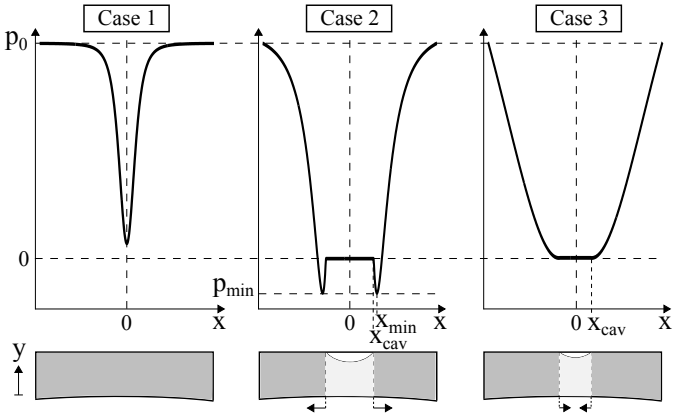

Figure 4.19: *Examples of pressure distribution for different cavitation cases and corresponding film zones. In case of cavitation, a central cavitated zone is present with $p = 0$, and the remaining (liquid) part of the film is solved using the Reynolds equation.*

Stiction force case 1

In case 1, the pressure distribution follows the expression given in equation (4.20), and the stiction force F_s is evaluated by calculating the mean pressure, $\overline{p}$:

$$\overline{p} = \frac{1}{2L}\int_{-L}^{L} p(x)dx \tag{4.21}$$

$$F_s = A_s(P - \overline{p}) \quad \text{with} \quad A_s = 8\pi RL\cos\gamma \tag{4.22}$$

The explicit expression for equation (4.21) may be seen in appendix A of paper [J]. A_s is the shadow area for the stiction pressure of both the inner and outer seat ring of the valve.

Stiction force case 2

For case 2 (and 3) the problem is solved for $x \in [0, L]$ and symmetrical conditions utilized to represent the negative coordinate part. Using $p(L) = p_0$ and $p(x_{min}) = p_{min}$ as conditions to determine C_1, C_2 in equation (4.17) gives a (lengthy) expression for the pressure distribution $p(x)$ for a given x_{min}. Using then the condition $\frac{\partial p}{\partial x}\big|_{x_{min}} = 0$, leads to:

$$x_{min} = \frac{\sqrt{yk}}{k}\tan a \tag{4.23}$$

where a is the root of an (also lengthy) implicit equation $f(a) = 0$. The root a is found numerically using a proper initial guess for the value of a. When entering case 2, $x_{min} = 0 \Rightarrow a = 0$ which is used as initial starting guess. Subsequent initial guesses are chosen as the root from the previous time step.

Knowing now x_{min}, the solution for the pressure distribution, $p(x)$, is given. The cavitation zone boundary x_{cav} is found numerically by imposing $p(x_{cav}) = 0$ with $x_{cav} \in [0, x_{min}]$. The mean pressure of case 2 is then given by:

$$\overline{p} = \frac{1}{L} \int_{x_{cav}}^{L} p(x) dx \tag{4.24}$$

and the resulting stiction force is found as in case 1. The lengthy explicit expressions for $p(x), \overline{p}$ and f are omitted in the thesis as they are several pages long, but these may easily be derived using computational algebra software (e.g. Maple) with the above provided guidelines. The explicit expression of $p(x)$ valid for case 2 and 3 when knowing x_{cav} is shown in appendix A of paper [J].

Stiction force case 3

The dynamics of cavitation zone expansion (case 2) is governed by the requirement that the minimum pressure cannot decrease below the tensile strength of the liquid, p_{min}. At some point in time, the film height h has increased such that expansion of the cavitation zone stops, succeeded by refilling of the cavitation zone (case 3). Using $p(L) = p_0$ and $p(x_{cav}) = 0$ as boundary conditions to equation (4.17) gives $p(x)$ (shown in appendix A, paper [J]), and the stiction force is evaluated as in case 2. The time of cavitation zone stagnation is identified in the simulation by comparing the current x_{cav} to the previous one from last time step.

The cavitation boundary dynamics in case 3 is determined by relating $\dot{x}_{cav}$ to the flow present at the cavitation boundary $Q(x_{cav})$, which is proportional to the pressure gradient $\frac{\partial p}{\partial x}$ (following equation (4.19)):

$$Q_{cav} = \overline{u}|_{x_{cav}} A_{cav} = -\frac{1}{12\eta} \frac{\partial p}{\partial x} h^2 \cdot A_{cav} \tag{4.25}$$

where $\frac{\partial p}{\partial x}$ and h is evaluated at x_{cav}, and A_{cav} is the flow area. The cavitation zone, with zero pressure inside, contains a mixture of vapor and liquid. The specific mixture characteristics are not known and it depends on the cavitation origin, which may be on the surfaces or somewhere in between. Some possible vapor/liquid mixtures are illustrated in figure 4.20.

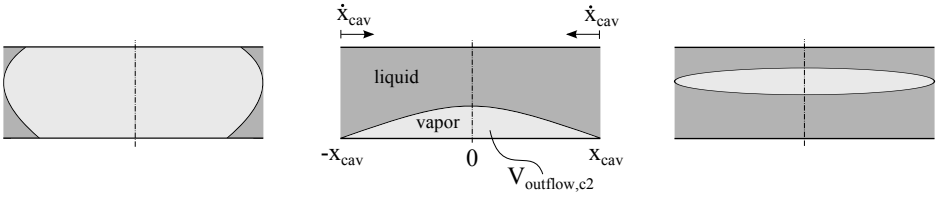

Figure 4.20: *Possible liquid/vapor mixtures in cavitation zone. The cavitation collapse speed is set to depend on the vapor/liquid ratio inside cavitation zone.*

During cavitation zone collapse, positive pressure gradient into the cavitation zone exist, leading to a positive flow in the direction of the cavitation zone, and a refilling of the

zone. Consider a liquid/vapor mixture as shown left in figure 4.20, compared to the mixture shown right. Different collapse speeds would result from a given zone boundary flow rate, all other parameters being equal. A refilling coefficient $\tau > 1$ is therefore defined which is determined from the vapor/liquid ratio inside the cavitated zone. That is,

$$\tau = \frac{V_{cav,c3}}{V_{\text{outflow,c2}}} = \frac{V_{cav,c3}}{\int_{T_{c2}}^{T_{c3}} Q_{cav} dt} \tag{4.26}$$

where $V_{cav,c3}$ is the total volume of the cavitation zone and $V_{\text{outflow,c2}}$ the outflow volume, both when entering case 3. T_{c2} and T_{c3} is the time for entering case 2 and 3 respectively.

The cavitation boundary velocity, $\dot{x}_{cav}$, and position is then calculated as:

$$\dot{x}_{cav} = \tau \frac{Q_{cav}}{A_{cav}} = -\frac{\tau}{12\eta} \frac{\partial p}{\partial x} h^2 \tag{4.27}$$

$$x_{cav} = \int_{T_{c3}}^{T_{c1}} \dot{x}_{cav} dt + x_{cav,c3} \tag{4.28}$$

Intake pressure

The fluid film outer boundary pressure p_0 is influenced by the local pressure drop present at the intake edges. Compared to the static surrounding pressure P, a lowered pressure is found at the film boundary depending on the intake velocity. Following Bernoulli's principle the boundary pressure in modeled as:

$$p_0 = P - \frac{1}{2} \lambda \rho \left(\overline{u}|_{x=L} \right)^2 \tag{4.29}$$

where ρ is the fluid density and λ a loss coefficient accounting for an increased pressure loss compared to an unrestricted flow, found experimentally in [89] to be approximately $\lambda = 2$.

Oil stiction results for example design geometry

By setting the surrounding pressure P to appropriate levels, both the HPV and the LPV stiction effect may be simulated using the above modeling approach by inserting the geometry values of the example valve design.

Figure 4.21 shows the resulting pressure distribution as function of time and the corresponding stiction force when driving the HPV away from the seat. The stiction force effectively counteracts the opening force (pressure and spring) up to ~ 8 kN, where after the valve is released with decaying friction force. As seen in figure 4.21, the valve is effectively held in the closed position due to the stiction effect until 0.2 ms has elapsed despite large forces trying to drive the plunger away.

The three cavitation cases are run through, starting with case 1 without a cavitation zone, followed quickly by an expanding cavitation zone (case 2). The cavitation zone then expands following the opening force until at some point the cavitation zone stops

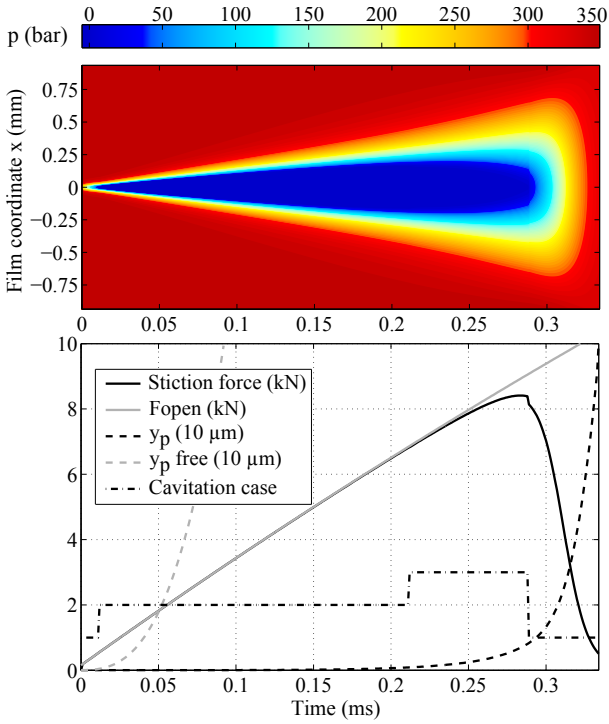

Figure 4.21: *Pressure distribution and corresponding stiction force when the HPV is forced open. Stiction time $T_{stic} = 0.24$ ms ($P = 350$ bar, $p_{min} = -5$ bar). The three pressure distribution cases are utilized in a 1-2-3-1 sequence after which the valve is released.*

expanding followed by a refilling of the cavitation zone (case 3). Finally case 1 is re-entered and the stiction force decays as the height increases.

Figure 4.22 shows a response corresponding to that of figure 4.21 for the LPV (notice the different pressure scales on the two graphs). As the surrounding pressure is much lower, the cavitation zone is expected to be large compared to the HPV response, which is also seen from the top of figure 4.22. The LPV oil film quickly cavitate when reaching $p = p_{min}$, followed by an expansion of the cavitation zone where the regions having negative pressure are clearly seen. The effect of negative pressure lasts for 0.1 ms, followed again by refilling of the cavitation zone and finally a return to case 1. A small stiction time below 0.1 ms is predicted for the LPV.

Study of uncertain parameters

The described stiction model exhibit two parameters which is difficult to estimate, namely the initial height and the tensile strength (maximum negative pressure). Clearly the initial height is in the μm range or even lower, where surface asperity plays a role

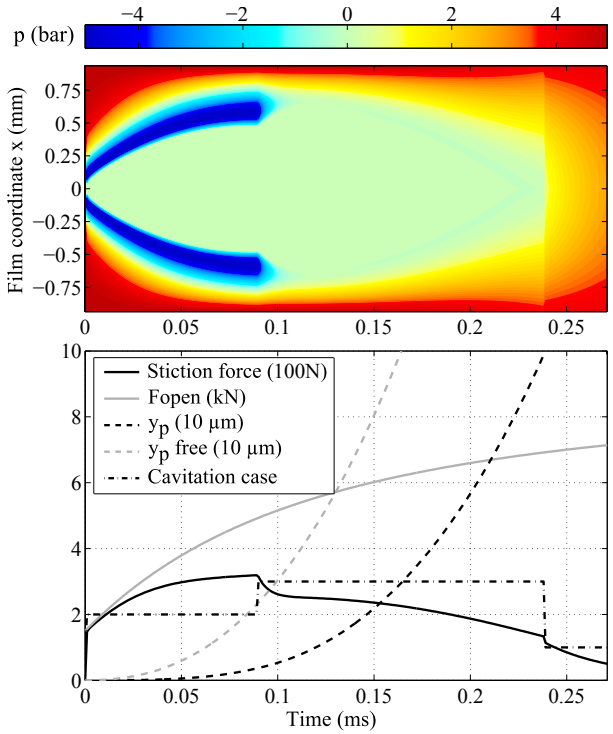

Figure 4.22: *Pressure distribution and stiction force when driving the LPV open. Stiction time $T_{stic} = 0.07$ ms, $P = 5$ bar and $p_{min} = 5$ bar. A large cavitation zone is developed, and the stiction force is quickly overcome by the opening force.*

and a uniform height is not present. In an ideal case with zero initial height, cavitation would be present instantly when applying an opening force. This singularity is, however, computational expensive to approach, as the simulation time steps needed goes towards zero. Figure 4.23 (left) shows the stiction time for the HPV and the LPV when the initial height is decreased. The LPV cavitate very quickly for initial heights of 1μm and below and no effect is thus seen in the stiction time (a 1μm initial height simulation is typically conducted in a couple of minutes). The HPV on the other hand needs very low initial heights to find the maximum stiction time, however an initial height of 0.1μm may be selected as a compromise between accuracy and computational cost.

The minimum pressure p_{min} is the other parameter hard to determine. For pure liquids, tensile strength exceeding 10 bar in dynamic loading has been observed [90]. However, the ability to withstand tension decreases when impurities are present as expected in hydraulic oil. The minimum pressure may therefore vary significantly during operation, and the simulation should represent worst case with respect to stiction effect. Figure 4.23 (right) shows the effect of lowering the minimum pressure on the stiction time for the LPV. Even though the stiction time is increased significantly, the stiction time is still relatively small for the shown range of minimum pressures. The HPV stiction is

only slightly influenced by changing p_{min}. A minimum pressure of -5 bar is chosen for the remaining results based on the experimental findings shown in [58].

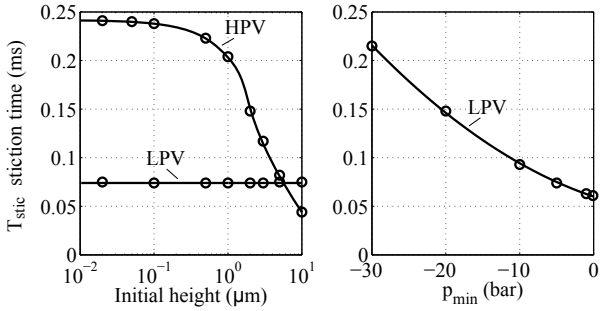

Figure 4.23: *Influence of initial height h_i on the stiction time (left). The LPV stiction is significantly influenced by p_{min} (right).*

One last aspect studied for the example design is related to the long term use of these valves. As described above, the stationary seat surfaces have a slight curvature, which improves the pressure distribution during valve loading, cf. design element C. Over time with many operation cycles the seat surface may loose this difference in curvature due to wear. In effect, this would give two parallel seat surfaces increasing the stiction effect. Simulations corresponding to the ones shown in figure 4.21 & 4.22 have been conducted using a very large value of R_{seat} to simulate two parallel surfaces. The illustration figures for these simulations may be seen in paper [J].

Compared to the response with curved seat surface, the cavitation zone is expanded and the stiction time is increased significantly for the HPV. The stiction time is more than doubled which retards valve movement and increases the chamber pressure overshoot. For the LPV, the stiction time is only slightly increased by 14%. However, the cavitation zone is enlarged and extends to nearly the whole film for some time period.

Stiction effect evaluation

The detailed behavior of a physical oil film is likely to differ from the simulated responses, as the tension in oil film and subsequent formation of the cavitation zone is subject to large uncertainties. However, the model provides a means to study the possible effect of liquid tension for annular seat valves.

In total, oil stiction effects for the example design does not greatly compromise the seat valve performance, but does contribute to considerable pressure transients for the chamber pressure, especially when forcing the HPV open. The HPV is found to be sensitive to changes in the seat curvature due to wear, unlike the LPV, which is not strongly influenced by the seat geometry curvature change.

Larger seat areas may easily increase the stiction effect to a degree where the DD pressure chamber response (overshoot due to HP valve stiction) is unacceptable. In such case, the

valve designer is forced to return to the topology selection and revise the design (element B in figure 4.1). For the example seat and plunger geometry, the stiction effect leads to a pressure chamber overshoot of approximately 50 bar at 350 bar manifold pressure, which is considered acceptable for proceeding with the example design.

However, this pressure overshoot is of concern in the design of the HP valve, and indicate that different valve geometries for the LPV and HPV may be beneficial. In such case, a HPV design utilizing for instance a steel plunger and zero seat angle may be selected for lowering the stiction effect, at the expense of a somewhat increased pressure loss.

4.6 Actuator interface dimensioning (element F)

With the seat and plunger geometry set, the interface between the valve plunger ring and the actuator needs to be dimensioned. Here a low mass and a low flow restriction are the main objectives, as the interface adds to the total moving mass of the valve and should allow for the oil to flow easily to the inner seat edge, cf. figure 4.2.

The interface is dimensioned to cope with the forces related to acceleration and deceleration of the armature and the plunger ring, and the actuator force itself. The actuator force and mass are known as part of the iterative design process indicated in the method overview in figure 4.1. The acceleration/deceleration forces may be estimated using the guidelines given in this section below. A relatively large strength margin is expected, and only a limited number of iterations are thus typically needed.

The largest acceleration of the plunger appears when forcing the HP valve open with a pressure chamber overshoot, and largest deceleration appears at the corresponding HPV opening end stop. Knowing the piston displacement, valve geometry and stiction effect, a simulation of the pressure chamber response in the event of opening the HP valve may be conducted, by estimating the total moving mass of the valve including the interface mass. This leads to an estimate of the maximum opening acceleration. Using the known mass of the actuator, the interface may then be dimensioned to transfer the needed force during this opening acceleration.

For the example valve design, the deceleration occurring as the HP valve hits the end stop dominates the interface dimensioning. Here relatively large velocity is present, after being shot open by the chamber pressure exceeding the manifold pressure. The impact velocity may be conservatively estimated by use of a dynamic valve simulation, where damping forces are neglected. Considering the ring part of the plunger to be the mass to be braked, and the interface some linear elastic member, the maximum braking force F_{br} may be calculated by virtue of energy conservation as:

$$F_{br} = k_i \Delta l \quad \text{and} \quad E_{pot} = E_{kin} \Rightarrow \frac{1}{2} k_i \Delta l^2 = \frac{1}{2} m_{br} v_{imp}^2 \Downarrow \tag{4.30}$$

$$F_{br} = v_{imp} \sqrt{m_{br} k_i} \tag{4.31}$$

where k_i is the stiffness of the interface, m_{br} the mass to be braked (plunger seat ring) and v_{imp} the simulated impact velocity. This maximum braking force may then be used to dimension the interface.

4.7 Virtual mass and damping effect model (element G)

This design method element seeks to estimate the fluid forces which oppose the plunger as it is moved rapidly through the surrounding oil, in order to include this effect later in the actuator optimization in element I. As previously discussed, valve closings are conducted at times where the cylinder piston is close to the top or bottom position, where the flow rates are relatively small. The forces acting on the valve plunger is a combination of the actuator force and fluid forces, where the fluid forces includes all forces related to the surrounding fluid.

The fluid forces resulting from flow through the valve gives a contribution acting to close the valve, with a force level depending on the flow rate at the time of closing. In addition to the flow induced forces, opposing fluid forces are present as a result of moving the submerged valve plunger rapidly in viscous oil, which significantly affect the movement of the plunger.

A combined model including all fluid forces are not easily developed at this stage of the design, and the flow induced forces are neglected as a conservative assumption with respect to the valve closing time. The virtual mass and damping effect model developed here thus considers the valve to be submerged in stationary oil, which is expected to reasonably represent the valve operation during closing, and a more accurate fluid model may be developed at a later design stage to test the valve design resulting from the design method.

As the seat and plunger geometry and is known at this design stage, a lumped parameter model of the opposing fluid forces may be developed for inclusion in the actuator optimization in element I. This lumped parameter model is determined using 2D transient CFD simulation. The CFD simulation is conducted using Ansys Fluent, where dynamic re-meshing and layering zones are utilized to account for the plunger movement, similar to the model previously used in section 3.4 on page 56 (simplified to 2D, though). The fluid forces acting on the plunger are calculated for each time step of the simulation and coupled to the plunger movement.

A simulated valve response when applying a constant 500 N closing force is given in figure 4.24, including the fluid forces resulting from this plunger movement.

As seen in figure 4.24, fluid forces are present even at zero velocity due to acceleration of the surrounding fluid, and a large increase in fluid forces appear when nearing the closed position. A lumped parameter model in the following form is utilized:

$$F_f = m_v \ddot{y}_p + \left(B + k_1 + k_2 e^{-\frac{l_s - y_p}{k_3}} + k_4 e^{-\frac{l_s - y_p}{k_5}} \right) \dot{y}_p + D \dot{y}_p^2 \tag{4.32}$$

where m_v denotes the virtual mass added due to acceleration of the surrounding fluid, B viscous shearing coefficient, D the drag coefficient and $k_1 \cdot \cdot k_5$ additional friction coefficients.

A series of transient CFD simulations with different characteristic actuator force levels (200-800 N), giving a number of responses similar to figure 4.24, have been conducted to obtain a basis for determining the geometry dependent parameters in equation (4.32). The parameter values for the lumped parameter model are then found using a global optimization method (Genetic Algorithm) with objective to minimize the difference between the CFD and corresponding responses using equation (4.32). Figure 4.24 shows the resulting lumped parameter model response of the opposing fluid forces using the found parameters.

Contrary to the transient CFD, the analytic model may be quickly evaluated and is thus suited for the actuator optimization in element I.

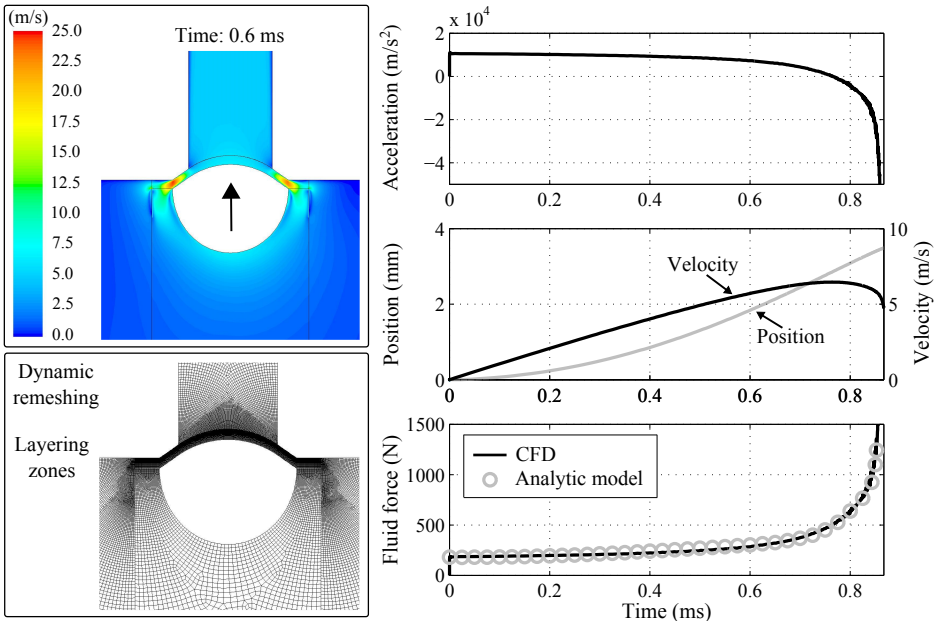

Figure 4.24: *Valve position, velocity, acceleration and opposing fluid forces corresponding to valve closing with a constant* 500 *N actuator force. Simulated using a transient CFD model, and a large increase in fluid force is present near the valve closed position.*

4.8 Heat dissipation model (element H)

This method element treats the valve actuator heating, in order to determine the allowable actuator power as input for the actuator optimization. Excessive heating at the coil and permanent magnet should be avoided. Generally, an increased actuator power is assumed to decrease the valve switching time, which in turn leads to lower valve flow losses by decreasing the amount of flow conducted with semi-opened valves, as previously discussed. How much actuator power should then be invested to decrease the valve flow loss?

As shown in figure 4.1, this method element is part of an iteration loop, as the actuator heating problem depends on the actuator dimensions, which is not known prior to the actuator optimization. Some initial guess on a feasible allowable power level may be obtained using rough estimations, and an actuator optimization (element I), with the selected power level, then gives the resulting valve switching time. A few iterations with different power levels then lead to knowledge of the obtained valve switching time for the invested actuator power. The method described in section 3.1 may then be used to give estimates on the relation between flow loss and invested actuator power. The method for evaluating the actuator heating and the considerations for the example design is given below.

The actuator heat dissipation is slow compared to the individual actuator cycles, and the temperature change for each actuator cycle is relatively small. The mean actuator power is therefore used as input to a steady FEA heat analysis, where the resulting temperature in the coil region is the parameter of interest. The heat FEA is solved by specifying the temperature of the surrounding steel to be 40^{o}C at a distance of 100 mm, to roughly simulate the valve assembly inserted in a motor block.

A maximum temperature of approximately 100^{o}C is specified based on the coil wire insulation and permanent magnet rating. Figure 4.25 (left) show the coil temperature as function of the mean actuator dissipated power. The heat FEA temperature field corresponding to 250 W actuator power is also shown in figure 4.25.

No oil movement in the coil region is included in the heat analysis illustrated in figure 4.25. Including oil movement in the analysis would improve the heat exchange rate, lowering the maximum coil temperature. However, as no pressure driven flow is present along the coil, this effect is expected to be small and not included in the analysis, leading to a conservative temperature estimate.

Calculating the additional power loss compared to zero switching time (based on the data in figure 3.4, for the example valve design), gives the values shown in table 4.3. As the heat limit for the example design actuator is 250 W giving a total actuator power of 500 W for the two valves. This indicates that the actuator power realizable within the thermal limits is relatively small compared to the valve flow loss resulting from a decreased switching time, at least for switching times of 3 ms and above.

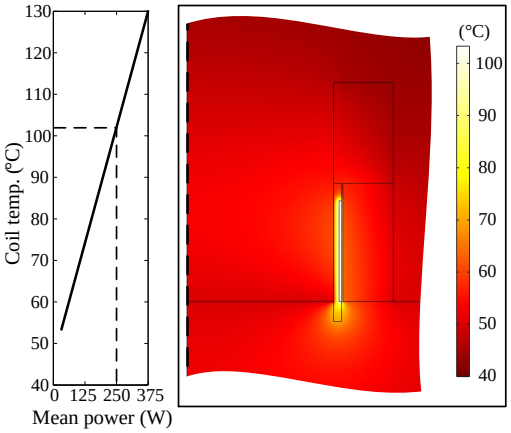

Figure 4.25: *Coil temperature as function of mean power dissipation (left) and temperature field resulting from a 250 W heat dissipation (right)*

Table 4.3: *Additional flow power loss compared to zero switching time for the example design.*

0 ms	1 ms	2 ms	3 ms	4 ms	5 ms
0 W	39 W	367 W	1472 W	3872 W	7704 W

For the example design, the actuator is optimized with basis is the maximum power level acceptable with respect to heating, and a switching time of approximately 1 ms is obtained after optimizing the actuator (design element I). Some de-rating may be favorable with respect to the total efficiency, which may be studied by running the actuator optimizations with different power levels.

4.9 Actuator optimization (element I)

This design method element optimizes the valve actuator to obtain minimum switching time, with basis in the preceding method elements. This is the last design step of the valve, which is followed by an efficiency evaluation of the completed valve design (element A2), as shown in figure 4.1.

To optimize with respects to the valve switching time, a dynamic model of the valve movement is coupled to the electro-magnetic actuator model. In addition to the electromagnetic actuator force F_{em}, the plunger is affected by the spring force and fluid restrictive forces F_f. That is,

$$F_{em} - k_s(y_p + y_i) - F_f = m\ddot{y}_p \tag{4.33}$$

where m denotes the moving mass, k_s the spring constant, y_i the spring preload, y_p the plunger position and $\ddot{y}_p$ the plunger acceleration. The springs are dimensioned such that the spring force in open position is sufficient to keep the valves open during piston displacement flow. The maximum flow force during displacement flow is determined using CFD analysis with an appropriate overhead to account for model uncertainties.

The fluid restrictive forces resulting from valve movement are modeled using equation (4.32) from design element G. As the viscous friction from moving the actuator itself is not included in (4.32), it is separately calculated from the shearing friction present in the bobbin region using (4.34), and in turn added to B in (4.32).

$$B_{act} = \nu\rho\frac{A_{act}}{w} \tag{4.34}$$

where ν is the kinematic oil viscosity, ρ the oil density, A_{act} the shearing area of the bobbin and w the shearing layer thickness. Relatively loose mechanical guidance is used for the fast switching DD valves, and the force resulting from B_{act} is typically small compared to the other forces acting during valve switching. Some rough estimate for A_{act} may therefore be applied in the initial iteration of the actuator optimization.

Specifications and parameters constituting the framework of the actuator optimization are given in table 4.4.

Table 4.4: *Parameters for actuator optimization in the design example.*

Maximum continuous power	250 W
Plunger diameter	60 mm
Moving mass (excl. coil)	25 g
Stroke length l_s	3.5 mm
Opening spring force	150 N
Max operation frequency	25 Hz
Virtual mass m_v	17 g
ν, ρ, t	$46 \cdot 10^{-6}$ m^2/s, 870 kg/m^3, 0.1 mm
(k_1, k_2, k_3)	$(0.002, 225, 3.952 \cdot 10^{-4})$ Ns/m
(k_4, k_5), D	$(1968, 2.965 \cdot 10^{-5})$ Ns/m, 4.935 Ns^2/m^2

Actuator system model

Transient electro-magnetic FEA is utilized for simulating the time dependent response of the actuator force F_{em}, considering a moving armature coupled to the valve movement. Three design variables, namely the wire diameter d, coil width b and coil height h define the actuator geometry, following the selected moving coil actuator topology. The actuator geometry including its parameters is given in figure 4.26. The outer steel flux path is dimensioned such that no magnetic saturation occur, and the permanent magnet height is determined from the coil height and valve stroke length (the moving coil does not leave the region with high flux density).

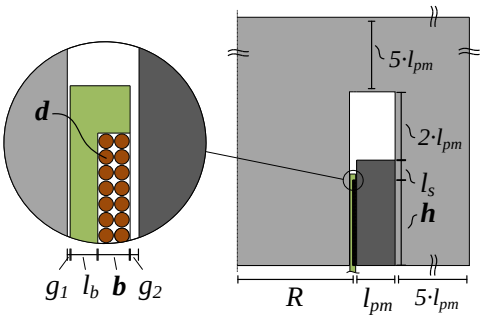

Par.	(mm)
g_1	0.1
l_b	1
g_2	0.25
R	30
l_{pm}	10
l_s	3.5

Figure 4.26: *Axi-symmetric actuator geometry used for optimization with three design variables (h,d,b) and a number of fixed parameters set on basis of the application and manufacturing considerations.*

The permanent magnet thickness l_{pm} directly influences the magnetic field density in the coil region, and should be selected large enough for the inner yoke material to saturate. A permanent magnet thickness $l_{pm} = 10$ mm is selected for the design example, ensuring inner yoke saturation for the actuator design with reasonable space requirements.

For fast valve switching, the current (and thus the actuator force) should rise quickly until the peak rated current level is reached, followed by a current hold until valve switching is conducted. Therefore, when modeling the valve response, a voltage step is initially applied, until the current reaches a specified maximum, where after a current source is applied until valve end position is reached ($y_p = l_s$), resulting in a current response similar to that obtained using a high frequency PWM voltage source with current control.

Electromagnetic model

Modeling of the electromagnetic circuit is done by solving the magnetic vector diffusion equation with appropriate boundary conditions for the domain shown in figure 4.26 (including a surrounding air domain, not shown in the figure). To model the applied voltage step followed by a current hold, co-simulation of an external circuit coupled to the field solution is utilized. The simulation is conducted using the software package COMSOL Multiphysics 4.3b AC/DC module, with an automatic setup through Matlab. Further details on the solver and utilized material properties may be seen in paper [K].

The problem domain is discretized into a number of elements with a mesh topology that allows the coil region to be moved without compromising the mesh quality. An example of the domain mesh is shown in figure 4.27. As seen, the mesh density is increased in the coil region, and the moving coil region together with two deforming regions are non-conformal (that is, the nodes does not match). These non-conformal mesh parts are combined using interpolating mesh interfaces. The deforming/moving regions are meshed using a structured quad mesh, facilitating non-complicated mesh deformation and avoiding the need for regeneration of domain mesh during time domain simulation.

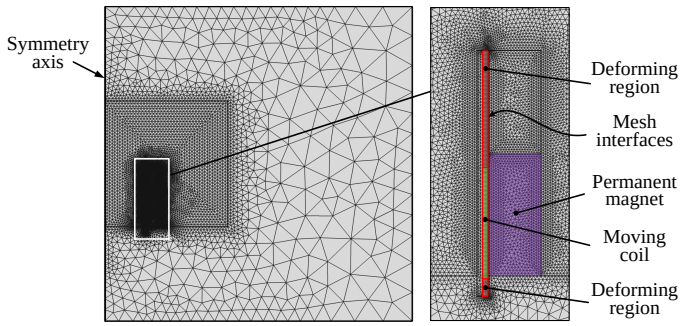

Figure 4.27: *Example of a problem domain mesh with insulation boundaries, symmetry axis and an increased mesh density near the coil region. The moving/deforming regions are non-conformal with the remaining mesh and mesh interfaces (ideally magnetic conducting) are used to combine the mesh regions.*

Each domain mesh consists of 15-30k elements, depending on the design point (h,d,b) in the optimization algorithm. The initial condition for the transient simulation is set to be the static solution with zero coil current, representing the static field generated by the permanent magnets.

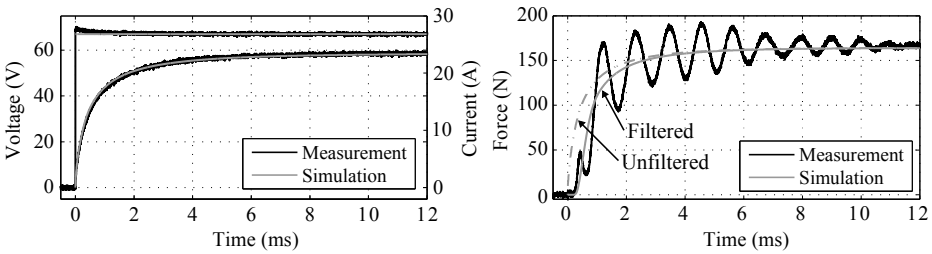

Figure 4.28: *Measured and simulated prototype actuator responses to a voltage step. The actuator coil was kept in a fixed position.*

The above actuator model has been compared to corresponding experimental measurements conducted on an actuator prototype, with the coil held in fixed positions. This prototype is similar to the example design actuator, and was manufactured and tested as a pre-study to the actuator optimization given in this section. Good agreement between the experiments and the simulations was found, as shown in figure 4.28. Oscillations are present in the measured force response, but the characteristics correspond well to the simulated response (when accounting for the filtering effect of the force gauge measurement setup). Further details on the actuator prototype and the experimental measurements may be found in paper [K].

Optimization

To perform the optimization of the moving coil actuator, the three design variables (coil height h, coil width b and wire diameter d) must be linked to the other dependent design parameters. Given a set (h,b,d), the number of coil turns n is determined as:

$$n = \text{round}\left(\frac{\xi A_{coil}}{\frac{\pi}{4}d^2}\right) \quad \text{with} \quad A_{coil} = hb \tag{4.35}$$

where $\xi = \pi/4$ is the assumed coil fill factor. The moving mass m is then given as:

$$m = V_{wire}\rho_c + m_0 \tag{4.36}$$

$$\text{where} \quad V_{wire} = L_{wire}A_{wire} = 2\pi R_{coil} n \frac{\pi}{4} d^2$$

here, R_{coil} is the mean coil radius, $m_0 = 25g$ the moving mass excluding the coil and ρ_c the density of copper. The coil region shearing friction B is found using (4.34), with $A_{act} = 2\pi(h + l_s)R_{coil}$.

The power level is available as input for the optimization, however the voltage-current ratio is not known. That is, the maximum value of coil voltage V_{max} and coil current I_{max} is to be specified. The allowable actuator power is linked directly to the voltage-current product of the power supply, whereby maximum current and voltage is assumed during valve switching. This is a conservative assumption with respect to the coil temperature, as the actual power will be somewhat lower than this maximum.

Each valve actuator is active for approximately 2.5 % of the complete cycle (1ms/40ms), giving a maximum allowable power, during switching, of 10 kW while maintaining the average power at 250 W. This power supply power limit is shown in figure 4.29.

Each point on the limiting line represents the same supply power, but which point should then be selected for optimum actuator performance? The grey dots in figure 4.29 represent widely available and cheap MOSFETs covering both the low-voltage-high-current, high-voltage-low-current and middle areas of figure 4.29. To analyze the voltage-current ratio's influence on the valve switching time, the moving coil actuator geometry is optimized for three reference power supplies in the example design, shown by the points A, B and C in figure 4.29. From an energy consideration point of view, the switching time may be expected to be independent of the specific voltage-current ratio, as equal actuator energy is available. However, other factors related to the coil and valve construction may come into play.

The moving coil design optimization is conducted using a brute force strategy, by which the whole design space is covered by a grid. This computational expensive strategy is chosen as it gives an idea of the overall tendencies and sensitivity instead of just the optimum design. To ensure feasible coil dimensions, which may be wound while obtaining the assumed filling factor $\xi = \pi/4$, only integer multiples of the wire diameter is considered for the coil width. That is, $b = Nd$, where N is the number of wire layers in the coil.

The main objective for the actuator optimization is to minimize the switching time, in order to obtain high efficiency of the DD machine. In case of several design points

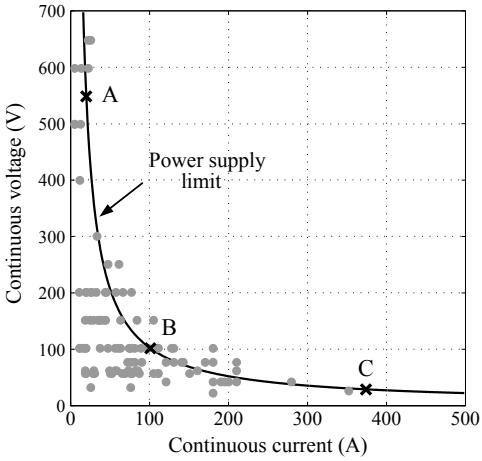

Figure 4.29: *Power supply limit as function of the maximum current and voltage levels. Commonly available MOSFETs indicated with grey dots.*

exhibiting similar low switching times, two secondary objectives are considered: One objective is a desire to obtain a low moving mass, as this reduces the kinetic energy and thus the material stresses at valve impact. Second is a large coil height, as a larger coil height improves the mechanical guidance of the valve and increases the heat dissipation area of the coil.

Results

Figure 4.30 shows contours of the valve switching time T_s for various wire diameters d and coil heights h for A, B and C type of power supply and with different number of coil layers N. The six top contours represent power supply type A with coil layers ranging from one to six, showing regions of low switching time and similar for supply type B and C in the three middle and bottom contours respectively. Increasing the number of layers N generally shifts the optimum region towards lower coil heights and increasing wire diameter, as seen in figure 4.30.

For supply type A, near minimum switching times in the range 1.0-1.05 ms are found for N equal to 2, 3 and 4, whereas supply type B and C exhibit lowest switching time with a single coil wire layer. While the number of layers and coil dimensions differs for each supply type, the minimum switching time is nearly unaffected by the voltage-current ratio, showing that a moving coil actuator design utilizing the supply power in an optimal way exist for each of the supply types A, B and C. Presumably this may be said generally for all voltage-current ratios, such that the minimum switching time is a function only of the available power level.

In order to select the most suitable supply type A, B or C, attention is directed to the coil moving mass. A low moving mass is desired to decrease the kinetic energy, and in figure 4.30 lower coil mass is found for low $b \cdot h$ products, where $b = N\,d$. Lowest moving

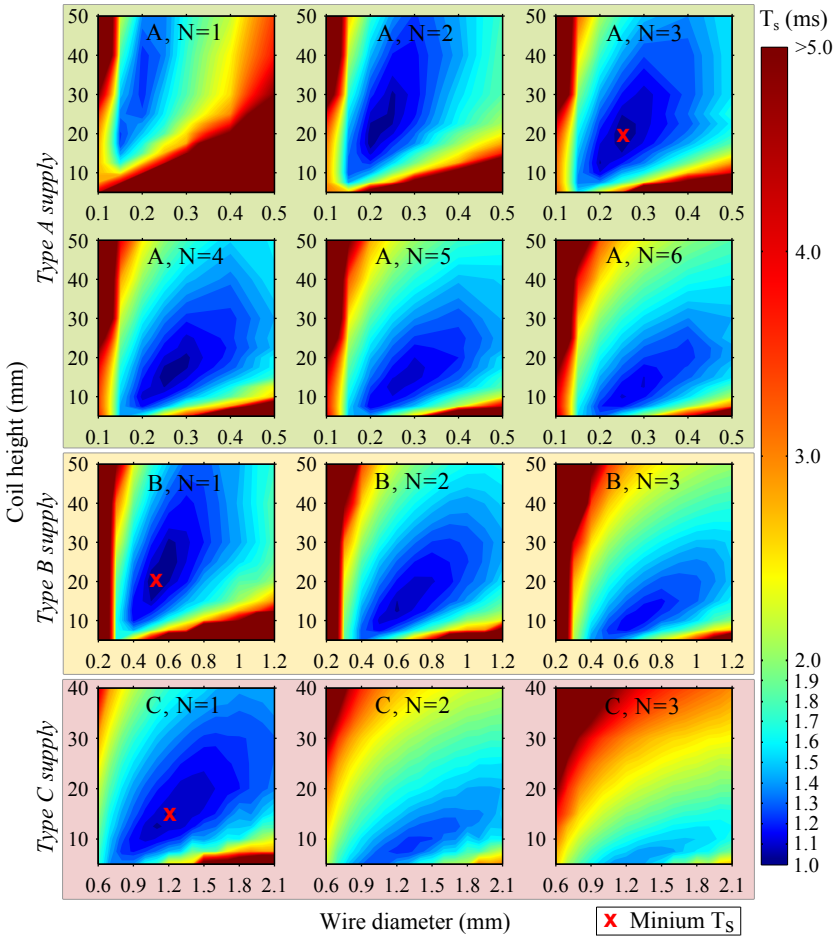

Figure 4.30: *Contours of valve switching time T_s using supply type A,B and C with various wire diameters and coil heights when considering different numbers of coil layers N. Minimum switching time is nearly independent of the supply type, minimum T_s is* 1.02 *(A),* 1.02 *(B) and* 1.05 *(C) ms.*

mass while maintaining a switching time close to minimum is obtained using supply A with two coil layers (point $h = 20$ mm and $d = 0.2$ mm). In addition, this design point has the practical benefit of having two coil layers, whereby the coil wire input and output may be at the same location. Table 4.5 show specifications of the chosen optimum design for the design example. The relatively high voltage level may be a concern regarding application safety.

Table 4.5: *Specifications of the selected optimum actuator design.*

Power supply	550V/18.2A	Switch time T_s	1.04 ms
Coil resistance	26.8 Ω	Coil turns n	200
Coil height h	20 mm	Coil width b	0.4 mm
Wire diameter d	0.2 mm	Coil layers N	2
Moving mass m	36 g	Coil mass	11 g

Figure 4.31 shows the magnetic flux density and current density of the optimum moving coil actuator at selected time steps. Initially the magnetic circuit is driven solely by the permanent magnet leading to the field shown in the top left part of figure 4.31. In this static situation, no angular currents are present (top right field).

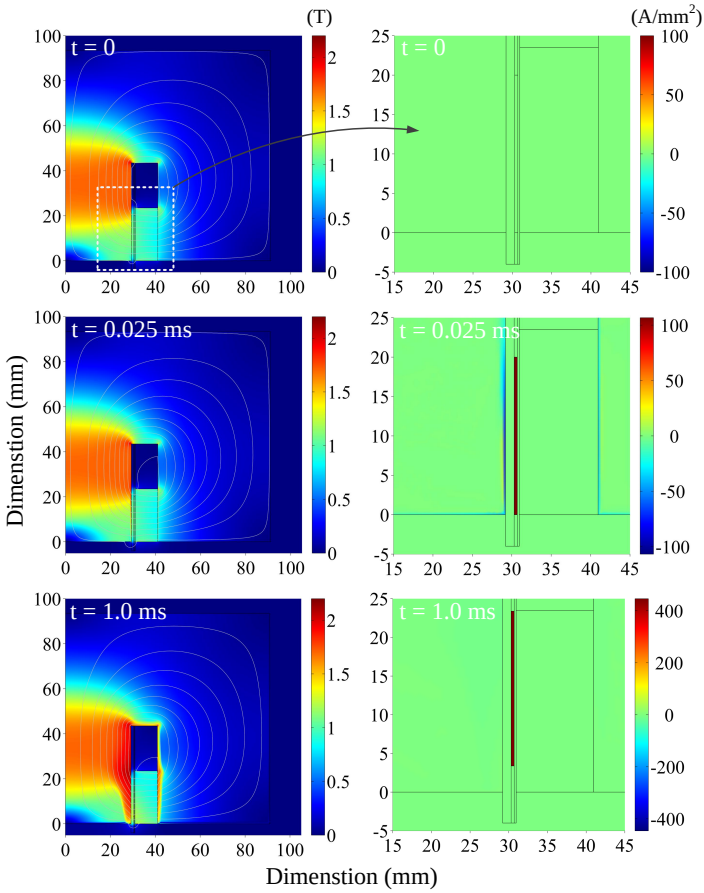

Figure 4.31: *Magnetic flux density (left) and current density (right) distribution of the optimum moving coil actuator at selected time instants.*

Shortly after applying the voltage step (t = 0.025 ms), the coil current is building up and eddy currents opposing the change in magnetic flux generated by the coil current are present (middle right part of figure 4.31), acting as a shorted turn in the flux path material, effectively limiting the apparent self-inductance of the coil.

At the end position (t = 1.0 ms), the coil has traveled to the opposite end of the permanent magnet and exhibits a current density of approximately 400 A/mm^2. As seen in figure 4.31 (bottom, left) an increase in magnetic flux density is visible at the end position, however, the magnetic flux density distribution is dominated by the field resulting from the permanent magnet.

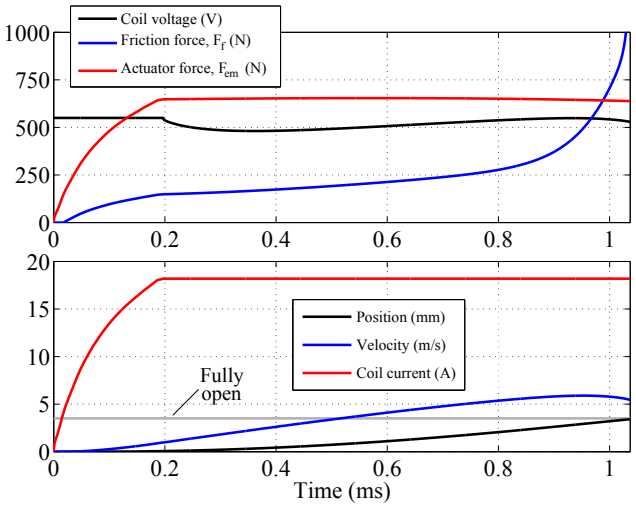

Figure 4.32: *Dynamic valve response using the optimum moving coil actuator. The voltage required to maintain the current level when latched (above* 0.7 *ms) is only slightly less than the applied voltage step level.*

The dynamic response of the optimum actuator design is shown figure 4.32. An adaptive time stepping scheme has been utilized to lower the computational cost. As seen in figure 4.32, the valve switching time is T_s =1.04 ms, in which period the valve travels 3.5 mm. Resulting from the voltage step, current starts to rise op to the maximum level specified, and this level is subsequently maintained. It is seen that, for the optimum design, the voltage required to maintain the maximum current is relatively close to the initial voltage level. This ensures high energy input leading to a low switching time. The resulting force is initially zero in a small period of time, as the opposing springs must be overcome before initiating motion.

Simulation time for the above actuator analyses vary significantly depending on the design point, but one simulation is typically conducted within 3-15 minutes.

4.10 Efficiency with actuator power loss (element A2)

The final step of the design method is to check the DD motor efficiency with the optimized valve design, including both flow and actuator power loss, against the target efficiency, cf. figure 4.1 on page 69. The actuator energy input during switching is known from the optimization step in I, which may be combined with the efficiency simulation given in step A.

For the flow coefficient and the obtained switching time the DD machine efficiency without actuator power loss is 99.7/98.9 % for full displacement and 20 % displacement respectively. Including the actuator power loss, the corresponding efficiencies are 99.3/98.7 %. The effect of the actuator loss is smaller at 20 % displacement, as the actuators are only activated once every fifth cycle and no actuator losses are present in the remaining cycles. The target efficiency of 99 % at 20 % displacement is not completely achieved, but the 98.7 % efficiency is accepted for the valve design example.

4.11 Example valve design and LPM analysis of motor

A Lumped Parameter Model (LPM) motoring response simulation, using the optimized valve design, is here conducted to evaluate the motor efficiency more accurately and evaluate the dynamic response. This simulation is performed with basis in the LPM method previously described in section 3.5 on page 64.

As input to the LPM, the flow and force characteristics of the designed valve is evaluated using steady CFD simulations, cf. section 3.5. Valve stiction effects are included (from section 4.5), and the actuator transient response is included using a first order system approximation, such that the response is similar to the response shown in figure 4.32. In addition, the valve movement dynamics include the virtual mass and damping effects, cf. section 4.7. A dead volume of 200 cc is assumed, similar to the design shown in figure 3.12 on page 55. The resulting dynamic response using this LPM is shown in figure 4.33.

Some key figures from the response are given in table 4.6. As seen in figure 4.33, a pressure overshoot of approximately 50 bar is present at the time of HPV opening, due to the oil stiction effect. The valve pressure difference during displacement flow is very low, and the fast switching valves enables the LPV and HPV to be closed relatively close to the piston top dead center and bottom dead center respectively.

The obtained efficiency is given in table 4.6. This efficiency is close to the estimated efficiency, and the slightly higher efficiency may be caused by the decreased valve opening time (0.8 vs. 1.0 ms). These asymmetric valve switching times makes the LPM differ from the efficiency estimation model (section 3.1), where equal valve opening and closing times are assumed.

The response shown in figure 4.33 is considered promising, and a prototype of the designed valve has been constructed and manufactured to test the performance compared to the simulation predictions.

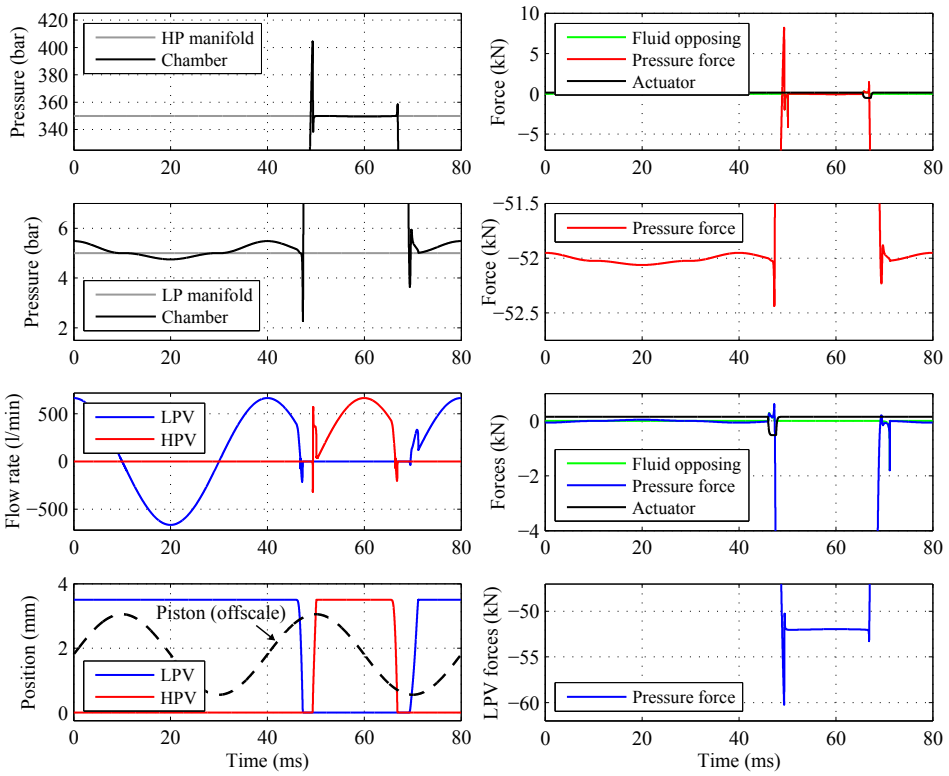

Figure 4.33: *LPM response of DD motor using the optimized valve design example. One motoring cycle followed by a motoring cycle shown.*

Table 4.6: *LPM model response specifications corresponding to figure 4.33.*

Cycle time	40 ms
Min/max avg. chamber pressure (idling)	4.7/5.5 bar
Min/max avg. chamber pressure (motoring)	2.3/404 bar
Max actuator force (net closing)	520 N
Opening time HPV/LPV	0.8/0.8 ms
Closing time HPV/LPV	1.0/1.0 ms
Efficiency 100%/20% displacement	99.4/98.8 %
Utilized displacement	93.7%

Chapter 5

Experimental Results on Valve Prototype

In this chapter the valve prototype is presented and experimental measurements on the valve actuator are compared to simulations. Further measurements are needed to study some remaining aspects of the valve performance. Manufacturing experiences are discussed to highlight some of the challenges found in manufacturing the valve design from the previous chapter.

Figure 5.1 show the valve prototype setups. A fixed position setup is utilized for testing the valve actuator, where a bobbin fixture replaces the valve plunger ring, as shown to the right. Another setup enables testing of the dynamic valve movement and sealing properties, as shown to the left. The valve plunger ring is manufactured in reinforced PEEK (black color), while the actuator interface and coil bobbin is made of pure PEEK (light brown color). A number of discrete permanent magnets are glued to form the radially magnetized annular magnet.

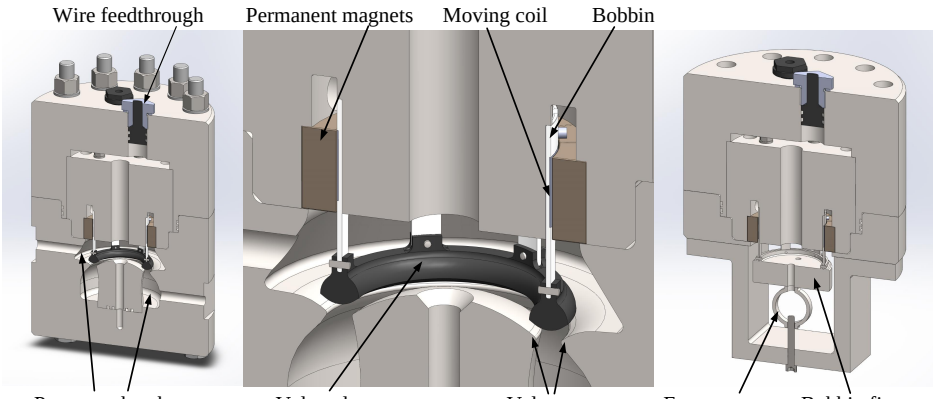

Figure 5.1: *Valve prototype setups. Left, a setup for testing valve movement and sealing at different pressure levels. Right, fixed position actuator test setup.*

The valve plunger CAD model and a picture of the manufactured plunger are shown in figure 5.2. The coil has been hand wound and glued to the bobbin. The plunger was initially constructed to be manufactured in one piece of reinforced PEEK, but supplier limitations caused a design change into two separate parts assembled with pins, as shown in figure 5.2.

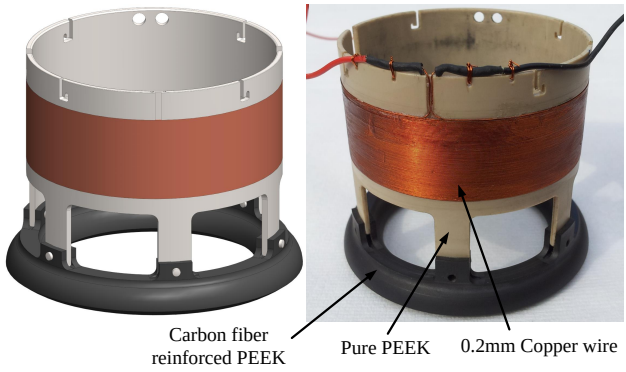

Figure 5.2: *CAD model and picture of the valve plunger. The assembly pins are not inserted in the picture to the right.*

The glued annular permanent magnet with the moving coil actuator and bobbin fixture is shown to the left of figure 5.3. This picture is upside down compared to the illustration to the right in figure 5.1. The 16 permanent magnet shells have been custom made for the prototype and are made of neodymium, type N48H (rated temperature 120°C). A complete view of the fixed position setup including control electronics is shown to the right in figure 5.3. The plunger position is adjustable within the valve stroke length, and a force gauge is used to measure the generated actuator force.

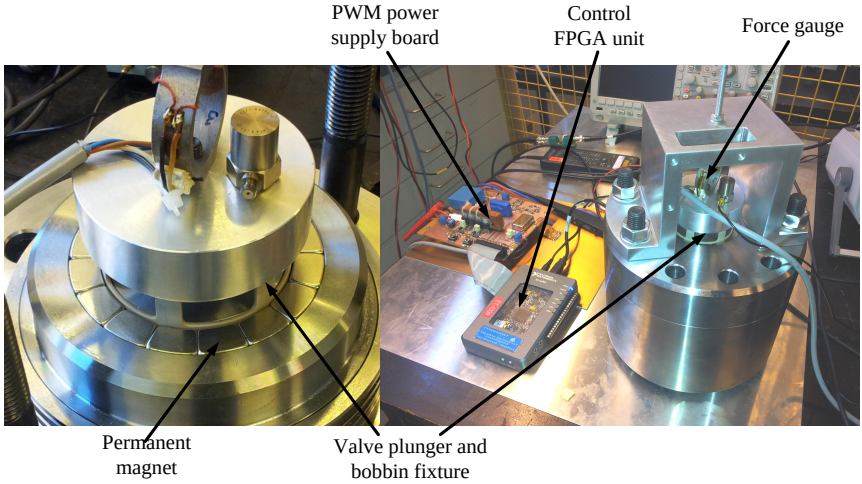

Figure 5.3: *Valve actuator close-up picture (left), and the fixed position test setup including control electronics (right).*

A custom designed MOSFET based H-bridge board with current measurement circuit have been developed and made by the author in order to have full controllability of the applied PWM voltage while supporting the high peak power at 550 V and 18 A. Large DC-link capacitors (5 mF) are used to maintain the supply voltage level reasonable constant. The moving coil actuator constitutes a low inductance load, and a relatively high PWM carrier frequency of 50 kHz is thus utilized to keep the current ripple low. The current measurement is conducted at the H-bridge output and transferred using digital signals to reduce noise effects. An FPGA control unit is used for the PWM and current control, and the data acquisition is performed using an oscilloscope. The strain gauge based force meter is connected to an external amplifier unit in order to obtain useable measurement signals. This strain gauge amplifier exhibits signal delay and a relatively low frequency filter (1000 Hz), which has been characterized in a previous setup. A model of this amplifier is used for the measurement and actuator simulation comparisons.

For the prototype plunger, the coil glue was applied manually. It was found difficult to avoid some excess glue, and the coil air gap was therefore increased by 0.1 mm to account for the increase in coil width. In addition, a more better solution for the coil wire connections will be implemented in future prototype versions.

The total weight of the plunger in the valve prototype is 50 g, with an increase of 14 g compared to the reference design mainly because of the design using two separate parts using pins for assembly.

5.1 Moving coil actuator verification

The electro-magnetic FEA, used for optimizing the actuator circuit in section 4.9, is here compared to experimental measurements on the valve prototype. Specifically, the static and transient actuator responses are studied and compared to the simulated responses.

Among other material properties, the relation between magnetic field strength, H, and magnetic flux density, B, is used as input for the FEA. To facilitate good analysis accuracy, the BH-relation for the construction steel and the permanent magnets is investigated experimentally before conducting the actuator simulation.

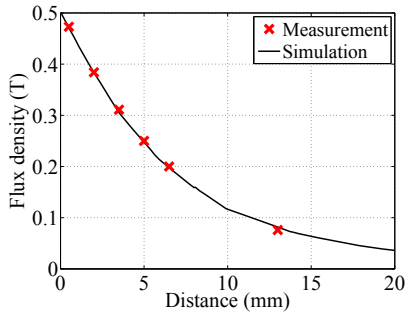

Figure 5.4: *Measured and simulated flux density as a function of distance for a magnet shell piece surrounded by non-magnetic material.*

The permanent magnets are expected to operate well above the coercive field strength, and are therefore modeled as $B = \mu_r \mu(H + M)$ where M is a constant magnetization strength. The magnetization M is determined experimentally by measuring the magnetic flux density of a single permanent magnet shell with a gauss-meter in some well-defined points, when surrounded by non-magnetic materials, and comparing with a corresponding steady spatial FEA. The result is shown in figure 5.4, where a magnetization of 1070 kA/m is found is the radial direction.

The steel path is fabricated using typical low carbon construction steel, where the magnetization curve is not specified. A toroid with a core of the specific steel material is fabricated and used to experimentally measure the magnetization curve. This toroid is fitting with a primary and a secondary winding, and a time varying current is conducted in the primary winding. This current and the induced voltage in the secondary winding are measured giving information of the field strength and corresponding magnetic flux in the steel material. That is,

$$\Phi N_s = \int_0^t v_s(\tau) d\tau \quad \text{where} \quad B = \frac{\Phi}{A_t} \tag{5.1}$$

and

$$H = \frac{N_p}{l_{eq}} i_p \quad \text{with} \quad l_{eq} = 2\pi \left(\frac{\ln\left(\frac{R_o}{R_i}\right)}{\frac{1}{R_i} - \frac{1}{R_o}} \right) \tag{5.2}$$

where Φ is the magnetic flux linking each turn, v_s the induced voltage in the secondary winding, i_p the primary winding current, R_i and R_o the inner and outer toroid radius, N_p and N_s the primary and secondary number of turns and A_t the cross sectional area of the toroid core.

Plotting the resulting magnetic flux densities, as function of the field strength for various primary current amplitudes lead to a number of hysteresis loops, as shown in figure 5.5. The initial magnetization curve used in the FEA is then given as the end-points of each hysteresis loop.

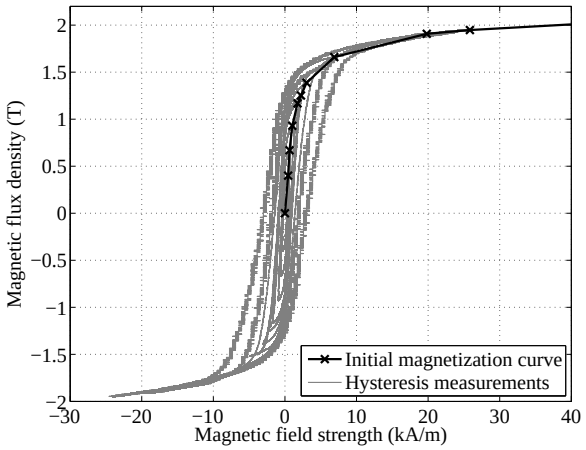

Figure 5.5: *Measured hysteresis magnetization curves and initial magnetization curve used as the steel material model in the actuator FEA.*

A typical value for the steel electrical conductivity is used, and the permanent magnet conductivity is set to zero as it is made up of discrete elements, cf. paper [L].

Steady current-force ratio comparison

Using feedback current control, a steady current and a corresponding steady actuator force is obtainable. By simulating the actuator with different levels of constant coil currents, a comparison as shown in figure 5.6 is found. A close to linear relation between coil current and actuator force is seen, as expected, and a good correspondence between the simulation model and the measurements is seen. Depending on the current direction, the magnetic flux generated by the permanent magnets is either strengthened or weakened, which makes the force characteristic deviate from a perfect linear relationship in the steady operation case. This effect, however, is seen to be limited for the valve actuator prototype.

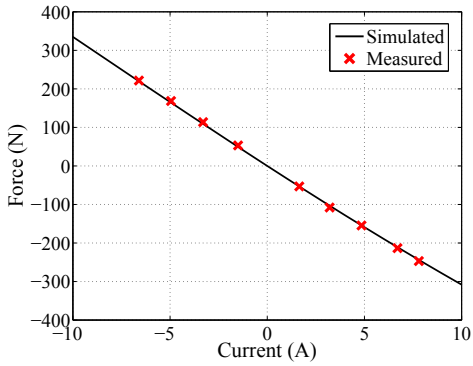

Figure 5.6: *Simulated and measured actuator force at different levels of steady coil current.*

In addition, the strengthening or weakening effect is time dependent, as magnetic diffusion must occur before the permanent magnet field is influenced, and the characteristic time for this effect is significantly larger than the 1 ms valve switch time, as previously discovered.

Transient actuator response comparison

The transient actuator response is examined both with voltage steps and current control sequences. The voltage steps are conducted by applying a fixed voltage level and letting the current rise to the corresponding steady value, while measuring the generated actuator force. A comparison between a positive and a negative voltage step, and the corresponding simulations is shown in figure 5.7.

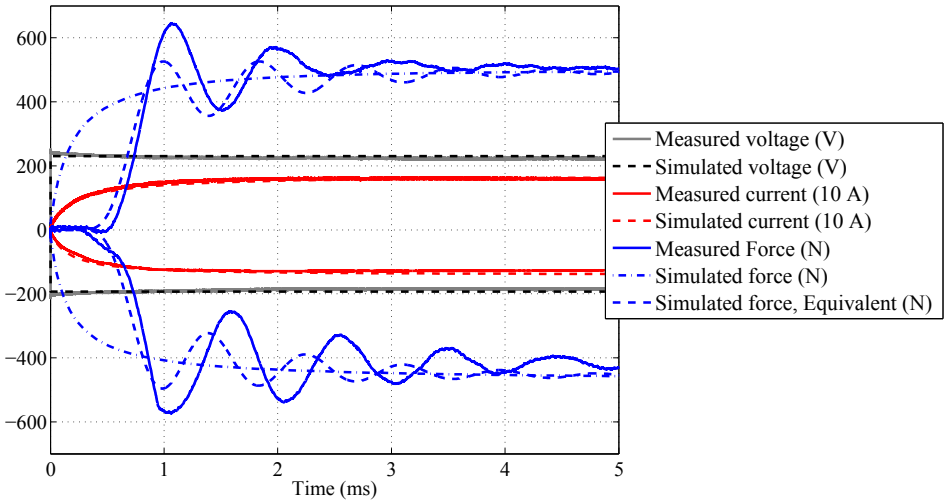

Figure 5.7: *Current and force responses for measured and simulated positive and negative voltage steps. The measured force is filtered through a signal amplifier and affected by oscillations in the mechanical structure.*

The measured current responses in figure 5.7 are seen to exhibit similar characteristics as the simulations. Each current build-up leads to a force build-up, which, according to the simulation and the Lorentz force law, results in a near proportional force rise. Due to signal filtering and mechanical oscillations, the measured forces significantly differs from the simulated actuator forces as seen in figure 5.7. Mimicking the effect of mechanical oscillation and signal filtering in the simulation leads to the equivalent simulated force response shown in figure 5.7, where reasonable correspondence is seen when compared to the measured response. The transfer function of the mechanical structure is approximated on basis of 3D finite element modal analysis, where the dominating frequencies are taken into account. In total, the simulations are seen to yield good correspondence with the experimental measurements shown in figure 5.7.

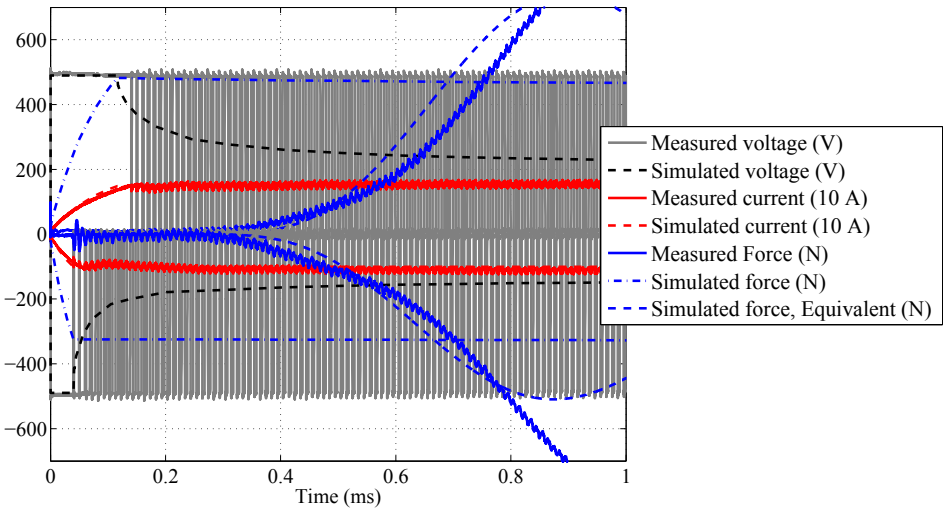

Figure 5.8: *Simulated and measured current response to a current control sequence. A relatively large voltage is applied until a constant current reference is reached. The simulation does not utilize PWM voltage.*

Figure 5.8 show the simulated and measured response to a current control sequence, where maximum voltage is initially applied when the current error is large, followed by a constant current reference control. The simulated and measured current responses are seen to have similar characteristics, albeit the simulated current tends to rise slightly faster than the corresponding measurements. Again, similar to the response in figure 5.7, the measured force is significantly delayed, but as indicated by the equivalent simulated force, the actuator force is expected to be present following the current rise.

The current rise time differs depending on the current direction, with lowest current rise time being present when the coil generated field acts in the positive direction of the permanent magnet field. Here the coil field act to further saturate the steel material, leading to a lower apparent self-inductance compared to the opposite current direction. The moving coil circuit should therefore be designed such that valve closing force is obtained when generating a magnetic field in the same direction as the permanent magnet, in order to obtain the lowest force build-up time for a given actuator circuit.

5.2 Manufacturing experience with reinforced PEEK

The ring part of the plunger has been made using carbon fiber reinforced PEEK, cf. figure 5.2. A pre-made solid plate of reinforced PEEK has been used as basis for the machining. According to the supplier, the plate should be homogenous and it should be possible to manufacture the part within tolerances.

However, residual material stresses were found to make manufacturing of the annular part a challenge. A challenge which has not yet been resolved. When performing the rough-machining of the part the material curves significantly due to residual stresses, as illustrated in figure 5.9. These residual stresses dominate despite having performed a pre, in between and post heat treatment of the material.

Figure 5.9: *Rough-machined plunger part in reinforced PEEK. Residual material stresses result in a significantly curved part.*

The main cause of this deformation is assumed to be the presence of a main fiber orientation crosswise of the annular part. This anisotropic property of the material may cause the ring shape to curve significantly. Improved machining methods or a main fiber orientation in the longitudinal direction may resolve this behavior, which is being attempted in order to achieve the desired plunger part with acceptable tolerances.

Chapter 6

Conclusions and Further Work

This thesis is concerned with the design and optimization of seat valves for digital hydraulic motors, where the application target is hydrostatic transmissions in large scale wind turbines. In such transmissions, a slow rotating hydraulic pump is directly driven by the turbine rotor, and pressurized oil is used to drive a variable displacement motor connected to a fast rotating generator. Variable displacement of the digital hydraulic motor is obtained by controlling a number of independent seat valves using relatively small linear electro-magnetic actuators.

Strict requirements are present for these valves in order to obtain efficient motor operation. The valves must be fast switching, exhibit very low pressure loss and endure billions of load cycles to compete with existing drive train solutions for wind turbines. Focus in this thesis have been on the machine efficiency in terms of minimizing the valve switching time and pressure losses, while the durability matter have been postponed for further research.

A suitable topology for such efficient valves has been selected, resulting in annular seat geometry and a moving coil linear electro-magnetic actuator. The annular geometry was chosen for its high area gradient and low moving mass, and the moving coil was chosen for its low force build-up time. This valve topology has been used as basis for a valve design optimization.

A valve design method have has developed and presented, taking into account the dominating aspects when designing seat valves for digital hydraulic machines. Within this method, a number of steps are used to optimize and evaluate the valve based on specifications of a target machine. The design method is computationally expensive as a whole, but may be performed for a given valve topology within a reasonable time frame of a month or two.

This design method has been shown applied to the chosen valve topology. The optimized valve has a simulated switching time of 1.0 ms and a pressure loss of 0.3/0.5 bar at 650 l/min for positive and negative flow direction respectively. Such valve performance results in very efficient motoring operation of approximately 99 % in a broad operation range, when considering only valve flow loss and actuator energy loss.

Encouraged by these promising simulation results, a prototype of this optimized valve has been manufactured. The transient force build-up of the valve actuator has been experimentally tested, and shown to agree well with the predicted performance. Challenges when manufacturing the valve plunger in the chosen composite material have been experienced, leading to unacceptable tolerances. This problem has yet to be resolved, in order to enable further testing of the valve prototype.

Further Work

Further work includes manufacturing of an acceptable valve plunger in reinforced PEEK, such that additional valve tests may be conducted. Improved machining processes may solve the tolerance problems; otherwise different basis materials with improved carbon fiber orientations may be needed. Assuming satisfactory tolerances of the valve plunger, the prototype tests include submerging in oil and pressurization in order to validate the simulated switching time and examine stiction/squeeze effects when operating the valve at higher pressures. In addition, valve leakage is a topic for investigation.

Next large study is on the durability of the valve, in particular wear and fatigue at the valve seat. An improved wire connection to the moving coil is needed, preferably using a braided wire solution to avoid fatigue failure at the coil connection.

Another interesting topic for further work is a study into the possibility of improving the transient performance of a variable reluctance linear actuator (solenoid). This actuator type has a durable moving steel member, which is intriguing for improved durability. Laminations may be included in such actuator design, leading to improvements in the force build-up performance compared to that found in the presented work.

Bibliography

[1] Enercon, "E-126 Wind turbine technical data," available online at www.enercon.de.

[2] E. Hau, *Wind Turbines - Fundamentals, Techonologies, Application, Economics*. Springer, 2013.

[3] Alstom, "Haliade® 150-6MW," brochure available from www.alstom.com.

[4] Wind Power Monthly, "Close up - Vestas V164-8.0 nacelle and hub," sep. 2013, Available online at www.windpowermonthly.com.

[5] M. Liserre, R. Cardenas, M. Molinas, and J. Rodriguez, "Overview of Multi-MW Wind Turbines and Wind Parks," *Industrial Electronics, IEEE Transactions on*, vol. 58, no. 4, pp. 1081–1095, April 2011.

[6] H. Polinder, J. Ferreira, B. Jensen, A. Abrahamsen, K. Atallah, and R. McMahon, "Trends in Wind Turbine Generator Systems," *IEEE Journal of Emerging and Selected Topics in Power Electronics*, vol. 1, no. 3, pp. 174–185, 2013.

[7] H. Li and Z. Chen, "Overview of different wind generator systems and their comparisons," *Renewable Power Generation, IET*, vol. 2, no. 2, pp. 123–138, June 2008.

[8] S. M. Muyeen, *Wind Energy Conversion Systems - Technology and trends*. Springer, 2012.

[9] J. B. Gayo, *Final Publishable Summary of Results of Project ReliaWind*. ReliaWind, 2011.

[10] R. H. Hansen, "Design and Control of the Power Take-Off System for a Wave Energy Converter with Multiple Absorbers," Ph.D. dissertation, Engineering and Science at Aalborg University, 2013.

[11] S. C. Rybak, "Description of the 3 MW SWT-3 wind turbine at San Gorgonio Pass, California," *NASA. Lewis Research Center Large Horizontal-Axis Wind Turbines*, pp. 575–588, 1981.

[12] J. Schmitz, N. Vatheuer, and H. Murrenhoff, "Hydrostatic Transmissions: A Power Play in Wind Turbine Design," *Hydraulics & Pneumatics*, vol. RWTH Aachen University, IFAS, 2013.

[13] P. Chapple, M. Niss, and K. E. Thomsen, "Wind turbines with variable hydraulic transmissions and electrically excited synchronous generators directly connected to the grid," in *Proceedings of the ASME Symposium on Fluid Power and Motion Control, FPMC*, 2012.

[14] Rexroth Bosch Group, "Radial piston hydraulic motor - Type Hägglunds CBM," datasheet available from www.boschrexroth.com.

[15] Danfoss, "Technical Information - Bent Axis Variable Displacement Motors - Series 51 and 51-1," datasheet available from www.powersolutions.danfoss.com.

[16] W. Rampen, *The Development of Digital Displacement Technology.* Fluid Power and Motion Control (FPMC), 2010, ch. Keynote address, pp. 12–17.

[17] M. Sasaki, A. Yuge, T. Hayashi, H. Nishino, M. Uchida, and T. Noguchi, "Large Capacity Hydrostatic Transmission with Variable Displacement," in *The 9th International Fluid Power Conference, 9. IFK*, 2014.

[18] Artemis Intelligent Power Ltd, "7 MW DD Transmission - Progress Report, November 2013," video available at www.artemisip.com/news-media/videos.

[19] T. Kazuhisa, M. Atsushi, S. Masayuki, S. Stephen, S. Uwe, R. William, F. Robert, and K. Hauke, "Wind turbine generator and tidal current generator," Chinese Patent CN102 959 238A, 2010.

[20] T. Kameda, M. Uchida, O. Uehara, and H. Dodson, "Hydraulic pump, method for maintaining same, and wind power generation device," Patent WO2 014 002 522A1, 2012.

[21] K. Takuro, D. Henry, R. Alasdair, and R. William, "Method and apparatus for performing maintenance on hydraulic pump, and power generating apparatus of renewable energy type," International Patent WO2 013 031 072A1, 2011.

[22] E. de Vries, "Mitsubishi launches 7MW turbine," wind Power Monthly, January 1th 2011.

[23] T. Kazuhisa, M. Atsushi, S. Masayuki, S. Stephen, S. Uwe, R. William, F. Robert, and K. Hauke, "Wind turbine generator and tidal current generator," Patent CN102 959 238A, 2010.

[24] W. Rampen, J. Almond, and S. Salter, "The Digital Displacement Pump/Motor Operating Cycle: Experimental Results Demonstrating the Fundamental Characteristics," in *International Fluid Power Workshop, Bath*, 1994.

[25] D. B. Roemer and P. Johansen, "Design of a High Efficiency Valve for use in a Digital Displacement Hydraulic Pump," Master's thesis, AAU, 2011.

[26] M. Ehsan, W. Rampen, and S. H. Salter, "Modeling of Digital-Displacement Pump/Motors and Their Application as Hydraulic Drives for Nonuniform Loads," *Project B3 - Power Take-off Systems*, vol. 122, no. 1, pp. 210–215, 2000.

[27] S. H. Salter, J. Taylor, and N. Caldwell, "Power Conversion Mechanisms for Wave Energy," in *Proceedings of the Institution of Mechanical Engineers, Part M: Journal of Engineering for the Maritime Environment*, 2002.

[28] J. Taylor, W. Rampen, A. Robertson, and N. Caldwell, "Digital Displacement Hydraulic Hybrids," in *Proceedings of JSAE Annual Congress*, 2011.

[29] J. Ivantysyn and M. Ivantysynova, *Hydrostatic Pumps and Motors*, J. Sakethataraman, Ed. abi, 2001.

[30] M. Linjama, "Digital Fluid Power - State of the Art," in *Proc. of the Twelfth Scandinavian International Conference on Fluid Power*, 2011.

[31] M. Linjama. and K. Huhtala, "Digital pump-motor with independent outlets," in *The 11th Scandinavian International Conference on Fluid Power, SICFP'09*, 2009.

[32] M. Heikkilä, J. Tammisto, M. Huova, K. Huhtala, and M. Linjama, "Experimental Evaluation of a Piston-Type Digital Pump-Motor-Transformer with Two Independent Outlets," in *Proceedings of Fluid Power and Motion Control conference, FPMC*, 2010.

[33] J. Tammisto, M. Huova, M. Heikkilä, M. Linjama, and K. Huhtala, " Characteristics of an In-line Pump with Independently Controlled Pistons," in *7th International Fluid Power Conference*, 2010.

[34] M. Karvonen, M. Linjama, M. Heikkilä, and K. Huhtala, "Analysis of signals and power flow in a digital hydraulic multi actuator application," in *Proceedings of the 8th FPNI Ph.D Symposium on Fluid Power, FPNI2014*, 2014.

[35] M. A. Holland, G. J. Wilfong, K. J. Merrill, and J. H. Lumkes, "Experimental Evaluation of Digital Pump/Motor Operating Strategies with a Single-Piston Pump/Motor," in *Proceedings of the 52nd National Conference on Fluid Power, Las Vegas*, 2011.

[36] K. J. Merrill, M. A. Holland, and J. H. Lumkes, "Efficiency Analysis of a Digital Pump/Motor as Compared to a Valve Plate Design," in *7th International Fluid Power Conference*, 2010.

[37] K. Merrill, M. Holland, and J. Lumkes, "Analysis of Digital Pump/Motor Operating Strategies," in *Proceedings of the 52nd National Conference on Fluid Power, Las Vegas*, 2011.

[38] Artemis Intelligent Power Ltd, "Digital Displacement® technology," brochure available from www.artemisip.com.

[39] Artemis Intelligent Power Ltd., Webpage information, Available at www.artemisip.com.

[40] J.-P. Uusitalo, T. Lauttamus, M. Linjama, L. Söderlund, M. Vilenius, and L. Kettunen, "Miniaturized bistable seat valve," *The Tenth Scandinavian International Conference on Fluid Power, SICFP*, vol. 10, no. 3, pp. 379–391, 2007.

[41] J.-P. Uusitalo, L. Soederlund, M. Junola, L. Kettunen, V. Ahola, and M. Linjama, "Novel bistable hammer valve for digital hydraulics," *International Journal of Fluid Power*, vol. 11, pp. 35–44, 2010.

[42] A. Ploeckinger, B. Winkler, and R. Scheidl, "Development and Prototyping of a Compact, Fast 3/2 Way Switching Valve with Integrated Onboard Electronics," in *Proceedings of the 11th Scandinavian International Conference on Fluid Power*, 2009, iSBN 978-91-02-7393-588-3.

[43] R. Scheidl and B. Winkler, "Optimization of a Fast Switching Valve for Big Flow Rates," in *Power Transmission and Motion Control - PTMC*, 2006.

[44] B. Winkler and R. Scheidl, "Development of a Fast Seat Type Switching Valve for Big Flow Rates," in *The Tenth Scandinavian International Conference on Fluid Power*, vol. 10, 2007, pp. 137–146.

[45] B. Winkler, A. Ploeckinger, and R. Scheidl, "A novel piloted fast switching multi poppet valve," *International Journal of Fluid Power*, vol. 11, pp. 7–14, 2010.

[46] M. Linjama and M. Vilenius, "Digital Hydraulics - Towards perfect valve technology," in *The Tenth Scandinavian International Conference On Fluid Power, SICFP*, 2007.

[47] S. Salter and W. Rampen, "Improved fluid-working machine," Patent EP 0 494 236 B1, 12 13, 1990, patent No. EP 0494236 B1.

[48] S. H. Salter and W. H. S. Rampen, "Pump control method and poppet valve therefor," Patent EP 0 361 927 B1, 07 27, 1989, patent No. EP 0361927 B1.

[49] W. Rampen, N. Caldwell, and U. Stein, "Annular valve," Patent US 7 077 378, 07 18, 2002, patent No. US 7077378.

[50] J. Taylor, Online video, "Power for Change - Intelligent Power - the development of digital hydraulics", 2009, available at www.youtube.com.

[51] W. Rampen, U. Stein, P. Bernhard, F. R. Mcintyre, G. P. Voller, and C. F. Souza, "Electronically controlled valves," Patent Application WO 2010/106 361 A1, 09 23, 2010, patent No. WO 2010/106361 A1.

[52] Artemis Intelligent Power Ltd., "Fluid distribution valve," European Patent, 2008, patent EP2187104A1.

[53] U. Stein, "Valve for a fluid-working machine," Patent GB 2 430 246 B, 03 1, 2005, patent No. GB 2430246 B.

[54] B. Lequesne, "Finite-element analysis of a constant-force solenoid for fluid flow control," *IEEE Transactions on Industry Applications*, vol. 24, pp. 574–581, 1988.

[55] H. E. Merritt, *Hydraulic Control Systems.* John Wiley & Sons, Ltd., 1967.

[56] S. Cetinkunt, *Mechatronics.* John Wiley and Sons, Inc., 2006.

[57] H. H. Woodson and J. R. Melcher, *Electromechanical Dynamics.* John Wiley & Sons, Inc., 1968.

[58] M. Resch and R. Scheidl, "A model for fluid stiction of quick separating circular plates," *Mechanical engineering science*, p. Online before print, 2013.

[59] R. Scheidl and C. Gradl, "An oil stiction model for flat armature solenoid switching valves," in *Proc. ASME/BATH 2013 Symposium on Fluid Power & Motion Control*, Sarasota, Florida, USA, October 2013.

[60] M. F. Ashby, *Materials Selection in Mechanical Design.* Elsevier, 2005.

[61] S. H. Salter, "Digital Hydraulics for Renewable Energy," in *World Renewable Energy Conference Aberdeen*, 2005, wE3.4.

[62] Victrex, "Material Properties Guide," available online at: www.victrex.com.

[63] B. Lequesne, "Fast-acting Long-stroke Bistable Solenoids With Moving Permanent-magnets," *IEEE Transactions On Industry Applications*, vol. 26, pp. 401–407, 1988.

[64] J.-P. Uusitalo, "A novel digital hydraulic valve package: A fast and small multi-physics design," Ph.D. dissertation, Tampere University of Technology, Tampere, Finland, 2010.

[65] J. Kim and J. Chang, "A New Electromagnetic Linear Actuator for Quick Latching," *IEEE Transactions on Magnetics*, vol. 43, pp. 1849–1852, 2007.

[66] L. Nascutiu, "Voice coil actuator for hydraulic servo valves with high transient performances," in *IEEE International Conference on Automation Quality and Testing, Robotics*, 2006.

[67] L. Liu and S. Chang, "A moving coil electromagnetic valve actuator for camless engines," *IEEE International Conference on Mechatronics and Automation*, vol. 1, pp. 176–180, 2009.

[68] B. Lequesne, "Permanent magnet linear motors for short strokes," *IEEE Transactions On Industry Applications*, vol. 32, pp. 161–168, 1996.

[69] J. A. Wagner, "The actuator in high performance disk drives: Design rules for minimum access time," *IEEE Transactions On Magnetics*, vol. Mag-19, no. 5, pp. 1686–1688, September 1983.

[70] Y. Liu, M. Zhang, Y. Zhu, J. Yang, and B. Chen, "Optimization of Voice Coil Motor to Enhance Dynamic Response Based on an Improved Magnetic Equivalent Circuit Model," *IEEE Transactions on Magnetics*, vol. 47, no. 9, pp. 2247–2251, 2011.

[71] S. Kim and H. Murrenhoff, "Measurement of effective bulk modulus for hydraulic oil at low pressure," *Journal of Fluids Engineering, Transactions of the ASME*, vol. 134, no. 2, 2012.

[72] R. Castilla, P. Gamez-Montero, N. Ertürk, A. Vernet, M. Coussirat, and E. Codina, "Numerical simulation of turbulent flow in the suction chamber of a gearpump using deforming mesh and mesh replacement ," *International Journal of Mechanical Sciences*, vol. 52, no. 10, pp. 1334 – 1342, 2010.

[73] Ansys, *User's Guide*. Ansys Inc., 2011, Available online.

[74] ——, *Meshing Users Guide*. Ansys Inc., 2011, Available online.

[75] W. Borutzky, B. Barnard, and J. Thoma, "An orifice flow model for laminar and turbulent conditions," *Simulation Modelling Practice and Theory*, vol. 10, no. 3-4, pp. 141 – 152, 2002.

[76] B. R. Munson, D. F. Young, T. H. Okiishi, and W. W. Huebsch, *Fundamentals of Fluid Mechanics*. John Wiley and Sons, 2010.

[77] G. S. Payne, A. Kiprakis, M. Ehsan, W. H. S. Rampen, J. P. Chick, and R. Wallace, "Efficiency and Dynamic Performance of Digital DisplacementTM Hydraulic Transmission in Tidal Current Energy Converters," in *Journal of Power and Energy*, vol. 221, May 2007, pp. 207–217.

[78] R. L. Norton, *Machine Design - An Integrated Approach*. Pearson, 2006.

[79] Ansys, "Mechanical APDL Material Reference," 2012, Unpublished, available online.

[80] S.-Y. Fu, B. Lauke, and Y.-W. Mai, *Science and engineering of short fibre reinforced polymer composites*. Woodhead Publishing in Materials, 2009.

[81] D. H. Johnson, "Principles of Simulating Contact Between Parts using ANSYS," Unpublished, available online.

[82] R. Cook, D. Malkus, M. Plesha, and R. Witt, *Concepts and Application of Finite Element Analysis*, W. Anderson, Ed. Wiley, 2002.

[83] W. Rampen and S. Salter, "Annular valve," Patent US2 013 205 986A1, 2013.

[84] F. Bauer, "The influence of liquids on compressor valves," in *Proc. of the international compressor conference*, Purdue, USA, July 1990, pp. 647–653.

[85] R. A. Pizarro-Recabarren, J. Barbosa, and C. J. Deschamps, "Modeling the Stiction Effect in Automatic Compressor Valves," in *Proc. international compressor engineering conference at Purdue*, West Lafayette, USA, July 2012.

[86] E. Giacomelli and M. Giorgetti, "Evaluation of Oil Stiction in Ring Valves," in *International Compressor Engineering Conference*, West Lafayette, USA, 1974, pp. 167–170.

[87] A. Z. Szeri, *Fluid Film Lubrication*. Cambridge University Press, 2011.

[88] C. E. Brennen, *Cavitation and Bubble Dynamics.* Oxford University Press, 1995.

[89] Y. Hori, *Hydrodynamic lubrication.* Springer-Verlag Tokyo, 2006.

[90] S. A. Sedgewick and D. H. Trevena, "Limiting negative pressure of water under Dynamic stressing," *Journal of Physics D: Applied Physics*, vol. 9, pp. 1983–1990, 1976.